

Dual Optical Comb LWIR Source and Sensor

Final Report

Reporting Period: 28 September 2015 – 28 September 2017

Joel M. Hensley, Justin M. Brown, Mark G. Allen
Physical Sciences Inc. (PSI)

Pierre Jouy, Jérôme Faist
Swiss Federal Institute of Technology (ETH)

Markus Geiser, Pitt Allmendinger, Markus Mangold, Andreas Hugi
IRsweep Inc.

Sponsored by
Defense Advanced Research Projects Agency (DOD)
DSO
ARPA Order No. HR0011515436

Issued by
U.S. Army Contracting Command – Redstone
Contract No. W31P4Q-15-C-0083

Agent
U.S. Army RDECOM, Aviation & Missile Research, Development & Engineering Center

Name of Contractor: Physical Sciences Inc.
Principal Investigator: Dr. Joel M. Hensley
Business Address: 20 New England Business Center, Andover, MA 01810-1077
Phone Number: (978) 689-0003
Effective Date of Contract: 28 September 2015
Contract Expiration Date: 28 September 2017

Approved for public release; distribution unlimited.

DISCLAIMER

This material is based upon work supported by the Defense Advanced research Projects Agency (DARPA) under Contract Number W31P4Q-15-C-0083. Any opinions, findings and conclusions or recommendations expressed in this material are those of the author(s) and do not necessarily reflect the views of DARPA Program Office.

REPORT DOCUMENTATION PAGE				Form Approved OMB No. 0704-0188	
Public reporting burden for this collection of information is estimated to average 1 hour per response, including the time for reviewing instructions, searching existing data sources, gathering and maintaining the data needed, and completing and reviewing this collection of information. Send comments regarding this burden estimate or any other aspect of this collection of information, including suggestions for reducing this burden to Department of Defense, Washington Headquarters Services, Directorate for Information Operations and Reports (0704-0188), 1215 Jefferson Davis Highway, Suite 1204, Arlington, VA 22202-4302. Respondents should be aware that notwithstanding any other provision of law, no person shall be subject to any penalty for failing to comply with a collection of information if it does not display a currently valid OMB control number. PLEASE DO NOT RETURN YOUR FORM TO THE ABOVE ADDRESS.					
1. REPORT DATE (DD-MM-YYYY) 12-10-2017		2. REPORT TYPE Final Technical Report		3. DATES COVERED (From - To) 28 Sep 2015 - 28 Sep 2017	
4. TITLE AND SUBTITLE Dual Optical Comb LWIR Source and Sensor				5a. CONTRACT NUMBER W31P4Q-15-C-0083	
				5b. GRANT NUMBER	
				5c. PROGRAM ELEMENT NUMBER	
6. AUTHOR(S) Joel M. Hensley ¹ , Justin M. Brown ¹ , Mark G. Allen ¹ , Pierre Jouy ² , Jérôme Faist ² , Markus Geiser ² , Pitt Allmendinger ² , Markus Mangold ² , Andreas Hugi ² Swiss Federal Institute of Technology (ETH) ² IRsweep Inc. ³				5d. PROJECT NUMBER	
				5e. TASK NUMBER	
				5f. WORK UNIT NUMBER	
7. PERFORMING ORGANIZATION NAME(S) AND ADDRESS(ES) Physical Sciences Inc. ¹ 20 New England Business Center Andover, MA 01810-1077				8. PERFORMING ORGANIZATION REPORT NUMBER PSI-1899/FinalReport	
9. SPONSORING / MONITORING AGENCY NAME(S) AND ADDRESS(ES) U.S. Army Aviation & Missile Research Development and Engineering Center ATTN: RDMR-WSD Redstone Arsenal, AL 35898				10. SPONSOR/MONITOR'S ACRONYM(S)	
				11. SPONSOR/MONITOR'S REPORT NUMBER(S)	
12. DISTRIBUTION / AVAILABILITY STATEMENT Approved for public release; distribution unlimited.					
13. SUPPLEMENTARY NOTES					
14. ABSTRACT In this program we developed a compact dual-optical frequency comb (OFC) sensor for standoff detection of national security relevant compounds. These compounds are primarily solids at room temperature and consequently have low vapor pressure. In realistic application scenarios these materials are found on common diffusely reflective. Because the target materials have their strongest spectral signatures in the longwave infrared (LWIR) regime, our OFC sources are based on dispersion compensated quantum cascade lasers (QCLs) in the 8 to 12 micron regime. The lasers emit about 1W of optical power under cw operation near room temperature and produce combs with optical bandwidths exceeding 100 wavenumbers. We developed processing algorithms for reducing the high bandwidth multi-heterodyne data stream into the desired spectral information with up to 0.3 cm ⁻¹ resolution and optimizing the signal to noise ratio. Finally, we tested a prototype dual-comb system against diffusely scattering surfaces at standoff distances up to 1 meter and demonstrated spectral discrimination at the few microgram mass loading level, a relevant metric for national security needs.					
15. SUBJECT TERMS Standoff Detection, Quantum Cascade Laser, Dual Comb Spectroscopy, Longwave Infra-red, Diffusely Scattering Surfaces					
16. SECURITY CLASSIFICATION OF:			17. LIMITATION OF ABSTRACT UU	18. NUMBER OF PAGES 92	19a. NAME OF RESPONSIBLE PERSON Joel M. Hensley
a. REPORT Unclassified	b. ABSTRACT Unclassified	c. THIS PAGE Unclassified			19b. TELEPHONE NUMBER (include area code) 978-689-0003

CONTENTS

1.0	SUMMARY	1
2.0	INTRODUCTION	2
3.0	METHODS, ASSUMPTIONS, AND PROCEDURES.....	4
3.1	Quantum Cascade Laser Optical Frequency Combs	4
3.1.1	QCL combs characterization.....	6
3.1.2	Dispersion compensation	7
3.1.3	Active region design and growth	13
3.1.4	Dual comb on a chip	20
3.2	Multi-heterodyne Signal Processing	25
3.2.1	F_{rep} tracking.....	25
3.2.2	Coherent averaging	31
3.2.3	Multi-heterodyne processing algorithm summary	36
3.3	Sensor Design	42
3.3.1	System model.....	42
3.3.2	Speckle.....	44
3.3.3	Detectors	45
3.3.4	Optical isolation	46
4.0	RESULTS AND DISCUSSION	48
5.0	CONCLUSIONS.....	79
6.0	RECOMMENDATIONS	80
7.0	REFERENCES	81
	LIST(S) OF SYMBOLS, ABBREVIATIONS, AND ACRONYMS.....	82

LIST OF FIGURES

Figure 1.	Schematic of single-chip dual optical comb source in HHL package (left) and implementation in a stand-off sensor geometry (right).....	2
Figure 2.	Schematic of comb formation in QCL by four wave mixing (FWM).	5
Figure 3.	Dual comb spectroscopy principle (top) with addition of an absorbing molecule (bottom).....	5
Figure 4.	Schematic of the setup used for QCL comb characterization (top). Optical spectra (bottom) obtained under the same driving conditions without (red curve) and with (blue curve) optical feedback.....	6
Figure 5.	Subthreshold interferogram (left) and zoom on the first satellite (right).....	7
Figure 6.	Schematic of a Gires-Tournois (GTI) coating principle	8
Figure 7.	Group delay dispersion (GDD) induced by a GTI coating.	8
Figure 8.	Measured LIV characteristics of a HR coated laser at different temperatures.	9
Figure 9.	Measured LIV characteristics of a GTI coated laser at different temperatures.	9
Figure 10.	Measured RF beatnotes at -10C for different currents.....	10
Figure 11.	Measured GDD induced by an HR coating and a GTI coating together with the simulated GDD induced by the GTI coating.	10
Figure 12.	Simulated and measured GDD induced by a GTI coating made of Al_2O_3 , YF_3 , Ge and Au.	11
Figure 13.	Optical microscope image of the back facet of a laser after explosion of the GTI coating.	11
Figure 14.	Simulated group velocity dispersion (GVD) as a function of the wavelength for two different laser ridge width. Inset: optical mode profile simulation with COMSOL.....	12
Figure 15.	Simulated cross section of the plasmonic (red curve) and ridge optical (blue curve) mode as a function of the vertical position (top). Dispersion of the refractive index for the plasmonic (red curve) and ridge optical (blue curve) mode for different cladding thicknesses (middle) with inset showing mode profile simulations for the plasmonic (left) and ridge optical (right) mode. Simulated GVD of the ridge optical mode for different top cladding thicknesses (bottom).	13
Figure 16.	Simulated wavefunctions distribution (left) and LIV (right) for the structure of each stack.	14
Figure 17.	Simulation of the gain for each stack and total gain.	15
Figure 18.	LIV characteristics (a) and wall plug efficiency of the laser at -15°C (full line) and 20°C (dashed lines).	15

LIST OF FIGURES (Continued)

Figure 19. rf beatnote (a) and corresponding optical spectra (b) for different currents at -15°C. (c) Summarizes the beatnote frequency and width at -20 dB.....	16
Figure 20. a) rf beatnote at -15°C and 1375 mA. b): mode spacing and power per mode at 1375 mA for temperatures of -15°C (blue) and 20°C (red). c) rf beatnote for different currents at 20°C.....	17
Figure 21. Log scale spectra (left) and corresponding beatnote (right) for a temperature of 0°C and a current of 1000 mA.	17
Figure 22. Multi-heterodyne spectra with 20 ms integration time and zoom in (inset) between 230 and 250 MHz.	18
Figure 23. LIV characteristics of a 4.5 mm HR coated device at different temperatures.	19
Figure 24. Optical spectra at different currents for a temperature of -15°C (left) and corresponding RF beatnote (right).	19
Figure 25. SEM picture of a dual comb on a chip device from the first generation (top). Schematic of the heater principle for the first generation (bottom).	20
Figure 26. Schematic of the cross section of the second generation dual comb on a chip (top). SEM picture of the front facet of a sample from the second generation dual comb on a chip (bottom).	21
Figure 27. Spectra and zoom in of both lasers with (bottom) and without (top) current in the heater.	22
Figure 28. Beatnote of the two lasers on the dual comb on a chip device for different values of the current injected in one of the heaters.	23
Figure 29. Multi-heterodyne spectra obtain from a dual comb on a chip device.	24
Figure 30. Picture of the beam on a thermal paper when a single laser (left and right panel) and two lasers (middle panel) on the dual comb on a chip are driven.	24
Figure 31. Shift of the optical spectra for a constant current on the laser for different values of the current in the heater.	25
Figure 32. Uncorrected drift of the multi-heterodyne signal. The multi-heterodyne signal drifts due to noise in the laser over a number of subsequent multi-heterodyne acquisitions in the RF-frequency domain.	26
Figure 33. Multi-Heterodyne signal of a dual-comb QCL laser spectrometer.....	26
Figure 34. Multi-heterodyne signal before (left) and after (right) correction.	27
Figure 35. Aligned spectra at different point in the spectrum.	27
Figure 36. Master-slave setup to investigate the possibility to reduce the computational load on QCL processing.....	28
Figure 37. Master-slaving results of the dual-comb spectrometer.	29
Figure 38. Zoomed in result from the stabilized multi-heterodyne result.	30

LIST OF FIGURES (Continued)

Figure 39. Locking loop only controls one parameter, whereas there are two free-running parameters to control.....	31
Figure 40. (Left) Multi-heterodyne signal of the peak before digital time-domain correction (blue) and after digital time-domain correction (red). (Right) both signals after coherent averaging in the time-domain.	32
Figure 41. Full multi-heterodyne signal spectrum with coherent averaging after correcting the time-domain signal for both F_{rep} and F_{ceo} drifts.....	33
Figure 42. Allan deviation algorithm.	33
Figure 43. Allan deviation of coherently averaged signal.	34
Figure 44. Setup for evaluating laser SNR.	35
Figure 45. SNR plot.	36
Figure 46. The reference channel is used for identifying the comb tooth locations and drift.	37
Figure 47. Autocorrelation is used to quantify drift of peaks.	38
Figure 48. Output of grid finding algorithm reliably identifies peak locations.....	39
Figure 49. Amplitude threshold for peak processing.	39
Figure 50. Representation of the true amplitude (black arrow) we wish to determine and the actual measured amplitude (blue arrow) resulting after random noise (black circle) is added.	40
Figure 51. Representation of the true amplitude (black arrow) we wish to determine and the actual measured amplitude (blue arrow) resulting after random noise (black circle) is added for a small signal relative to noise amplitude.....	40
Figure 52. Processor design.....	42
Figure 53. (blue) and reflective (red) pathways that provide the total radiance at the detector.....	43
Figure 54. Signal to noise ratio (SNR) as a function of standoff distance to the target.	44
Figure 55. Key aspects of speckle.....	45
Figure 56. Vigo MCT detector.	46
Figure 57. Dispersion of cadmium thiogallate $\lambda/4$ waveplate designed for $\lambda = 7.5 \mu\text{m}$ with arrows marking commercially available wavelengths.....	47
Figure 58. Electronic switching between two test coupons, one with target compound applied and one blank.	49
Figure 59. Sample mounted on chopper wheel motor for measurements with continuously moving sample.	49
Figure 60. Optical layout for standoff measurements off of a diffusely scattering sample. This example shows a 0.3m standoff case.	50

LIST OF FIGURES (Continued)

Figure 61. Segment of raw time domain comb data from the reference detector (top) and signal detector (bottom).....	51
Figure 62. Raw frequency domain comb data from the reference detector (top) and signal detector (bottom) after bin averaging every 1024 points. Inset plot shows small region of frequency domain before bin averaging (gray).	51
Figure 63. Segment of frequency domain comb data from the reference detector (blue) and signal detector (green) along with processed results (bold) determining amplitude for each comb tooth.	52
Figure 64. Ratio of signal to reference comb envelope from previous figure (brown) shown for the full spectrum converted to optical frequency, along with a 12 point running average (black) equivalent to a 4 cm^{-1} resolution.	52
Figure 65. Optical Spectra from Laser 26HM.....	53
Figure 66. Optical Spectra from Laser 26BG.....	54
Figure 67. Envelope of optical spectra from laser 26HM (blue) and laser 26BG (red) along with their geometric mean (black).	55
Figure 68. Logarithmic scale plot of combined (geometric mean) laser spectra.	55
Figure 69. Previously measured LWIR absorption spectra for 4 representative simulants: fluorinated silicone oil (FSO), Krytox TM vacuum oil, Dimethicone (SF-96), UCON OSP-150 lubricant.	56
Figure 70. LWIR absorption spectra for 4 representative simulants in the region of the QCL comb emission.	57
Figure 71. Liquid spectrophotometer cell.	57
Figure 72. Fractional transmission from FTIR transmission spectra of FSO samples in Table 2 at a resolution of 4 cm^{-1}	58
Figure 73. FSO Transmission as function of mass loading to determine absorption cross section.	59
Figure 74. IR transmission spectra for hexafluorobenzene from SDBS database.	60
Figure 75. A) Fractional transmission of Krytox TM in hexafluorobenzene at various concentrations. B) Peak absorbance at 1250 cm^{-1} verses mass loading.	61
Figure 76. FTIR reflection signal from a Blank sample (black), an FSO sample (blue), and no sample (red).....	62
Figure 77. FTIR measured reflectance from all FSO samples and one blank (red).....	62
Figure 78. FTIR measured reflectance from all Krytox TM samples and one blank (red).....	63
Figure 79. Raw comb envelope from blank samples.	64
Figure 80. Comb envelope of blank samples normalized by mean of all F series blanks.	65

LIST OF FIGURES (Continued)

Figure 81. Raw comb envelope of FSO samples.	65
Figure 82. Comb envelope from FSO samples normalized by mean of all F series blanks.....	66
Figure 83. Comb envelope from FSO samples normalized by mean of all F series blanks and 3 rd order polynomial baseline removed.....	66
Figure 84. Raw comb envelope of Krytox™ samples.	67
Figure 85. Comb envelope of Krytox™ samples normalized by mean of all F series blanks.	67
Figure 86. Comb envelope of Krytox™ samples normalized by mean of all F series blanks and 3 rd order polynomial baseline removed.	68
Figure 87. Series of raw comb envelope measurements from FSO applied in place sample.	69
Figure 88. Series of comb envelope measurements from FSO applied in place sample, normalized to first measurement (FSA23).....	69
Figure 89. Series of comb envelope measurements from FSO applied in place, normalized to first measurement (FSA23) and 3 rd order polynomial baseline removed.....	70
Figure 90. Series of raw comb envelope measurements from Krytox™ applied in place sample.	71
Figure 91. Series of comb envelope measurements from Krytox™ applied in place sample, normalized to first measurement (GSA24).....	71
Figure 92. Series of comb envelope measurements from Krytox™ applied in place sample, normalized to first measurement (GSA24) and linear baseline removed.....	72
Figure 93. Raw comb envelope of FSO samples at 0.98m standoff.	73
Figure 94. Comb envelope of FSO samples normalized by mean of measurements EB1,EB2,EB3,EB4 at 0.98m standoff.	73
Figure 95. Comb envelope of FSO samples normalized by mean of measurements EB1,EB2,EB3,EB4 and 3 rd order polynomial baseline removed at 0.98m standoff.	74
Figure 96. Raw comb envelope of Krytox™ samples at 0.98m standoff.	74
Figure 97. Comb envelope of Krytox™ samples normalized by mean of measurements EB1,EB2,EB3,EB4 at 0.98m standoff.	75
Figure 98. Comb envelope of Krytox™ samples normalized by mean of blank measurements EB1,EB2,EB3,EB4 and 3 rd order polynomial baseline removed at 0.98m standoff.	75

LIST OF FIGURES (Continued)

Figure 99. Series of raw comb envelope measurements from FSO applied in place sample at 0.98m standoff.....	76
Figure 100. Series of comb envelope measurements from FSO applied in place sample, normalized to first measurement (ESA22) at 0.98m standoff.....	77
Figure 101. Series of comb envelope measurements from FSO applied in place sample, normalized to first measurement (ESA22) and 3 rd order polynomial baseline removed at 0.98m standoff.....	77
Figure 102. Selected comb envelope measurements from FSO applied in place sample, normalized to first measurement (ESA22) and 3 rd order polynomial baseline removed at 0.98m standoff.....	78

LIST OF TABLES

Table 1.	Measurement Summary	48
Table 2.	FSO Samples.....	58
Table 3.	Linear Fit Coefficients from Previous Figure.....	59
Table 4.	Krytox TM Samples.....	60
Table 5.	Summary of Target Coupons and Their Mass Loading.....	63

1.0 SUMMARY

In this program we developed a compact dual-optical frequency comb (OFC) sensor for standoff detection of national security relevant compounds. These compounds are primarily solids at room temperature and consequently have low vapor pressure. In realistic application scenarios these materials are found on common surfaces that are not necessarily optically flat and highly reflective, so we emphasize diffusely reflective surfaces that are representative of the real-world surfaces. Because the target materials have their strongest spectral signatures in the longwave infrared (LWIR) regime, our OFC sources are based on dispersion compensated quantum cascade lasers (QCLs). Targeting two spectrally rich regions of the LWIR, we designed lasers at 8.3 μm (1180 to 1240 cm^{-1}) and 10.0 μm with a novel dispersion compensating approach in the laser processing. The 8 μm lasers emit ~ 1 W optical power under cw operation near room temperature and produce combs with optical bandwidths exceeding 100 cm^{-1} . We developed processing algorithms for reducing the high bandwidth multi-heterodyne data stream into the desired spectral information with up to 0.3 cm^{-1} resolution and optimizing the signal to noise ratio. Finally, we tested a prototype dual-comb system against diffusely scattering surfaces at standoff distances up to 1 meter and demonstrated spectral discrimination at the few $\mu\text{g}/\text{cm}^2$ mass loading level, a relevant metric for national security needs.

2.0 INTRODUCTION

Physical Sciences Inc. (PSI), together with the research group of Prof. Jérôme Faist at ETH Zürich and IRsweep, developed a chip-scale dual Optical Frequency Comb (OFC) source in the LWIR targeting the detection of multiple chemical agent simulant films at or below the $\mu\text{g}/\text{cm}^2$ areal density in the presence of typical background clutter at proximal stand-off distances up to 5m. The OFC's are generated by two Quantum Cascade Lasers (QCL's) optimized for up to 150 cm^{-1} of comb bandwidth and 1W output power. A schematic of the source and its overall stand-off sensor implementation is shown in Figure 1. The dual OFC will be grown and processed on a single epitaxial substrate. Each OFC will be electrically driven and free-running (requiring no optical locking mechanisms). This QCL-based comb source is a unique, cw-comb source, where the QCL cavity is the micro-resonator with giant 3rd-order non-linearity for comb generation that requires no external pump laser.

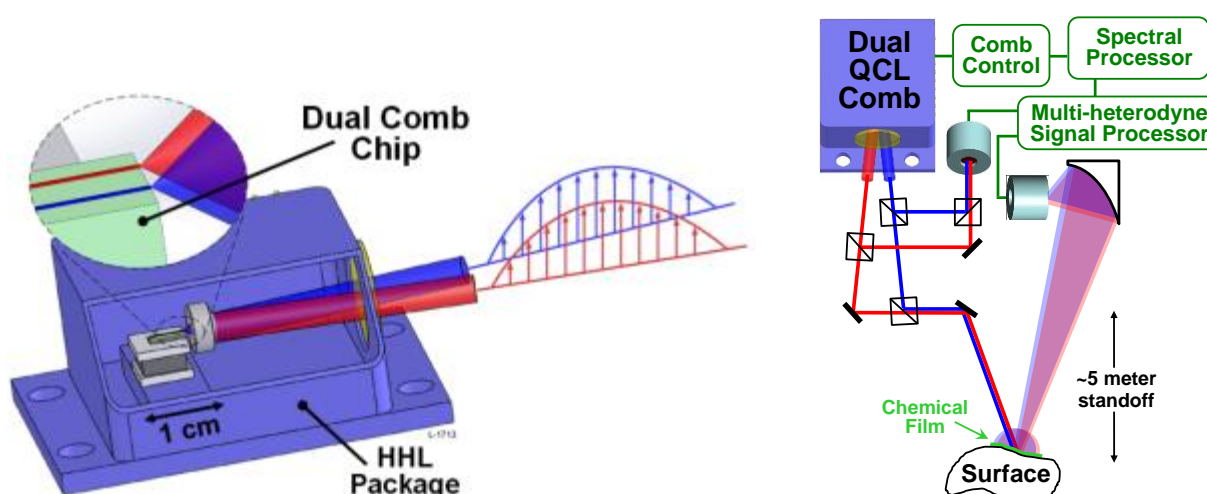


Figure 1. Schematic of single-chip dual optical comb source in HHL package (left) and implementation in a stand-off sensor geometry (right).

The key performance parameters for the OFC, as well as all other sub-systems, are derived from the sensor chemical detection requirements. The existing state of the art in stand-off LWIR laser-based sensing of trace chemical films requires bulky and expensive external-cavity QCL sources. This program addresses the cost and the size of these sources and it also provides over one order of magnitude increase in spectral density for the target 1 Hz detection rate, providing improved detection and speciation capability while reducing sensitivity to clutter noise. Compared to the previous state of the art in QCL-based OFC's, this program increased the average power and spectral bandwidth by an order of magnitude.

The proposed sensing scenario is a DoD mission objective for post-event reconnaissance of surface contaminants following the release of chemical agents. Surfaces of interest include local topology, equipment (painted metal surfaces, structures), and typical construction material (cloth, plastics, etc.). Typical interfering materials/chemicals that might be present on these surfaces include dust, pollen, soil, vegetation, various petroleum products, soot, and other

industrial compounds. The system level requirements have been derived from the Joint Program Executive Office for Chemical and Biological Defense (JPEO-CBD) Next Generation Chemical Detector (NGCD) system. The sensor developed here is expected to significantly reduce the cost and SWaP of this system, while increasing performance.

This report summarizes our accomplishments from Phase 1 addressing the following key technical challenges:

- **Engineered Dispersion Control in High Power QCL Combs:** Achieving the required spectral bandwidth and average output power will require careful management of the QCL dispersion. Dispersion control in QCL devices will be achieved by waveguide, doping, and facet reflectance design and optimization to balance the various contributions so as to achieve a flat dispersion curve over the spectral bandwidth. At high operating powers, the dispersion due to the optical gain is an additional design parameter that is optimized to achieve the target power and comb bandwidths.
- **Optimized and efficient signal processing:** To acquire the entire optical spectrum of 150 cm^{-1} in the RF-bandwidth of 500 MHz on two detectors, data-rates of at least 4 GBytes/sec are generated, which need to be processed in real-time to generate the LWIR spectrum.
- **Standoff detection from diffusely scattering surfaces:** Speckle noise and background clutter can dominate noise sources in laser-based diffuse scattering/reflectance sensing. Speckle properties of comb sources are analyzed and mitigated using spatial diversity.

3.0 METHODS, ASSUMPTIONS, AND PROCEDURES

3.1 Quantum Cascade Laser Optical Frequency Combs

The Quantum Cascade Laser (QCL) was first experimentally in 1994 (Faist et al. 1994). It is constituted of two parts: the gain medium (as well named active region) and the cavity. The active region is a multilayer structure of at least two different semiconductor which present an offset in the conduction band. This allow to create so called quantum wells in which the electrons will have quantified energies; intersubband transitions allow the emission of photons. By engineering the width of each layer and applying a voltage on the structure, a cascading structure allows to reach population inversion and photon emission at the desired wavelength. Finally, the fabrication of a cavity allows for the lasing emission to occur; the spectrum of emission of the QCL corresponds to the convolution of the cavity modes with the gain spectra. for this project, the material used are InGaAs/AlInAs grown by MBE on InP substrate. The cavity is a ridge cavity with a width between 4 and 10 μm , a height around 3 μm and a length of typically 4.5 mm. such cavity gives rise to Fabry-Perot multi-mode emission with a mode separation of about 0.3 cm^{-1} .

Frequency combs are characterized by equally spaced mode and a constant phase relation between the modes. In QCLs, the natural dispersion of the materials gives dispersive Fabry-Perot modes. The frequency comb regime is reached thanks to the so called four wave mixing (FWM) schematized in Figure 2 which allows locking of all the modes. Each comb line can be characterized by the offset frequency f_{CEO} , the repetition frequency f_{rep} and the index N of the line.

For dual comb spectroscopy (Schiller 2004, Keilmann et al. 2004, Coddington et al. 2010, Villares et al. 2014), two QCL combs with slightly different f_{rep} are combined on a fast detector. Each pair of line will beat together and give rise to a line in the RF domain as shown in Figure 3. By placing an absorbing molecule on the path of one or both laser beam, the intensity of the lines in the optical domain will be affected and will be directly transferred in the RF multi-heterodyne signal. This technique has the advantage to not require moving parts as all wavelengths are analyzed in parallel. As well, using lasers as a source offers a very high brightness, necessary for standoff detection.

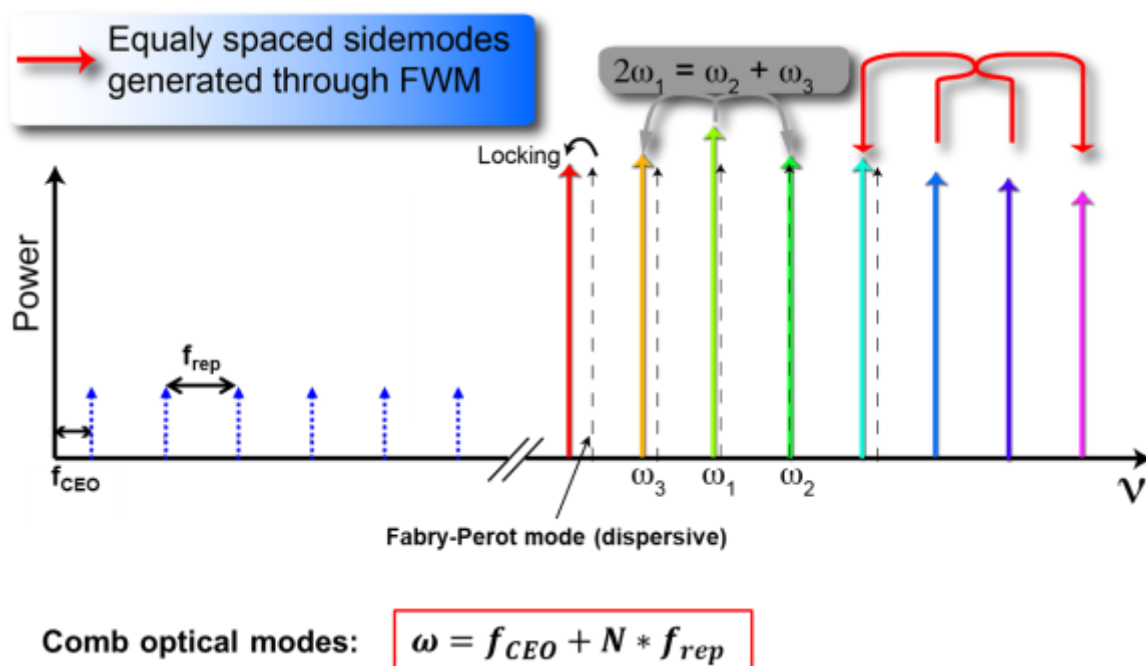


Figure 2. Schematic of comb formation in QCL by four wave mixing (FWM).

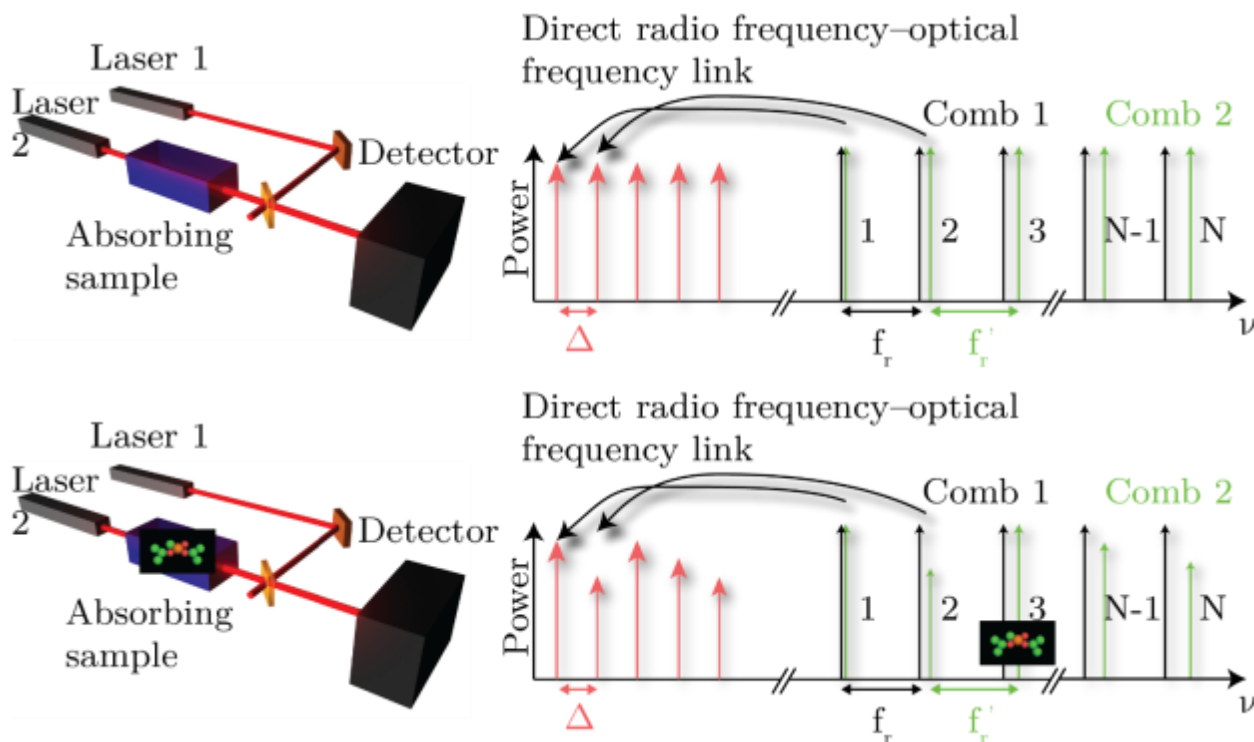


Figure 3. Dual comb spectroscopy principle (top) with addition of an absorbing molecule (bottom).

3.1.1 QCL combs characterization

The setup for QCL comb characterization is described in Jouy et al. [2017]: Even if QCL frequency combs are stable under operation, they are sensitive to small changes in optical feedback. It is therefore important to do all characterizations under the same optical conditions. To ensure consistent data characterization, we adopted the setup schematized in Figure 4 top. The laser is driven with a low noise driver and a bias-T sends the RF part of the current on a spectrum analyzer to characterize the frequency comb beatnote. The beam is collimated with a high numerical aperture lens of NA=0.85. In order to isolate the laser from back-reflections from the Fourier Transform Infrared Spectrometer (FTIR), a tilted neutral density filter (NDF) with 1% transmission is placed after the lens. A beam splitter can be used to monitor the evolution of the optical power after the NDF. Finally, the spectra are measured with a FTIR and the optical power is measured by placing a thermopile sensor directly after the lens. In this configuration, we verified that no element placed after the NDF will disturb the beatnote measured on the spectrum analyzer. Figure 4 bottom shows two spectra obtained under the same driving conditions but once with a narrow beatnote and once with a broad beatnote. The broad beatnote was obtained by placing the NDF perpendicular to the beam to increase the optical feedback in the laser and destabilize the frequency comb operation. The two spectra have a different bandwidth; it is reduced by more than 15 cm^{-1} when in frequency comb operation. It is thus crucial to do all optical spectra measurements of the frequency comb while conserving the narrow beatnote properties during the measurement.

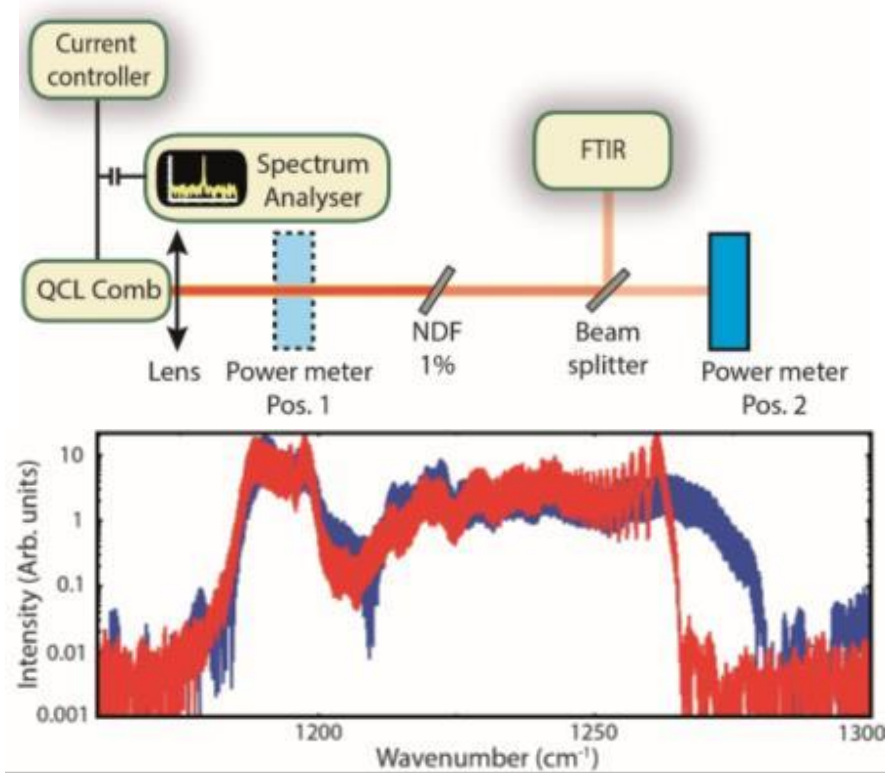


Figure 4. Schematic of the setup used for QCL comb characterization (top). Optical spectra (bottom) obtained under the same driving conditions without (red curve) and with (blue curve) optical feedback.

3.1.2 Dispersion compensation:

For the formation and stability of QCL combs, the dispersion plays a crucial role. The group delay dispersion (GDD) is the most convenient parameter to measure in order to characterize the dispersion of the laser. The method used to measure the GDD first described in Hofstetter and Faist [1999] is as follows:

- Measurement of a sub-threshold interferogram with an FTIR
- Isolation of the first satellite interferogram which corresponds to the interference with photons having experienced one more round trip in the laser cavity (see Figure 5)
- Extraction of the phase spectrum accumulated after one round trip in the laser cavity by Fourier transformation
- The Phase spectra is derived to obtain the dispersion and the value of the GDD.

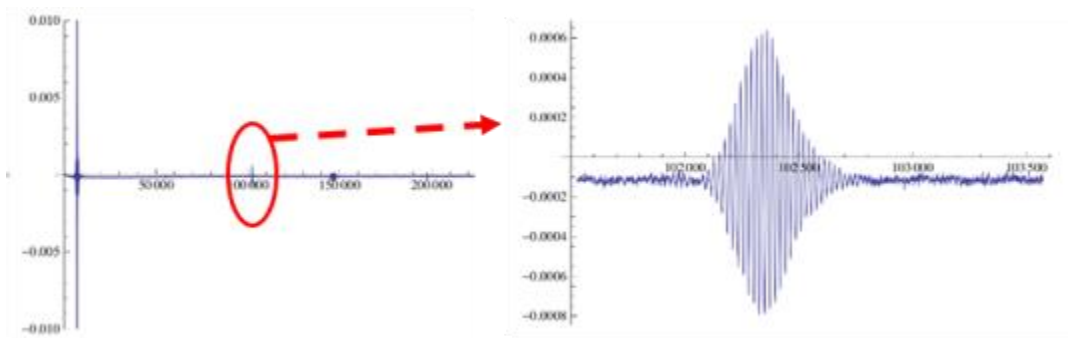


Figure 5. Subthreshold interferogram (left) and zoom on the first satellite (right).

A strong effort in order to compensate the materials natural dispersion was done. The first strategy was to use a Gires-Tournois (GTI) approach. Figure 6 shows the principle of such approach: a layer is deposited on one facet of the laser cavity and covered by a gold layer. Due to the refractive index mismatch between the laser cavity and the deposited layer, a partial reflectivity occurs at the interface; the gold layer on the other side of the deposited layer acts as a 100 % reflectivity mirror. As shown in Figure 7, such configuration provides a modulation of the GDD due to the periodic phase modulation. Several material combinations for the deposited layer were tested in order to obtain different values of GDD correction; a 1D simulation based on the matrix transfer formalism was used to design the deposited layers for the GTI coating.

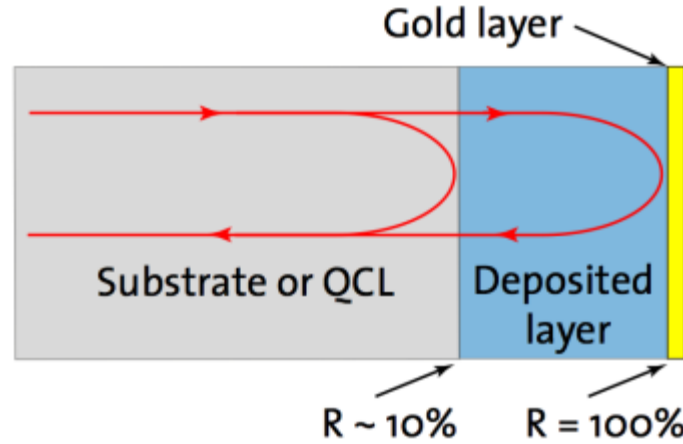


Figure 6. Schematic of a Gires-Tournois (GTI) coating principle

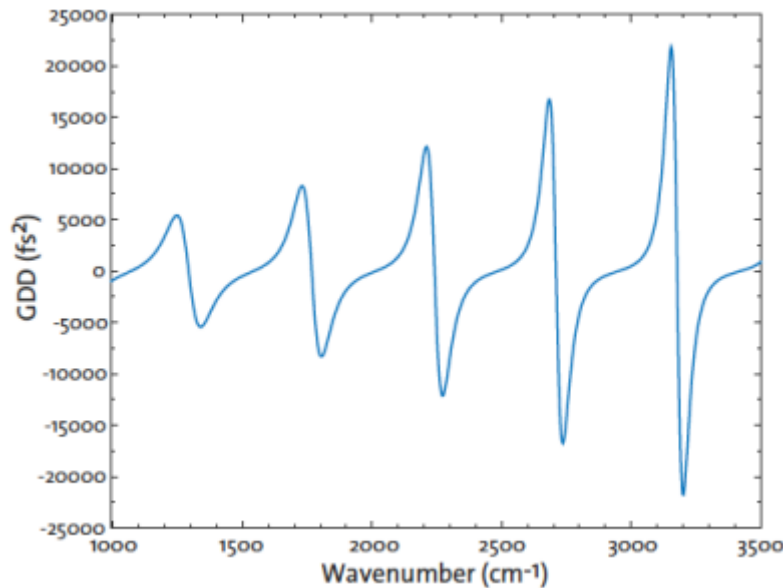


Figure 7. Group delay dispersion (GDD) induced by a GTI coating.

As published in Villares et al. [2016], using the GTI approach allowed us to improve the comb operation of a QCL. Figure 8 shows the Voltage-Optical power as a function of current (LIV) characteristics at different temperatures of a laser with a simple high reflectivity (HR) coating ($\text{Al}_2\text{O}_3/\text{Au}$). The comb operation regime occurs only on a small portion of the laser dynamical range. Figure 9 shows the LIV characteristics of a laser with a GTI coating (alternating layers of Al_2O_3 and SiO_2 and with an Au layer as a last layer). In this case the laser operates in the comb regime on the full dynamical range as shown by the narrow beatnote observed in Figure 10. Without coating, the GDD of those lasers emitting around 1320 cm^{-1} wavenumber was positive; therefore as shown in Figure 11 the GTI coating has been designed to add a negative GDD at this wavenumber. The discrepancy between the simulated and measured

induced GDD at wavenumbers around 1300 cm^{-1} is attributed to the absorption for SiO_2 at those wavelengths.

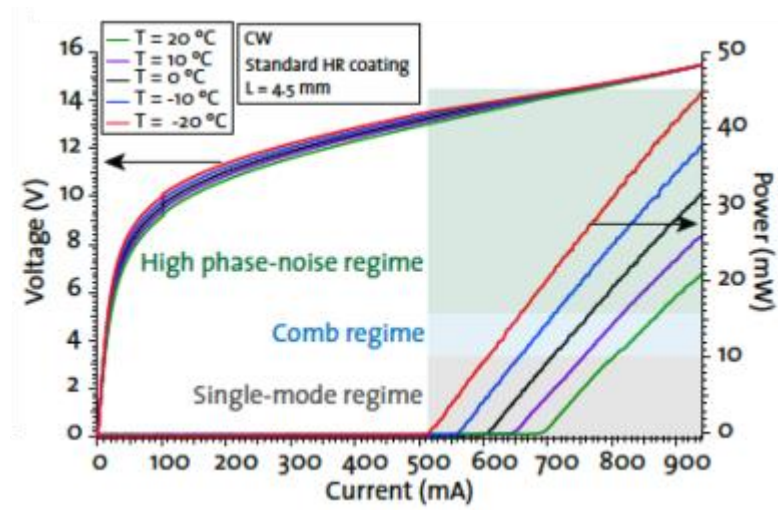


Figure 8. Measured LIV characteristics of a HR coated laser at different temperatures.

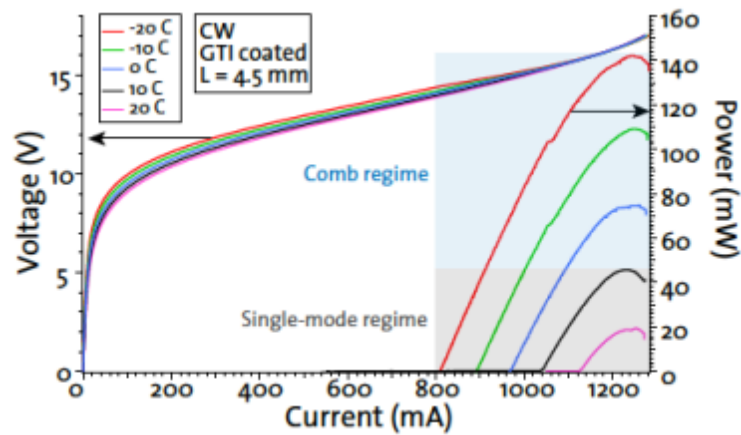


Figure 9. Measured LIV characteristics of a GTI coated laser at different temperatures.

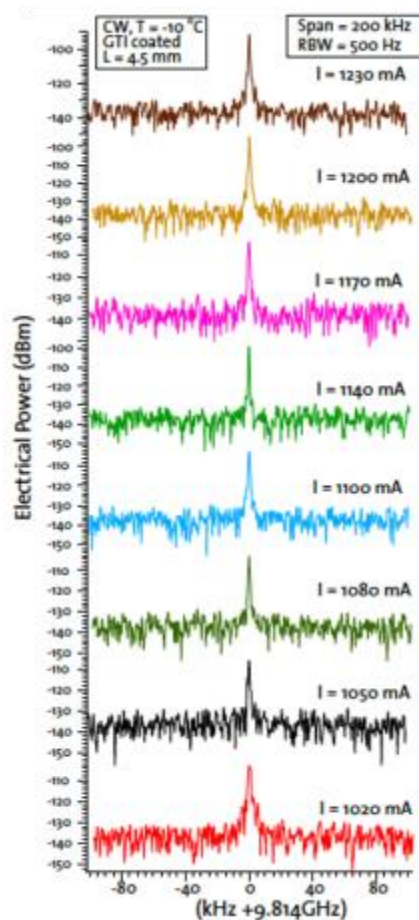


Figure 10. Measured RF beatnotes at -10C for different currents.

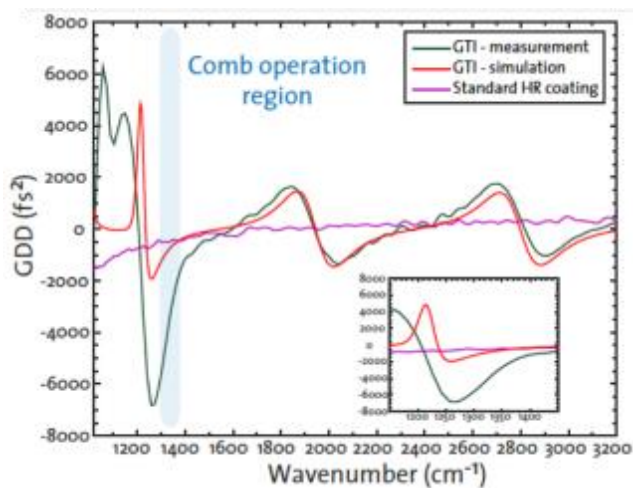


Figure 11. Measured GDD induced by an HR coating and a GTI coating together with the simulated GDD induced by the GTI coating.

In order to avoid absorbing materials and to reach greater values of negative induced GDD, other combinations of coating materials have been tested. Figure 12 shows for example the simulated and measured GDD induced by a GTI made of Al_2O_3 , YF_3 , Ge and Au layers.

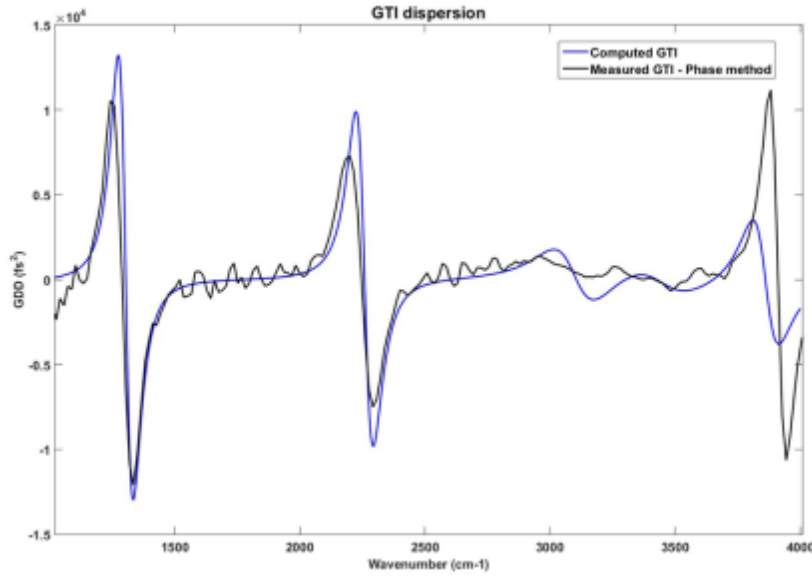


Figure 12. Simulated and measured GDD induced by a GTI coating made of Al_2O_3 , YF_3 , Ge and Au.

Even if the approach of using GTI coatings for improving the comb operation of the lasers gave promising results, it suffers from strong limitations. The first one is that the GTI coating needs to be done on each laser; it is a time-consuming procedure which requires very good control of the deposited layer thicknesses to reach the targeted wavelength. In addition, the working principle of the GTI coating implies that the deposited coating acts as a cavity; this leads to high optical power in the coating layers which turns out to be a problem for high power QCL combs. As shown in Figure 13, many coatings “exploded” due the absorption of a portion of the high optical power in the coating layers. Due to those reasons, the approach of compensating the dispersion directly by engineering the waveguide was also explored.

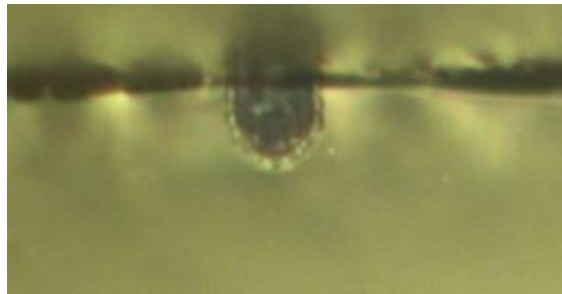


Figure 13. Optical microscope image of the back facet of a laser after explosion of the GTI coating.

The approach eventually adopted for dispersion compensation was to work directly on the waveguide design. COMSOL simulations were used in order to determine the dependence of the GDD as a function of the laser ridge width (see Figure 14) and as well to optimize the top cladding design for optimal GDD values. As described in Bidaux et al. [2017], coupling a plasmonic mode to the ridge optical mode allows to change significantly the GDD. Simulations illustrating this property are shown in Figure 15.

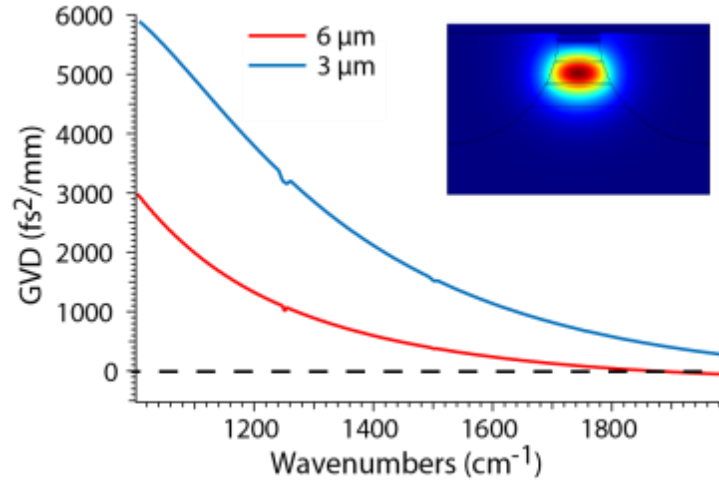


Figure 14. Simulated group velocity dispersion (GVD) as a function of the wavelength for two different laser ridge width. Inset: optical mode profile simulation with COMSOL.

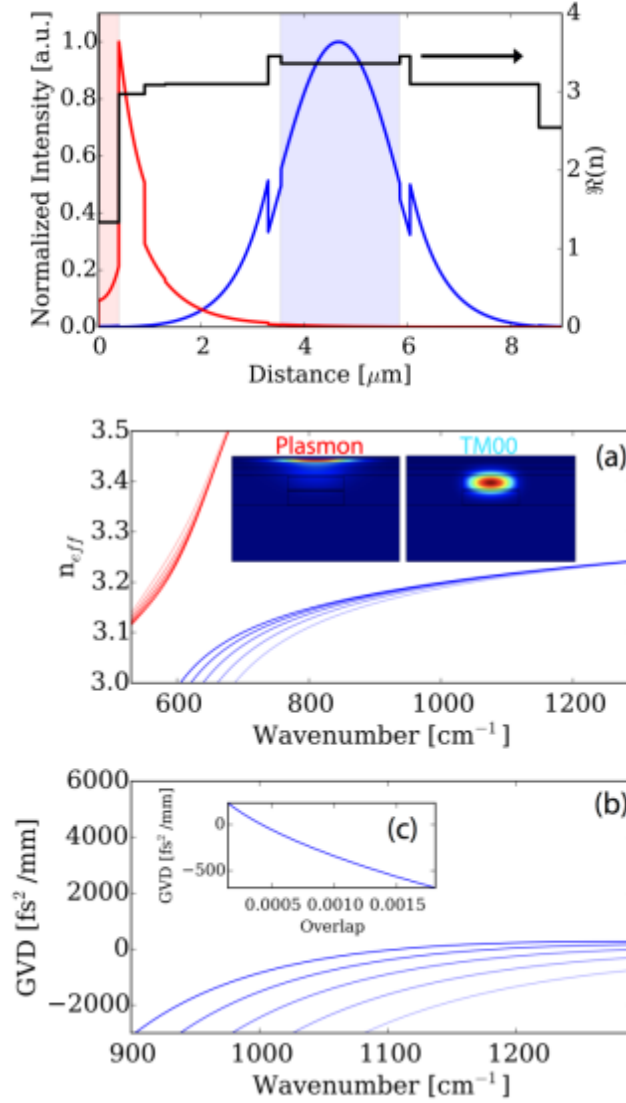


Figure 15. Simulated cross section of the plasmonic (red curve) and ridge optical (blue curve) mode as a function of the vertical position (top). Dispersion of the refractive index for the plasmonic (red curve) and ridge optical (blue curve) mode for different cladding thicknesses (middle) with inset showing mode profile simulations for the plasmonic (left) and ridge optical (right) mode. Simulated GVD of the ridge optical mode for different top cladding thicknesses (bottom).

3.1.3 Active region design and growth

QCL combs at 1250 cm^{-1}

The final design for the QCL comb emitting with wavenumbers around 1250 cm^{-1} is a two stack design, meaning two central emission wavelengths in order to have a broader

bandwidth, obtained by genetic optimization. The simulations of each stack are shown in Figures 16 with the predicted total modal gain in Figure 17.

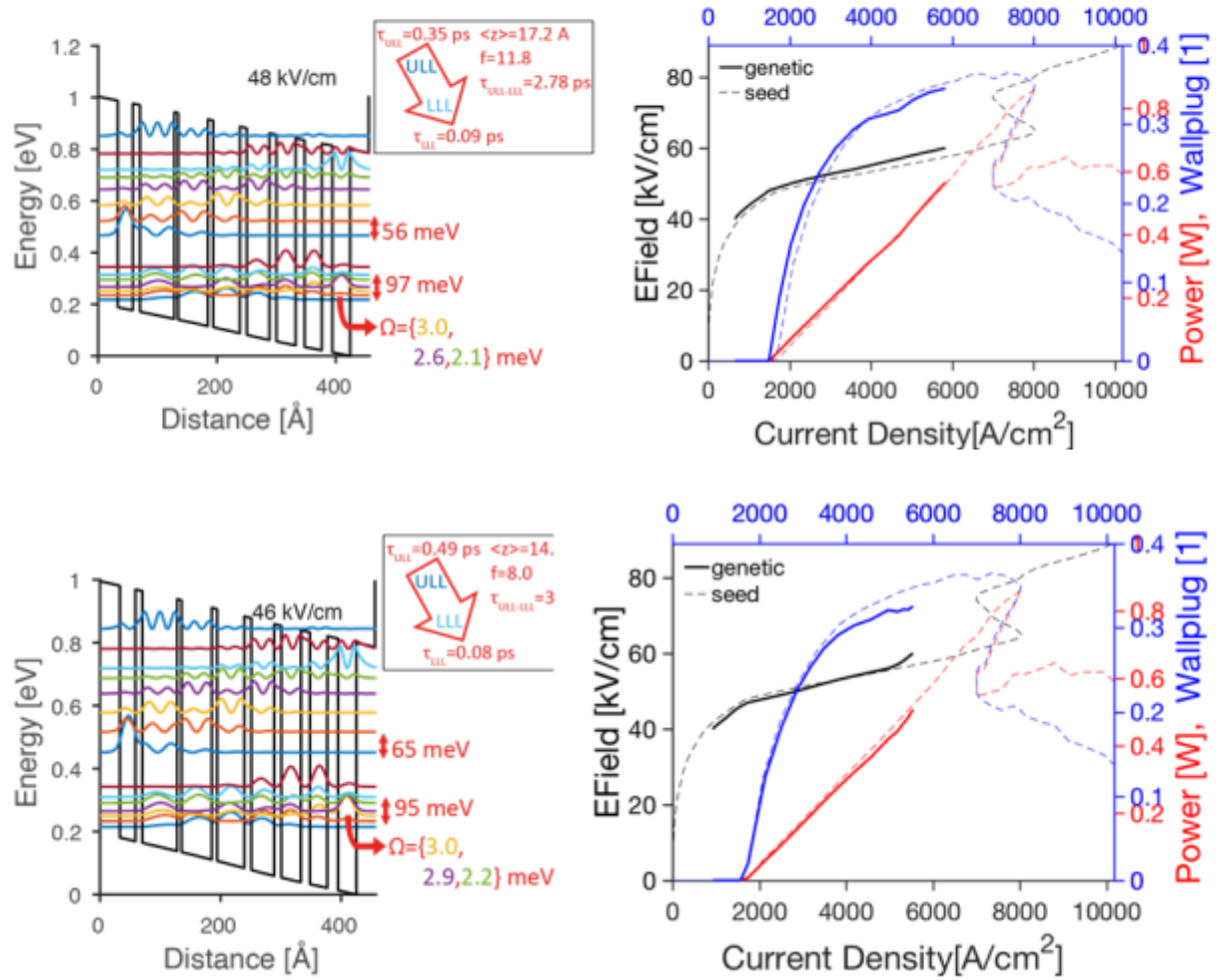


Figure 16. Simulated wavefunctions distribution (left) and LIV (right) for the structure of each stack.

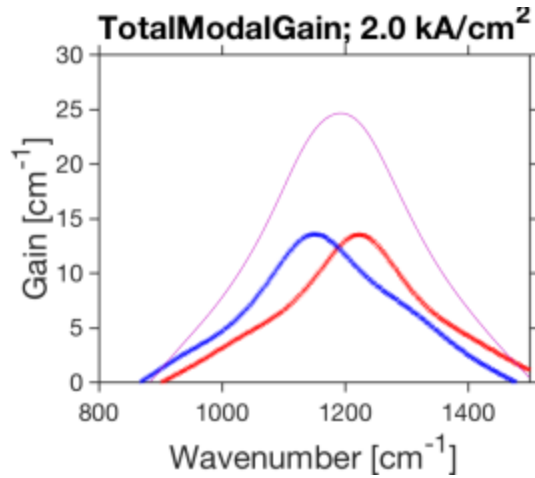


Figure 17. Simulation of the gain for each stack and total gain.

The QCL combs resulting from this design gave outstanding power performances and are to date the most powerful QCL combs reported [Jouy et al. 2017]. Figure 18 shows the LIV characteristics as well as the wall plug efficiency for these devices.

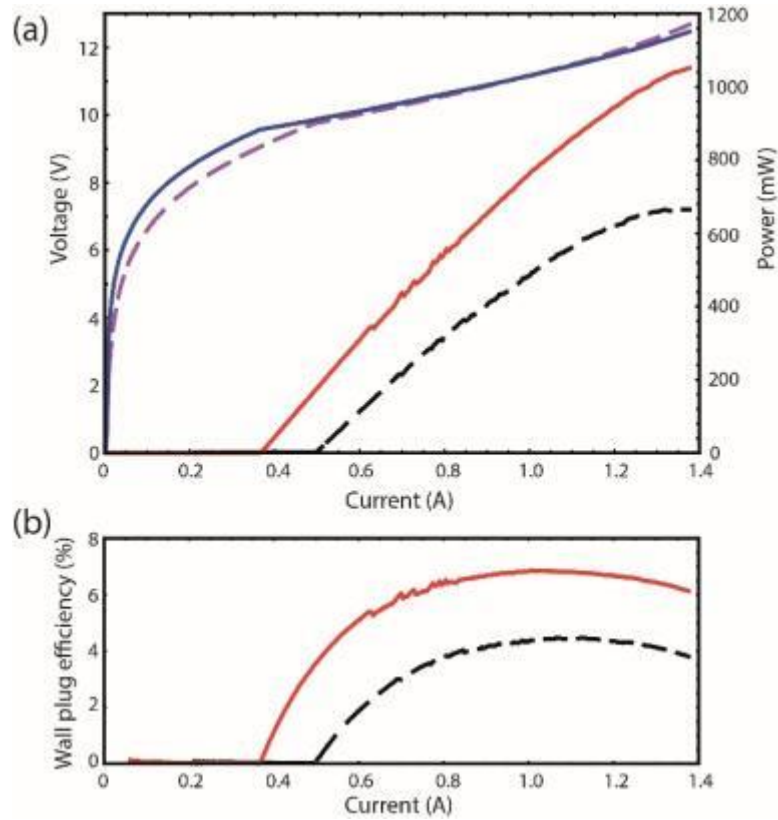


Figure 18. LIV characteristics (a) and wall plug efficiency of the laser at -15°C (full line) and 20°C (dashed lines).

The beatnote, spectra, beatnote frequency and beatnote width at -20 dB for different driving currents and at -15°C are presented in Figure 19 a), b) and c) respectively, showing comb operation up to roll over with very strong beatnote SNR.

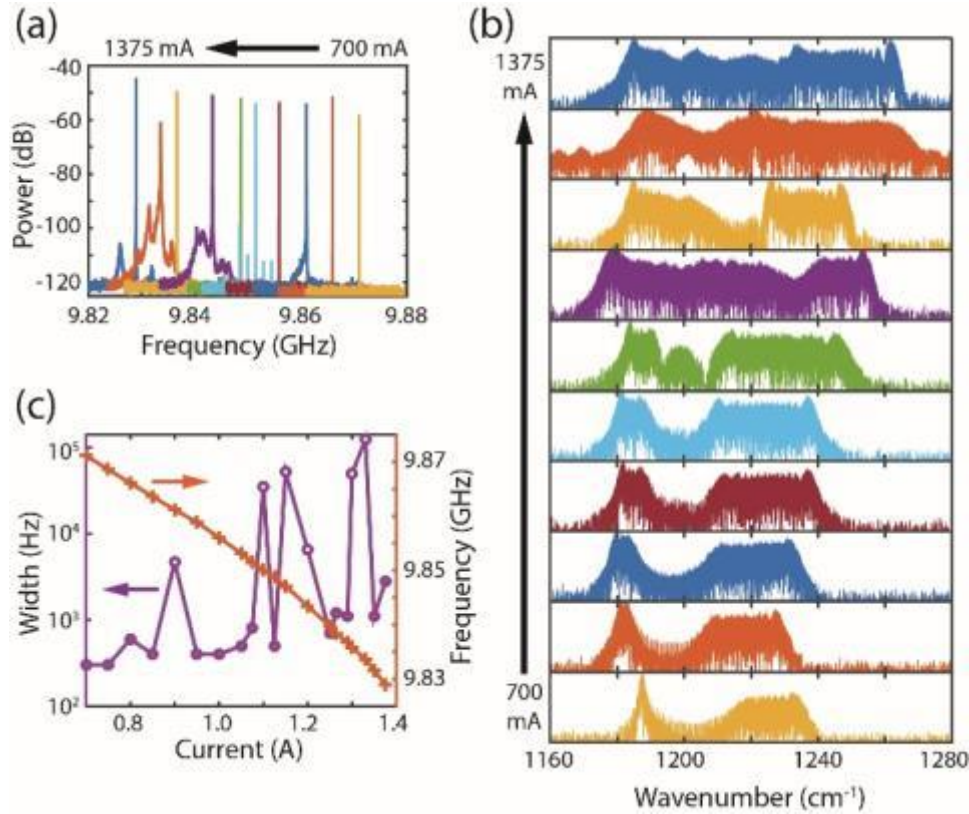


Figure 19. rf beatnote (a) and corresponding optical spectra (b) for different currents at -15°C. (c) Summarizes the beatnote frequency and width at -20 dB.

Figure 20a shows the beatnote at -15°C for a current of 1375 mA with a narrower bandwidth. Under those driving conditions, the optical output power is above 1 Watt and the beatnote present an SNR above 60 dB. The spectra at 1375 mA for temperatures of -15°C and 20°C are shown in Figure 20b. At -15°C, a total bandwidth of 85 cm⁻¹ with a power of 1.05 W is achieved and a continuous bandwidth of 82 cm⁻¹ has a power per mode above 1 mW with an average power of 4.1 mW. At room temperature, a total bandwidth of 75 cm⁻¹ with a power of 0.664 W is achieved and a continuous bandwidth of 73 cm⁻¹ (excluding 5 modes for wavenumbers in the vicinity of 1225 cm⁻¹) has a power per mode above 1 mW with an average power of 2.99 mW. At room temperature, the beatnote is more robust and is a narrow peak on all the dynamical range beside at 1100 mA (Figure 20c).

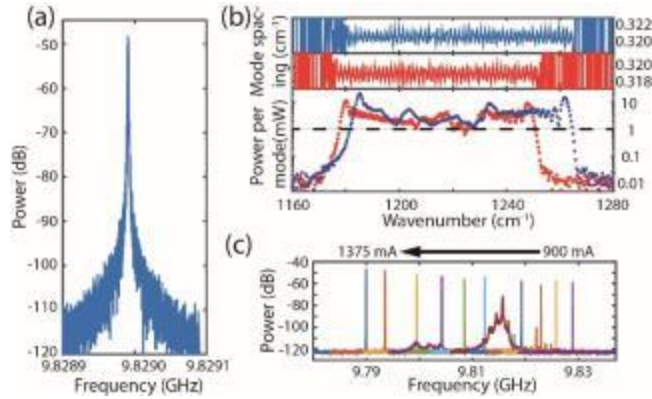


Figure 20. a) rf beatnote at -15°C and 1375 mA. b): mode spacing and power per mode at 1375 mA for temperatures of -15°C (blue) and 20°C (red). c) rf beatnote for different currents at 20°C .

Other lasers from the same process gave broader QCL comb emission bandwidth. An example of a spectra and the corresponding beatnote of a 4.5 mm uncoated laser operated at 0°C and 1000 mA is presented in Figure 21 with a bandwidth above 105 cm^{-1} . This value is still lower than the targeted 150 cm^{-1} ; the most promising strategy to reach this bandwidth goal would be to add a third stack in the active region to broaden even more the gain bandwidth.

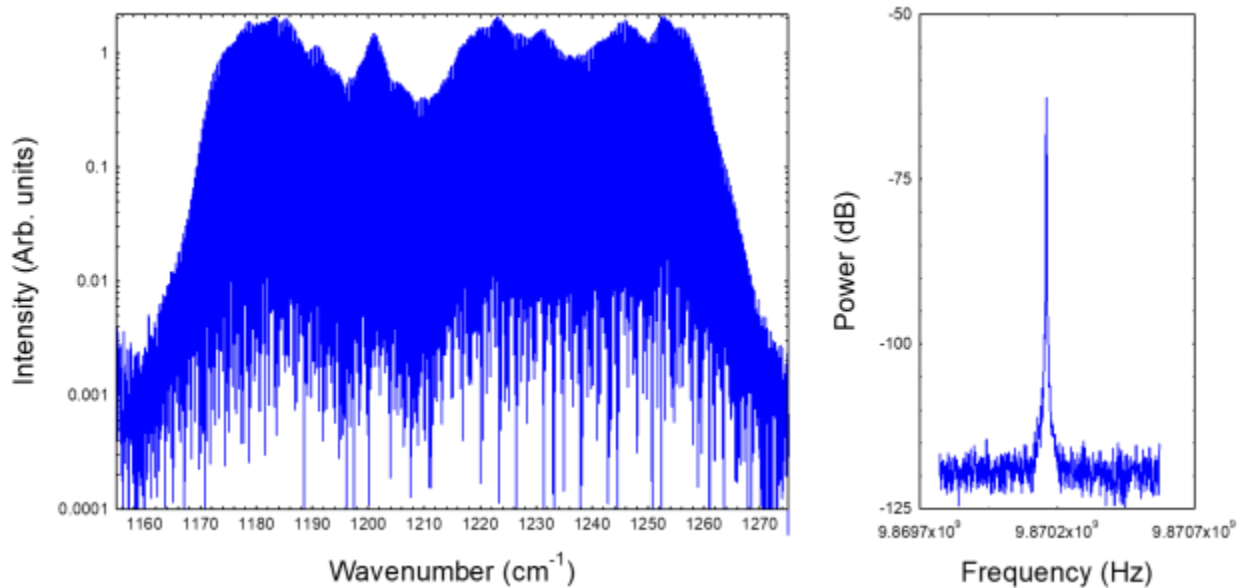


Figure 21. Log scale spectra (left) and corresponding beatnote (right) for a temperature of 0°C and a current of 1000 mA.

Two lasers were combined in a dual OFC setup, generating the multi-heterodyne spectrum shown in Figure 22 where the lasers are 4.5 mm long and are operated one at 0°C and

the other at +15°C with currents of approximately 1270 and 1386 mA respectively without further stabilization. Even if uncoated, each laser has an optical output power above 400 mW in those driving conditions. About 215 peaks corresponding to an optical bandwidth of more than 70 cm^{-1} are observable between 200 and 600 MHz with a spacing of approximately 1.77 MHz.

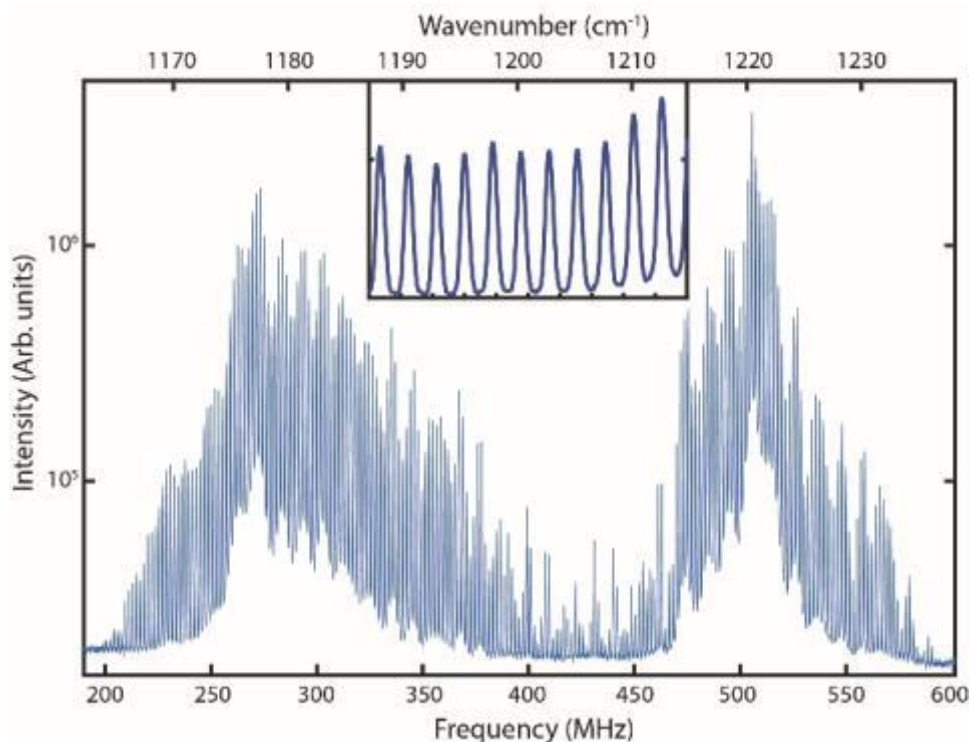


Figure 22. Multi-heterodyne spectra with 20 ms integration time and zoom in (inset) between 230 and 250 MHz.

QCL combs at 1025 cm^{-1}

The latest active region developed for emission centered around 1025 cm^{-1} is a one stack active region. The LIV characteristic of a 4.5 mm HR coated laser is shown in Figure 23 for different temperatures. The comb characterization is presented in Figure 24 for different driving currents at -15°C. It presents a narrow beatnote and thus a comb operation on the entire dynamical range, giving more than 300 mW of output power and a bandwidth above 50 cm^{-1} for the highest currents. Here again the power is much above the targeted optical power of 50 mW but the bandwidth is below the targeted 150 cm^{-1} . Here as well, adding another stack will ultimately allow further increased bandwidth.

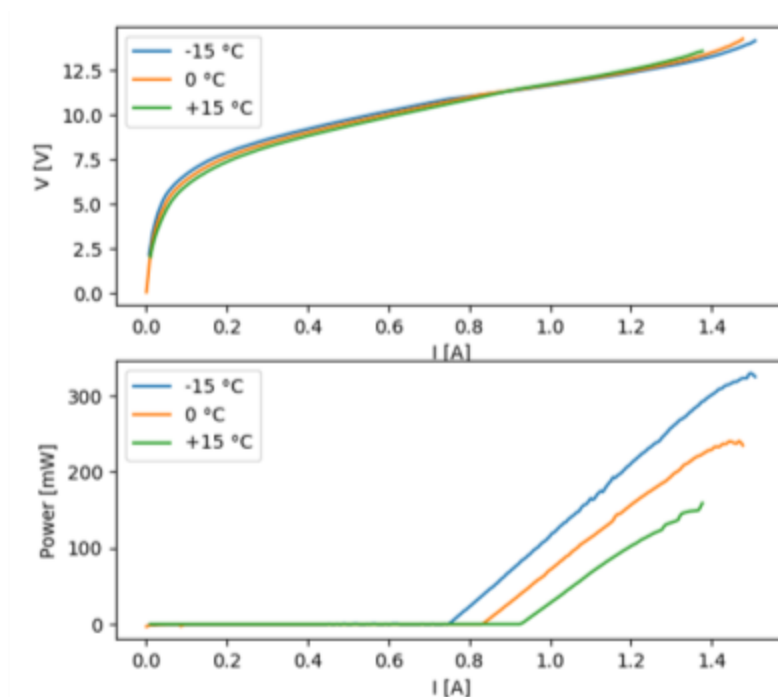


Figure 23. LIV characteristics of a 4.5 mm HR coated device at different temperatures.

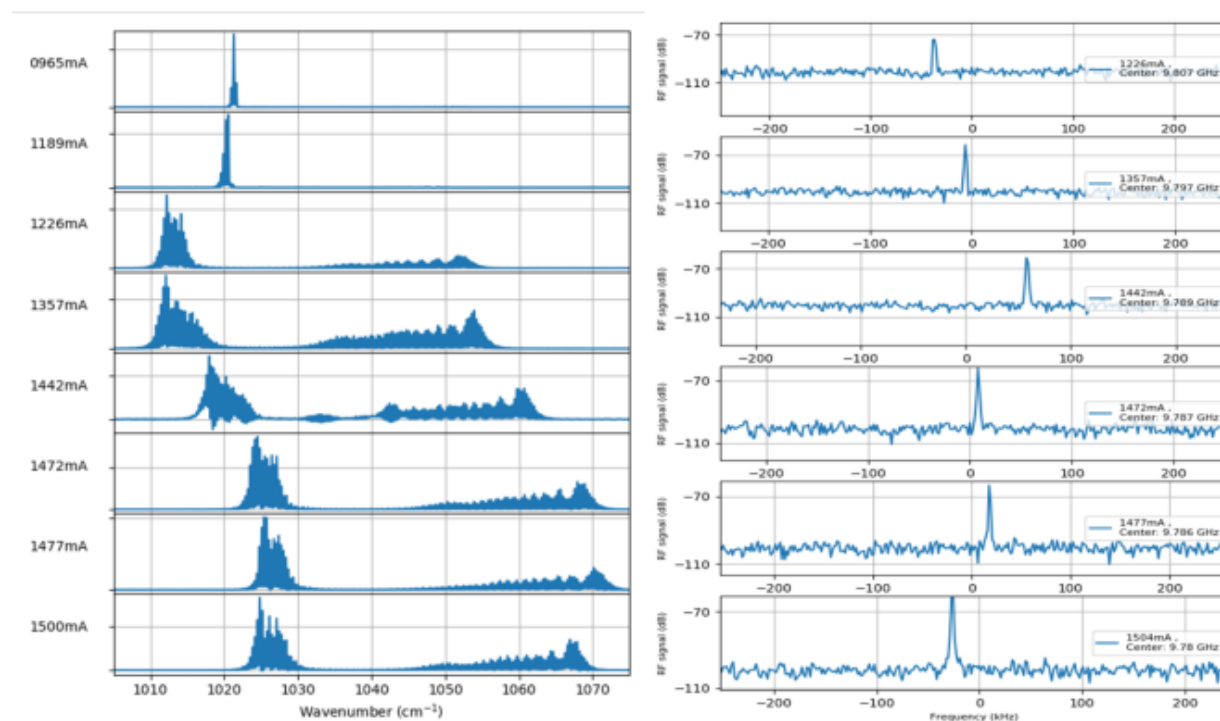


Figure 24. Optical spectra at different currents for a temperature of -15°C (left) and corresponding RF beatnote (right).

3.1.4 Dual comb on a chip

In a dual comb setup, one source of noise is due to having two independent lasers. In particular, the multi-heterodyne signal drifts due to independent temperature fluctuations of both lasers. A strategy to overcome this problem was to have the two laser combs on the same chip in order to have the same temperature fluctuations on both lasers. To be able to fine tune the wavelength and the repetition frequency of each lasers independently using temperature gradient on the chip, additional heaters were placed on the side of each lasers. Two generations of heaters have been developed and are represented in Figures 25 and 26. The top one uses a shallow conducting low doped InP channel between the direct contact and the heating contact. Changing the flowing current between those two pads will change the heat dissipated next to the laser due to the resistance of the low doped InP layer. Even if such configuration works for tuning the wavelength of one laser with respect to the second laser, sharing the direct contact pad for both driving the laser and driving the heater makes this design weak for laser stability. Therefore a second generation was developed in which the heaters are additional ridges on the side of each laser. Such configuration provides separate driving channels for each lasers and each heaters.

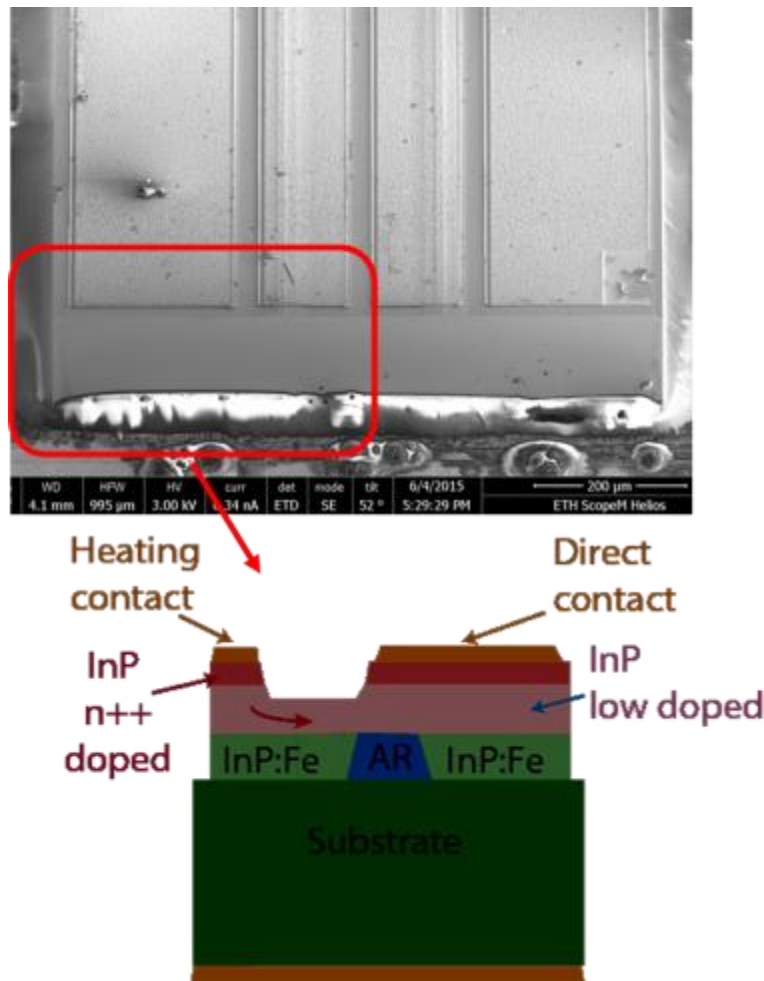


Figure 25. SEM picture of a dual comb on a chip device from the first generation (top). Schematic of the heater principle for the first generation (bottom).

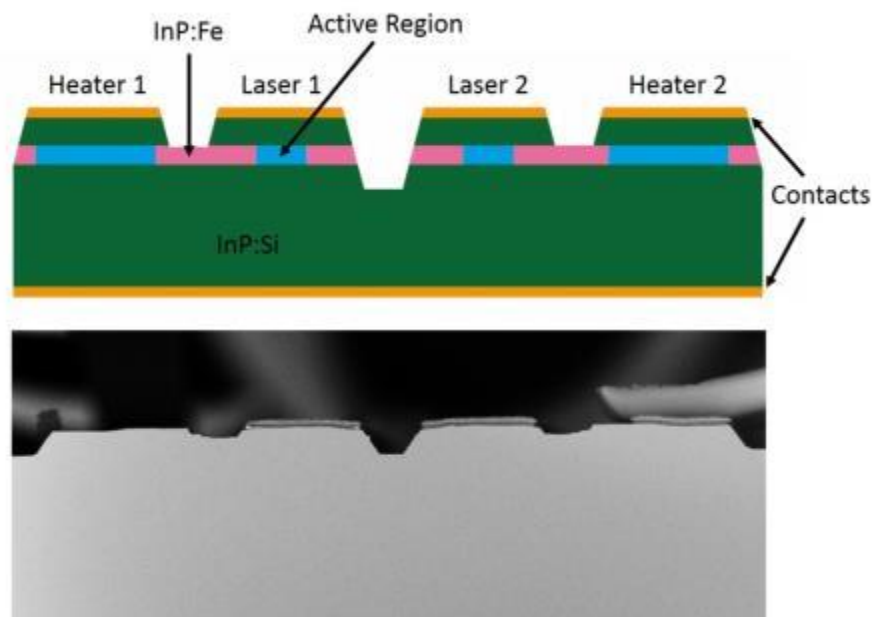


Figure 26. Schematic of the cross section of the second generation dual comb on a chip (top). SEM picture of the front facet of a sample from the second generation dual comb on a chip (bottom).

The performance of these devices has been reported in Villares et al. [2015]. For this 3 mm HR coated device, the two lasers are driven using the same driver. The spectra of each laser is presented in Figure 27 without (top panel) and with heater on (bottom panel). It shows that engaging the heater brings the two combs to closer together. The effect of the heater on the beatnote frequency can be seen in Figure 28 where one beatnote stays at the same frequency but the other beatnote frequency sweeps across more than 500 kHz. Finally, a multi-heterodyne spectra corresponding to an optical bandwidth of more than 32 cm^{-1} is shown in Figure 29 to show the good stability of the dual comb on a chip system.

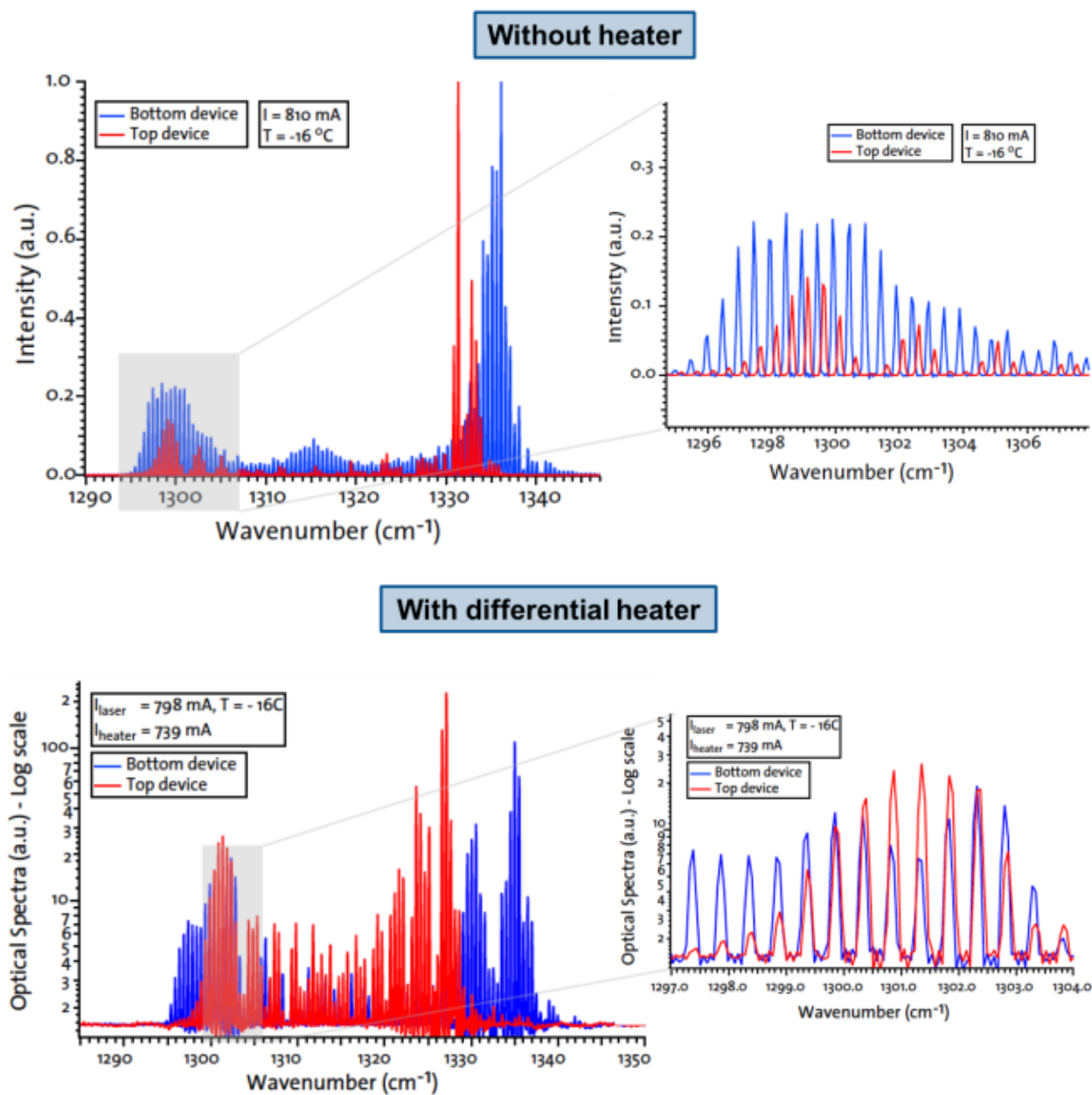


Figure 27. Spectra and zoom in of both lasers with (bottom) and without (top) current in the heater.

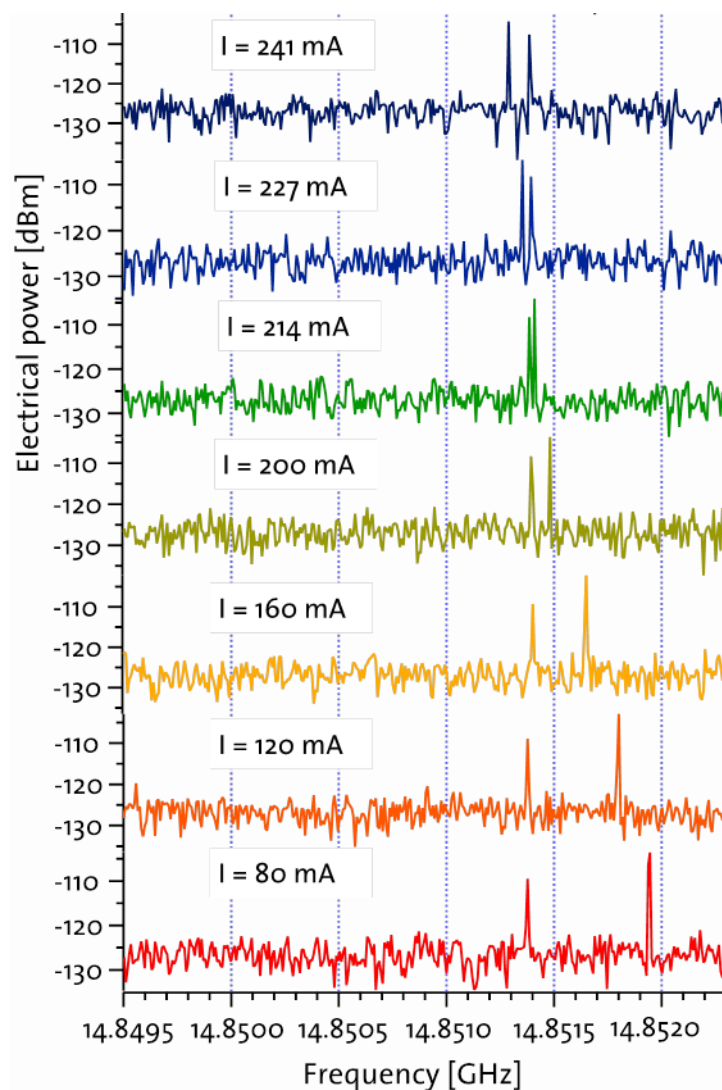


Figure 28. Beatnote of the two lasers on the dual comb on a chip device for different values of the current injected in one of the heaters.

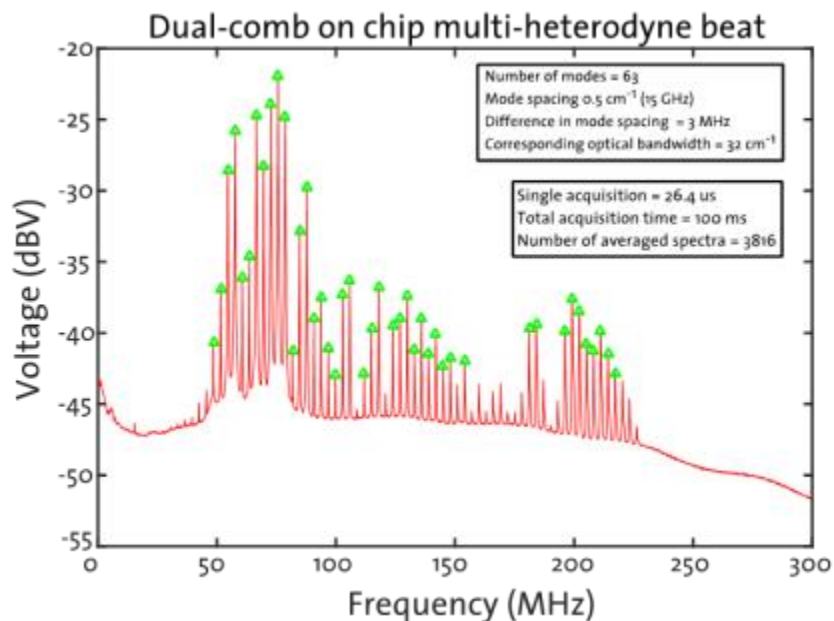


Figure 29. Multi-heterodyne spectra obtain from a dual comb on a chip device.

Dual comb devices were also fabricated in a second iteration. A 4.5mm long device was mounted epi-down in order to improve the performances of the lasers. The epi-down mounting bring the challenges of having a very flat surface to insure a good thermal and electrical contact of each lasers and heaters, to have good electrical isolation between each channels and to have a very precise alignment (accuracy in the order of 5-20 μm). Figure 30 shows the independent and simultaneous operation of the two lasers and Figure 31 shows the tuning of the spectra by more than one free spectral range when injecting 100 mA in one of the heater.

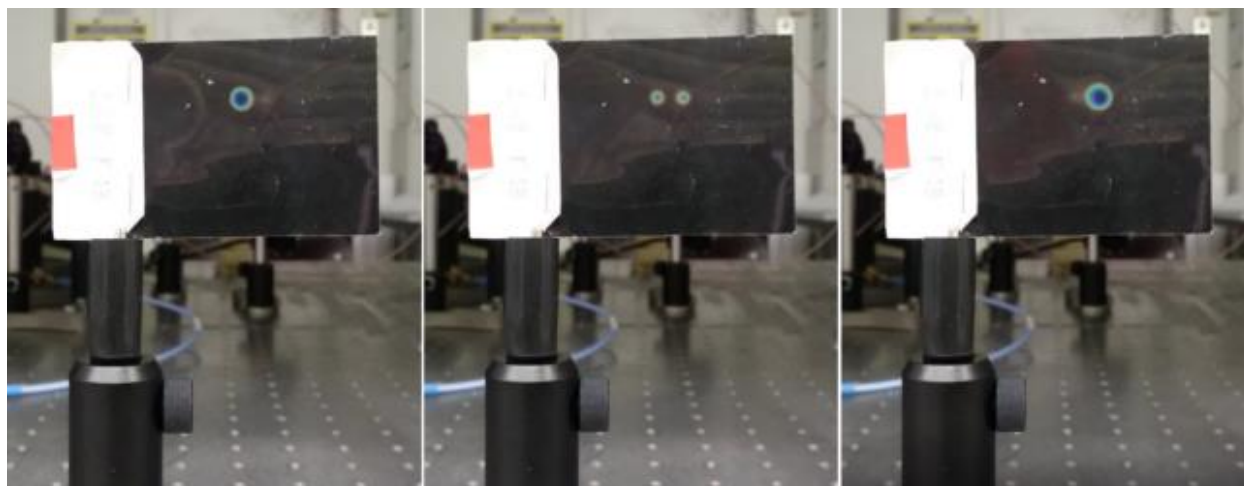


Figure 30. Picture of the beam on a thermal paper when a single laser (left and right panel) and two lasers (middle panel) on the dual comb on a chip are driven.

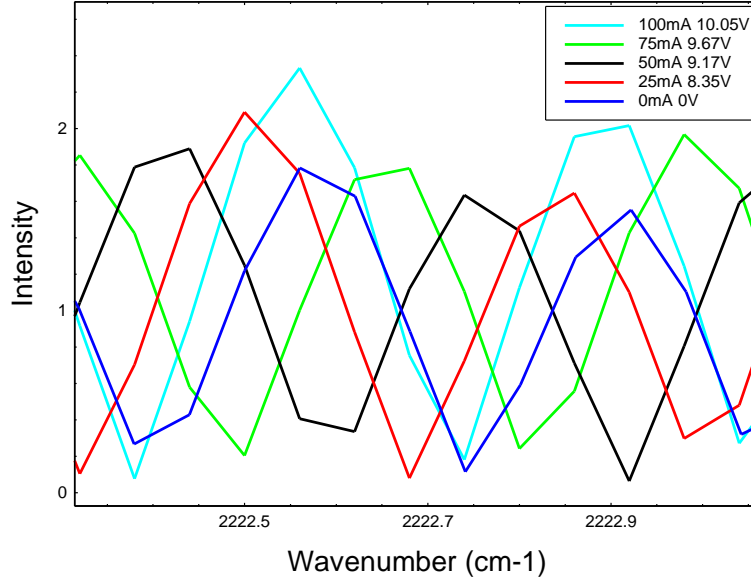


Figure 31. Shift of the optical spectra for a constant current on the laser for different values of the current in the heater.

3.2 Multi-heterodyne Signal Processing

3.2.1 F_{rep} tracking

Using free running lasers challenges the processor since the multi-heterodyne lines drift freely. Each line in a multi-heterodyne signal can be expressed by the equation:

$$f_n = \Delta f_{ceo} + n * \Delta f_{rep} \quad (1)$$

Due to the drift of the offset and repetition frequency of both lasers, the resulting multi-heterodyne signal also drifts. The measurement in Figure 32 shows the drift of the multi-heterodyne signal in the RF-domain after acquiring a number of subsequent measurements with the QCL dual-comb spectrometer. The multi-heterodyne spectrum of this measurement is shown in Figure 33. This drift needs to be taken into account for any multi-heterodyne processor. There have been many suggestions how to overcome these difficulties [Ideguchi et al. 2014, Yang et al. 2016, Hugi et al. 2017].

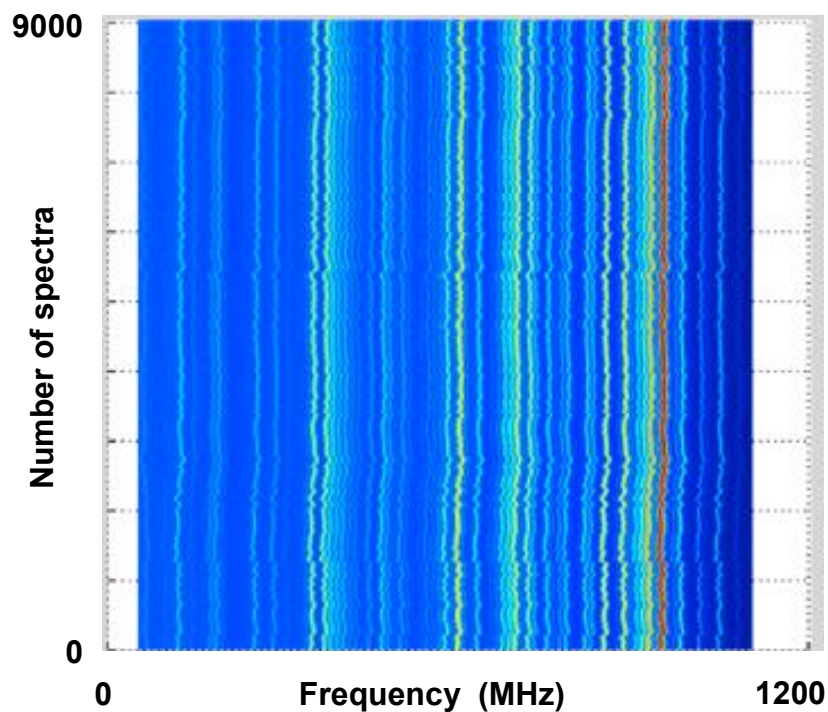


Figure 32. Uncorrected drift of the multi-heterodyne signal. The multi-heterodyne signal drifts due to noise in the laser over a number of subsequent multi-heterodyne acquisitions in the RF-frequency domain.

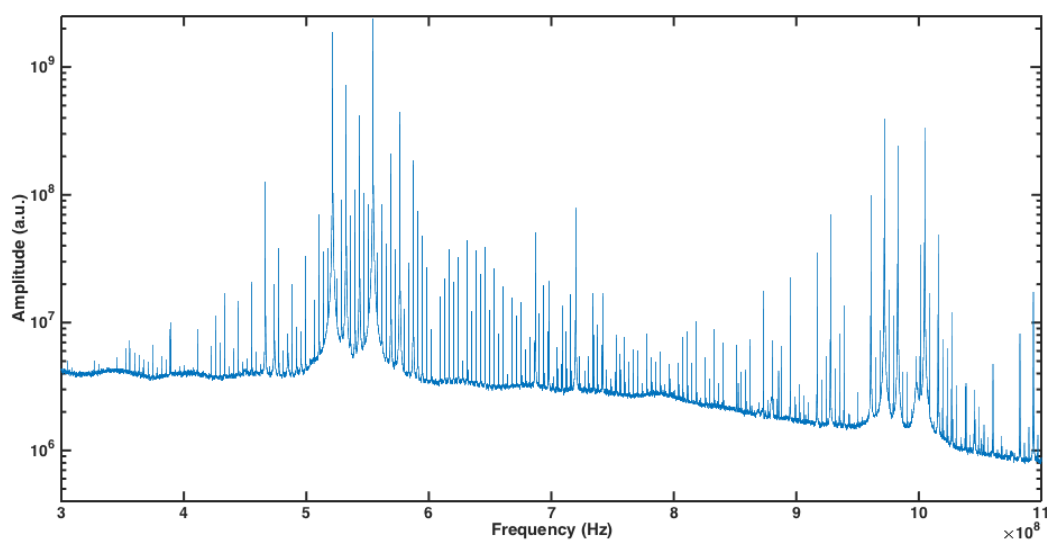


Figure 33. Multi-Heterodyne signal of a dual-comb QCL laser spectrometer.

Figures 34 and 35 shows a corrected multi-heterodyne spectrum where all of the heterodyne modes are aligned simultaneously.

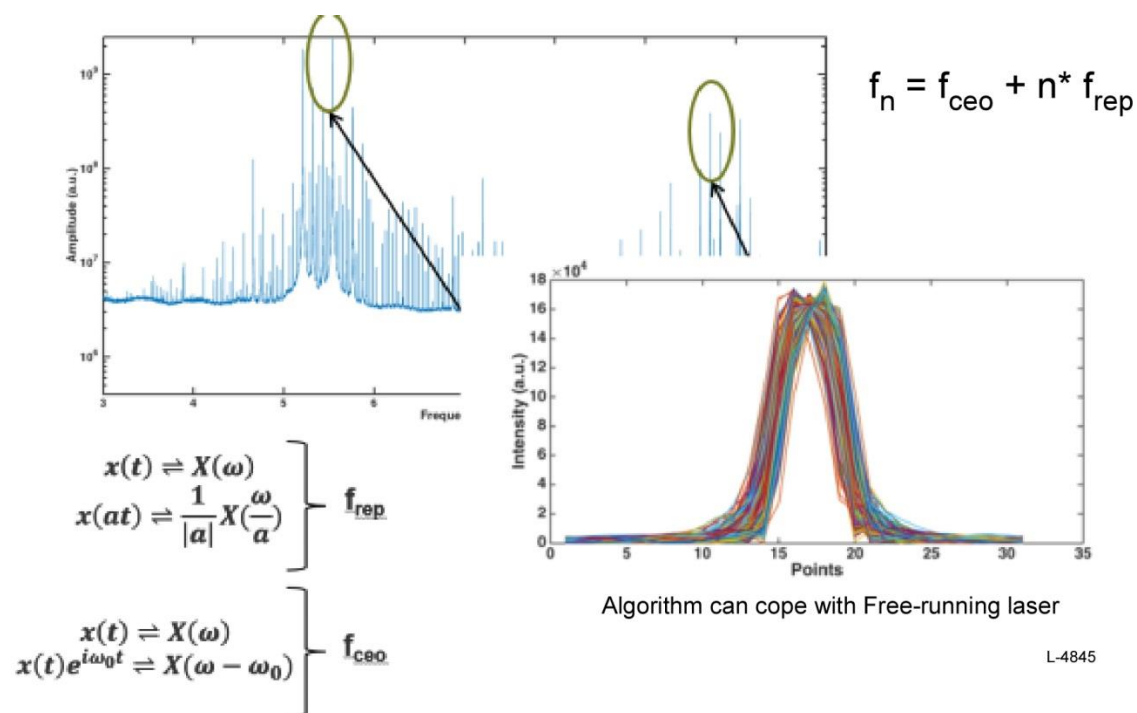
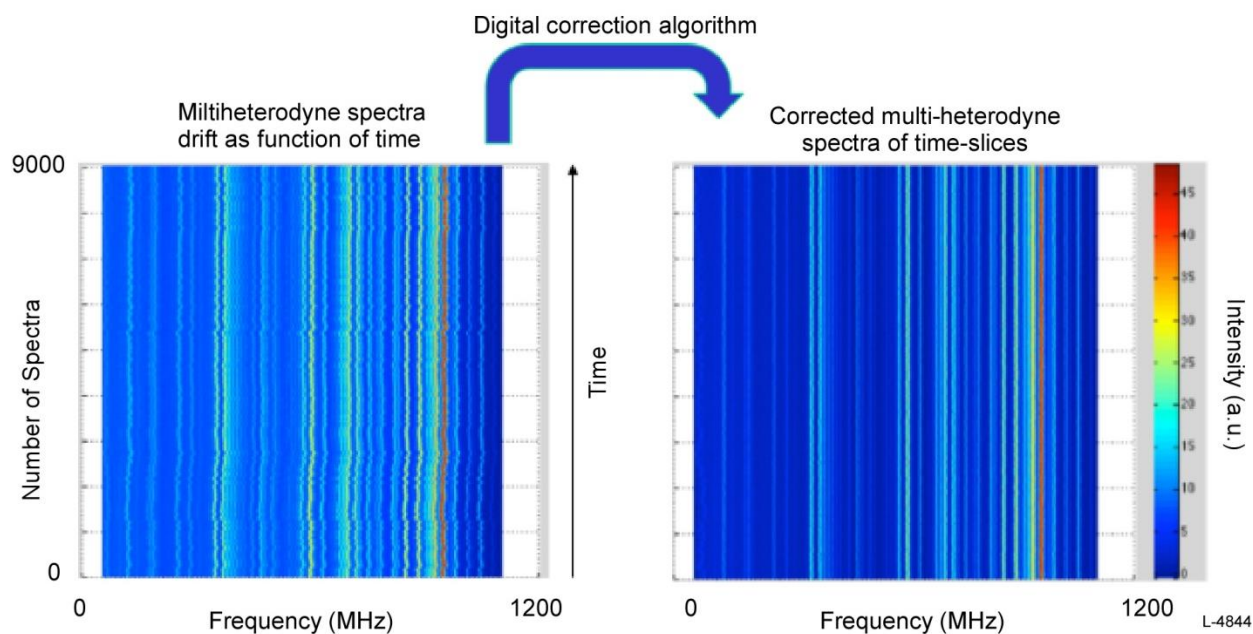


Figure 35. Aligned spectra at different point in the spectrum.

Measuring the drift of the repetition frequency and offset frequency of the multi-heterodyne signal allows us to correct these signals. After having measured the drift of the repetition frequency as well as the offset frequency, the mathematical operations to apply to the signal to correct for F_{rep} are:

$$\left. \begin{aligned} x(t) &\Rightarrow X(\omega) \\ x(at) &\Rightarrow \frac{1}{|a|} X\left(\frac{\omega}{a}\right) \end{aligned} \right\} f_{\text{rep}}$$

$$\left. \begin{aligned} x(t) &\Rightarrow X(\omega) \\ x(t)e^{i\omega_0 t} &\Rightarrow X(\omega - \omega_0) \end{aligned} \right\} f_{\text{ceo}} \quad (2)$$

These processing steps are however very computationally expensive and thus it is important to review implications on signal to noise ratio (SNR) of these different approaches prior to implementing the processor. Therefore, we investigated the possibility of achieving the same effect as a computational expensive F_{rep} detection using a master-slave setup of the QCLs. The assumption of the experiment was that we can keep the master comb free-running and slave the second comb to it, resulting in a stabilized multi-heterodyne spectrum that is a much easier computational work-load on the processor.

The setup to carry out the experiment to reduce the computational load on the processor is illustrated in the Figure 36. Comb 1 is kept free-running. A phase-lock loop which acts on the multi-heterodyne signal drift is installed. A single line of the multi-heterodyne signal is filtered out with a bandpass filter centered at 162 MHz. This signal is fed into the correction loop to stabilize the multi-heterodyne signal. A proportional integral derivative (PID) control loop is used to generate the correction signal which acts on the current input of Comb 2.

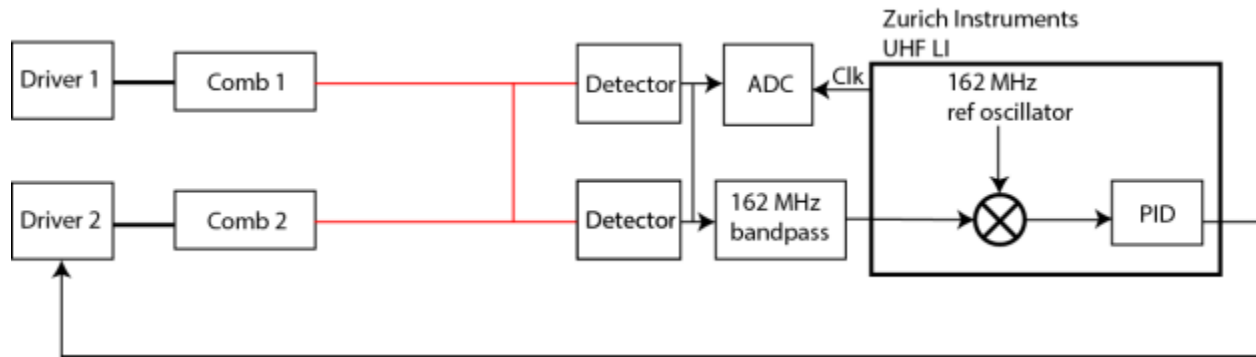


Figure 36. Master-slave setup to investigate the possibility to reduce the computational load on QCL processing.

The result of the locked multi-heterodyne signal is shown in the Figure 37. The dual-comb setup was operated in a folded configuration. This configuration is advantageous for this experiment for two reasons. First, it allowed us to observe more peaks in the same bandwidth. Second, it was a well suited configuration to observe the main peak on which the lock stabilizes and compare it to a peak which is far away in the optical spectrum due to the folded multi-heterodyne spectrum.

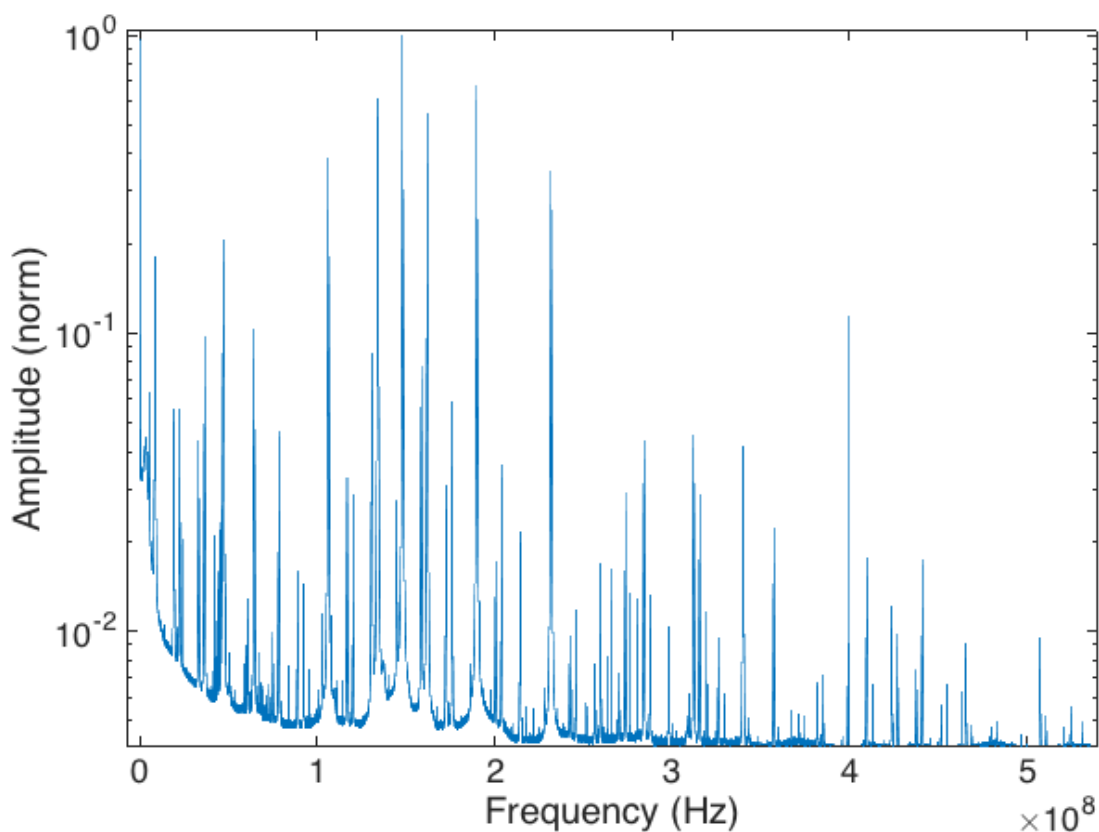


Figure 37. Master-slaving results of the dual-comb spectrometer.

Figure 38 shows the zoomed in result. It becomes very apparent that the locking strength on slave laser is not very efficient. Only roughly 10% of the emission power is locked. Furthermore, observing the coherence of the neighboring peaks, for example peak #23 which is 5.75 cm^{-1} away from the main locked peak is already loses most its coherence. This is because the locking loop only controls one parameter of the lock by stabilizing one single parameter of the laser.

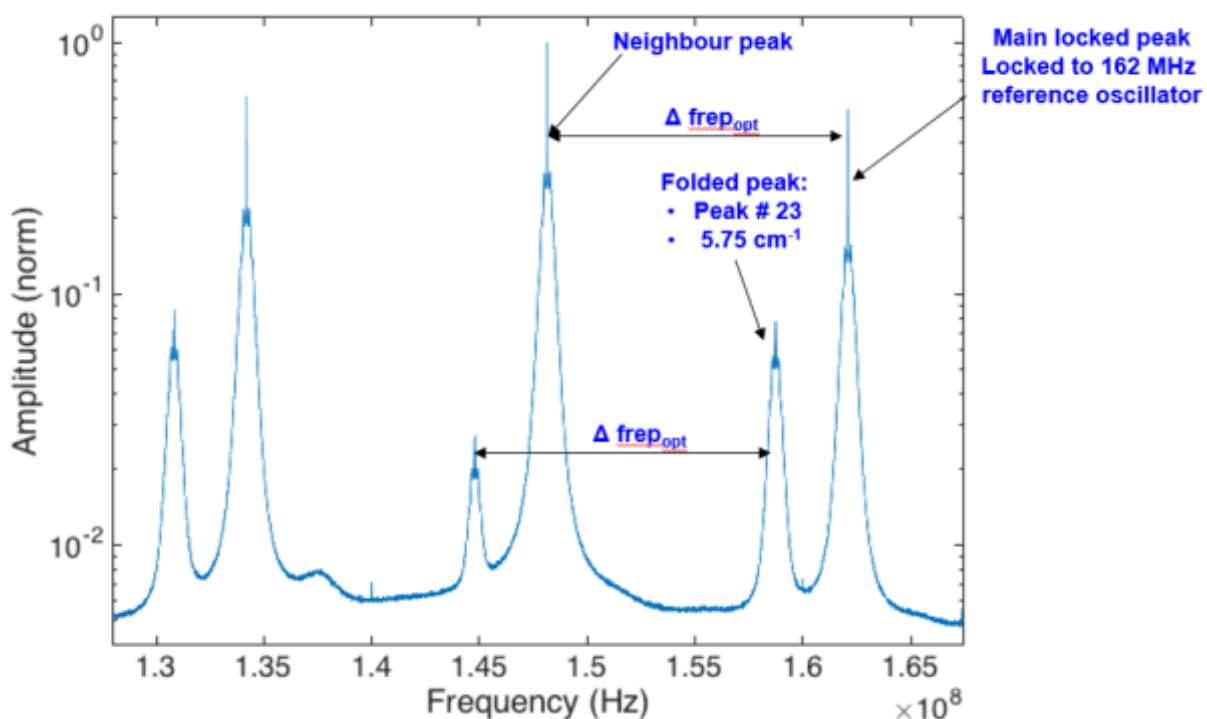


Figure 38. Zoomed in result from the stabilized multi-heterodyne result.

This problem is further illustrated in the Figure 39. In the main peak, the amount of power in the lock is about 10%, whereas the already peak #23 has a substantially larger bandwidth of 100 kHz. This shows that the loss of coherence with such an approach amount sot 17 kHz/cm⁻¹.

The marginal results of the locking led to the decision to abandon its use in prestabilizing the combs, focusing instead on an appropriate software solution which combines processing speed and good SNR.

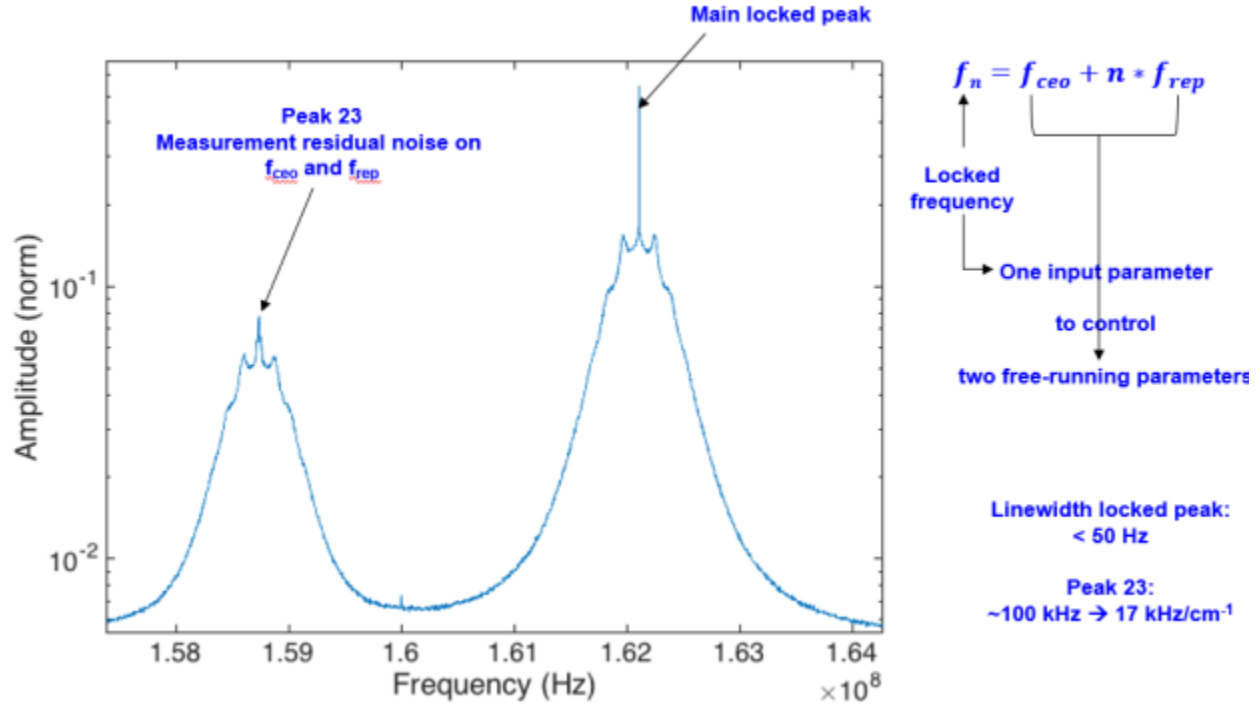


Figure 39. Locking loop only controls one parameter, whereas there are two free-running parameters to control.

3.2.2 Coherent averaging

Traditional dual-comb spectrometers realized with fiber combs usually run in a fully stabilized setup. The multi-heterodyne signal is acquired in the time domain in a coherent fashion, allowing the signal to be averaged coherently in the time domain. The coherent averaging has the advantage of a better dynamic range of QCL comb measurements. Coherent vs incoherent averaging gain compare as followed. The coherent gain is given by

$$SNR_{coh}gain(dB) = 10 * \log(N) \quad (3)$$

Whereas the incoherent gain is limited to

$$SNR_{incoh}gain(dB) = 10 * \log(\sqrt{N}) \quad (4)$$

Given these two expressions, coherent averaging should be chosen due to the increased dynamic range. Initially, the algorithm developed was based on coherent averaging. The measurement of the F_{rep} and F_{ceo} drift was carried out prior to resampling. The resampling was carried out using Eq. 2.

However, for free-running combs F_{rep} and F_{ceo} of the multi-heterodyne signal both drift, so the acquired time-domain signal needs to be corrected for these drifts prior to carrying out the coherent averaging. The coherent averaging in itself is computational a very simple step, however extracting the drift of F_{rep} and F_{ceo} as well as the required resampling of the time domain signal are extremely computationally intensive. Therefore, we decided to compare coherent averaging to non-coherent averaging on a SNR basis to evaluate which algorithm will in the end be implemented in the real-time processor.

In order to explore the gain in SNR with coherent averaging, the digital signal drift algorithms were used to get a very accurate result in the drift of F_{rep} and F_{ceo} . Subsequently, the time domain signal was resampled to correct the drift in the time domain. The time domain signal was subsequently averaged incoherently in the time domain and afterwards an FFT was performed to compare the dynamic range gain. In order to correct for as little drift as possible, a measurement was carried out with the hardware lock in place.

Figure 40 shows the signal gain when applying the correction algorithm on the time domain signal. The multi-heterodyne signal increases by a factor of 5 dB. The same signal can afterwards be coherently averaged in the time-domain. The coherently averaged signal is shown in Figure 40 right, exhibiting the expected signal gain.

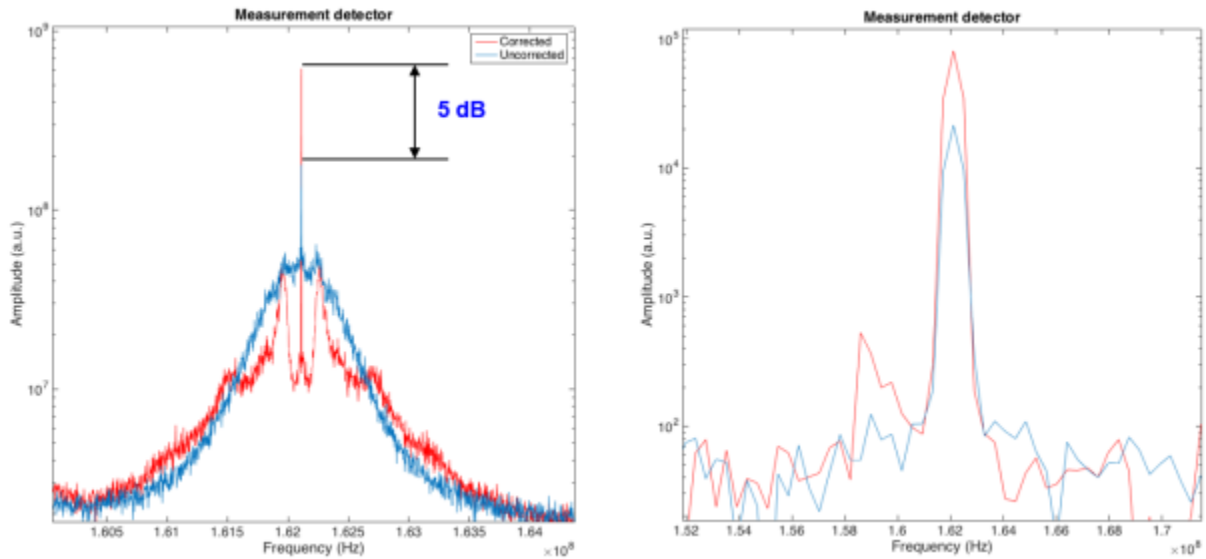


Figure 40. (Left) Multi-heterodyne signal of the peak before digital time-domain correction (blue) and after digital time-domain correction (red). (Right) both signals after coherent averaging in the time-domain.

Figure 41 shows the full spectrum with coherent averaging after having corrected the time domain signal for both F_{rep} and F_{ceo} drifts. The gain in dynamic range of coherent averaging is significant. However, the most important figure for any sensing system is not the dynamic range of the comb modes, but rather the amplitude stability of the individual peaks. To account

for the amplitude stability of the coherently averaged mode locked peaks, we developed a new Allan deviation computational method (Figure 42) which works on coherently averaged data.

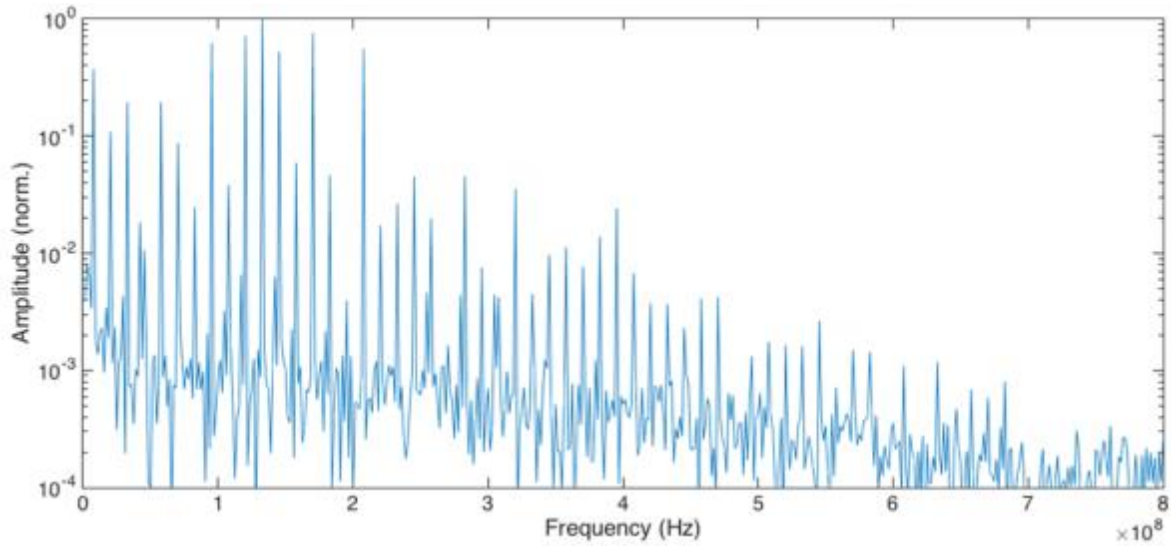


Figure 41. Full multi-heterodyne signal spectrum with coherent averaging after correcting the time-domain signal for both F_{rep} and F_{ceo} drifts.

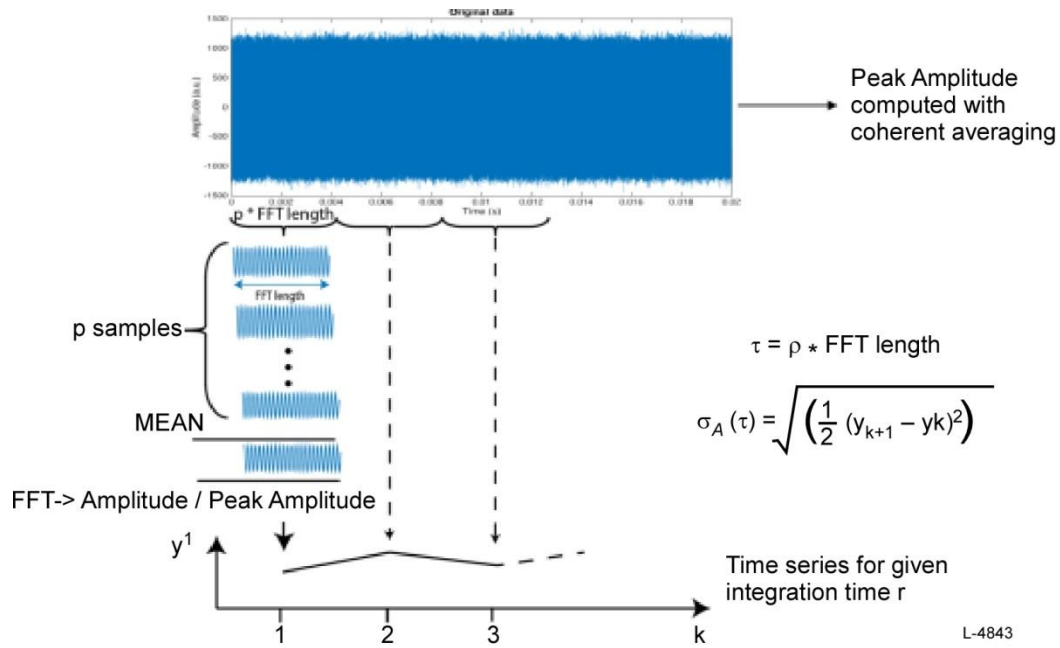


Figure 42. Allan deviation algorithm.

The computation of the traditional Allan deviation is not compatible with the coherent averaging, which averages the signal in the time domain and only computes the average at the end. The new algorithm we developed, averages coherently n number of slices of a total integration time of τ , computes the FFT, extracts the amplitude and compares the amplitude fluctuations of differently averaged signals of different integration times. Using this method, we get an Allan deviation of 10^{-2} at around 1 ms integration time. This is not better, even slightly worse, compared to non-coherent averaging. As shown in Figure 43, with longer integration times, the SNR becomes better.

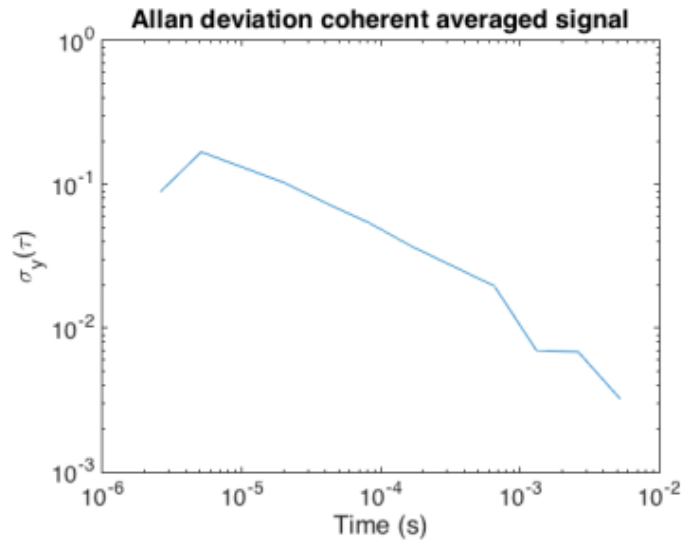


Figure 43. Allan deviation of coherently averaged signal.

We have concluded that the reason that we do not see an improvement of the SNR when conducting coherent averaging is twofold:

- a) The main source of amplitude noise originates from the laser itself and has nothing to do with the algorithm used.
- b) The worse SNR compared to non-coherent averaging is the non-ideal locking and correction algorithms. There is still a substantial amount of power outside of the coherently averaged signal (basically the power that is observable inside the side lobes after the correction), therefore the coherent averaging induces amplitude modulation whenever the signal is not locked and resided in the side bands.

Given that we do not expect to see any improvement of the SNR using coherent averaging, but that the correction algorithms to achieve coherent averaging are extremely slow and about a factor 1000x more computational expensive, we decided to implement an incoherent averaging algorithm with much less dead time and larger throughput.

Laser SNR evaluation

In order to measure the noise floor of a laser we use the setup shown in Figure 44 while sweeping the current of the laser to different comb regimes with special care to avoid feeding back into the laser. Increasing the current drives the laser first in the single mode regime, afterwards follows a clean comb regime with favorable SNR and a high phase noise regime, unfavorable for dual-comb measurements.

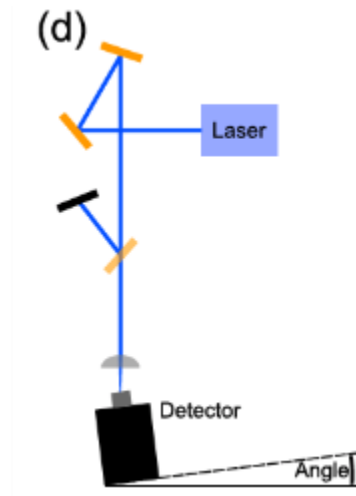


Figure 44. Setup for evaluating laser SNR.

Figure 45 shows a typical noise measurement result. The three noise regimes are clearly visible switching from single mode to comb regime to high-noise regime. The measurement frequencies stay within about 100 MHz.

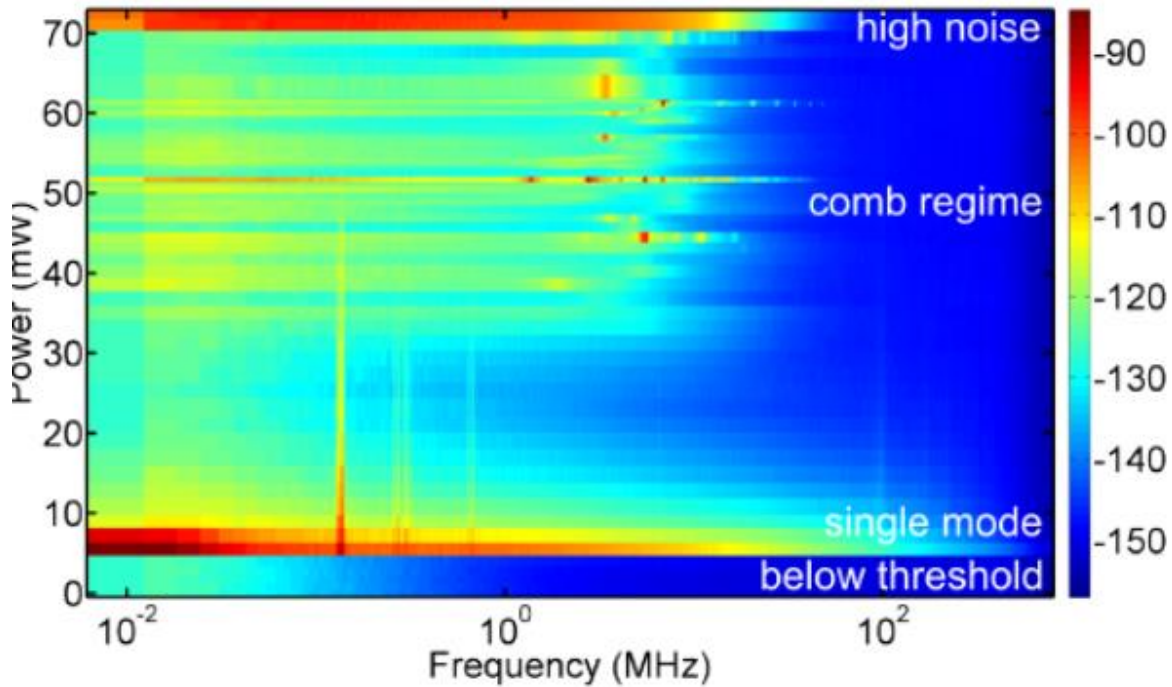


Figure 45. SNR plot.

3.2.3 Multi-heterodyne processing algorithm summary

In this section, we describe the final operation of the algorithm developed for the acquisition of high SNR data with dual-comb based QCL spectrometers.

The signal processor algorithm can be divided in these steps:

- a) Measure a multi-heterodyne signal in the time domain for 20 ms on two channels. One is the sample channel, the other one the reference channel.
The F_{rep} and F_{ceo} drift measurements are all done on the reference channel.
- b) Split the 20 ms acquisition in n-equally spaced time slices.
- c) Search for F_{rep} for this acquisition at the beginning of the 20 ms acquisition in the reference channel
- d) Search for F_{ceo} drift within the 20 ms acquisition
- e) Using the F_{rep} and F_{ceo} information, generate a grid of indexes on which the comb lines will reside.
- f) Use the grid to measure the amplitudes of the sample and reference channel and extract the transmission from this.

a) *Measurement*

Since the reference channel is not reduced by the scattering or interaction with the target, we use the reference channel to measure the grid and peak position of the signal channel even when the signal channel is extremely weak or even totally absent.

b) Splitting

The reference channel is subsequently split into n equally spaced time-slices. Each time slice is converted into the Fourier space using the FFT. The processor has N -spectra, each containing information on the F_{rep} and F_{ceo} drift. Figure 46 illustrates this process.

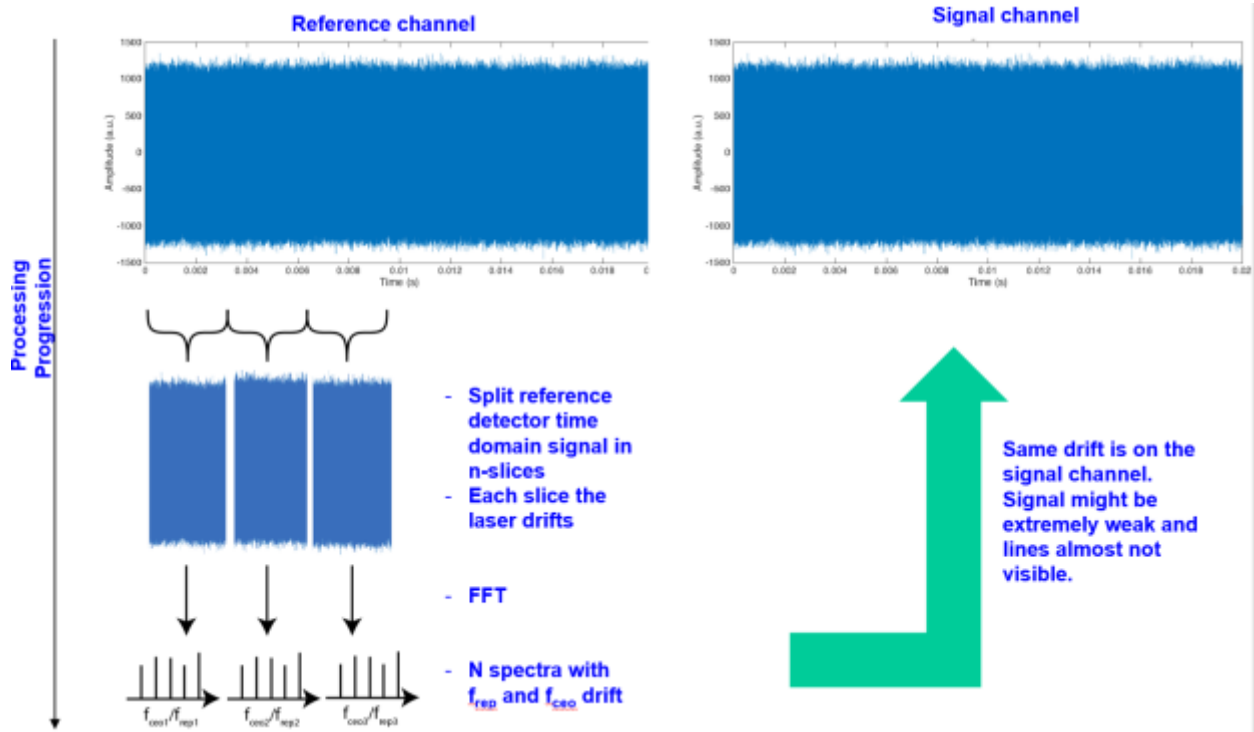


Figure 46. The reference channel is used for identifying the comb tooth locations and drift.

c) Search F_{rep}

Figure 47 shows how to calculate the F_{rep} of the first time slice. From the autocorrelation of the spectrum from time-slice 1, the N -th peak gives information on the NF_{rep} peak.

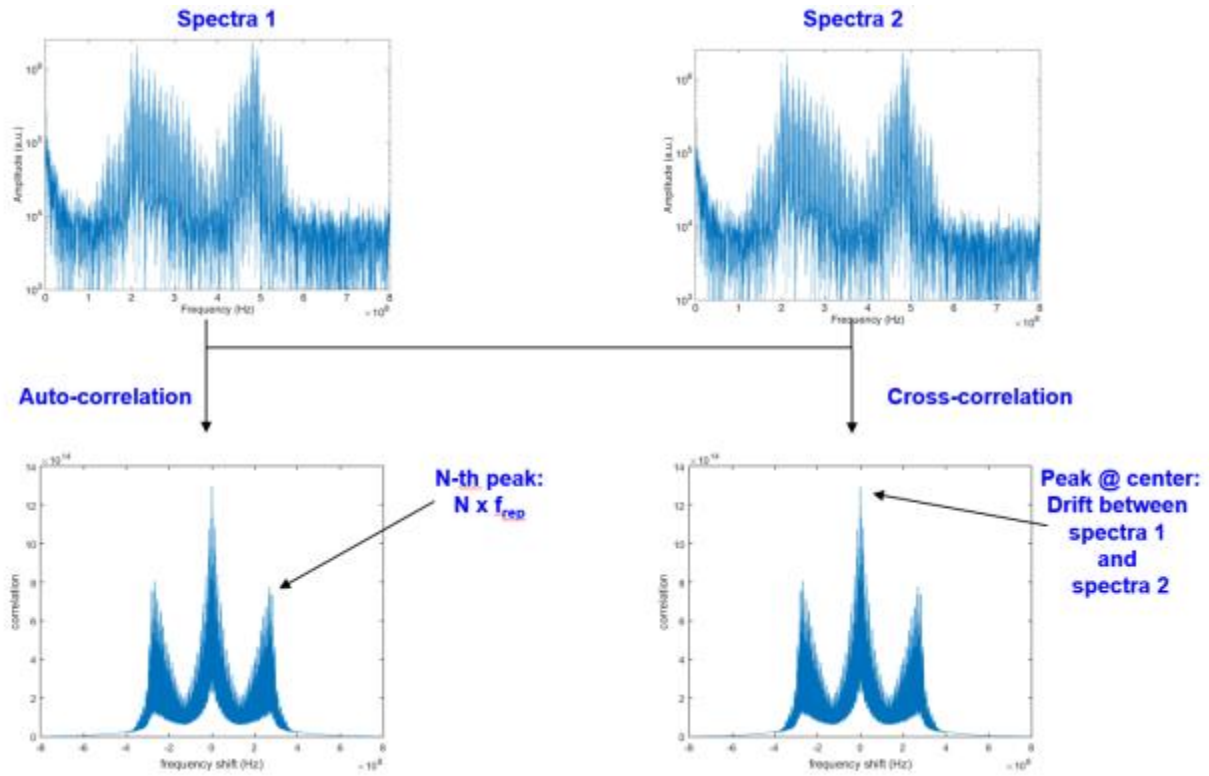


Figure 47. Autocorrelation is used to quantify drift of peaks.

d) Search the F_{ceo} drift

The drift between the individual n-time slices is computed similarly to the F_{rep} measurement. The correlation between spectra 1 and the N -th spectra is computed, and the resulting center peak gives the drift.

e) Generate grid of indexes for all slices

Using the drift information from the two previous steps, we next compute the array of frequencies. Figure 48 shows the result of the reliable grid finding algorithm using the F_{rep} and F_{ceo} drift information. In blue, the original multi-heterodyne signal is shown. In color, the individually picked peaks of the multi-heterodyne signal are shown. The grid matches exactly the heterodyne signal, including where there is minimal detectable power. As shown in Figure 49, the grid is subsequently filtered by a threshold above the noise level, typically set to 2-3x the noise level.

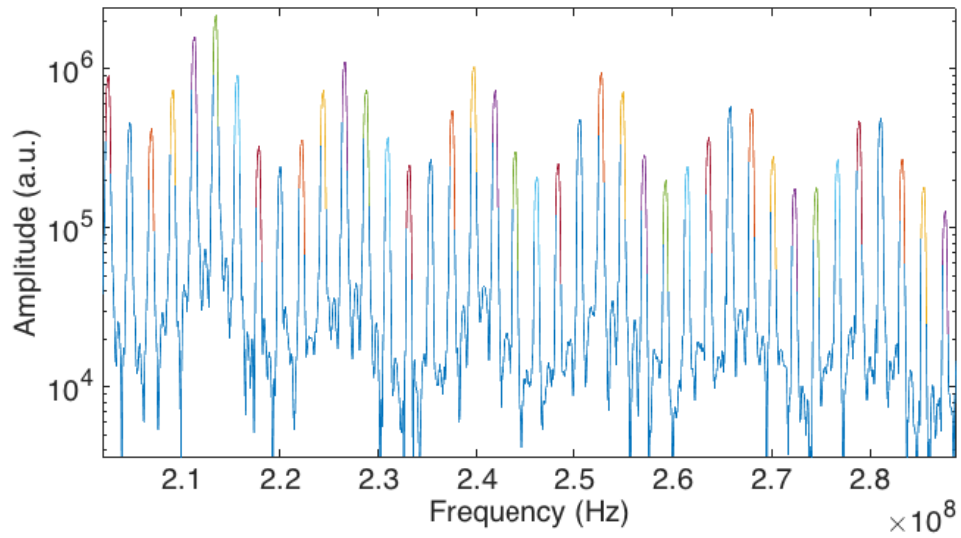


Figure 48. Output of grid finding algorithm reliably identifies peak locations.

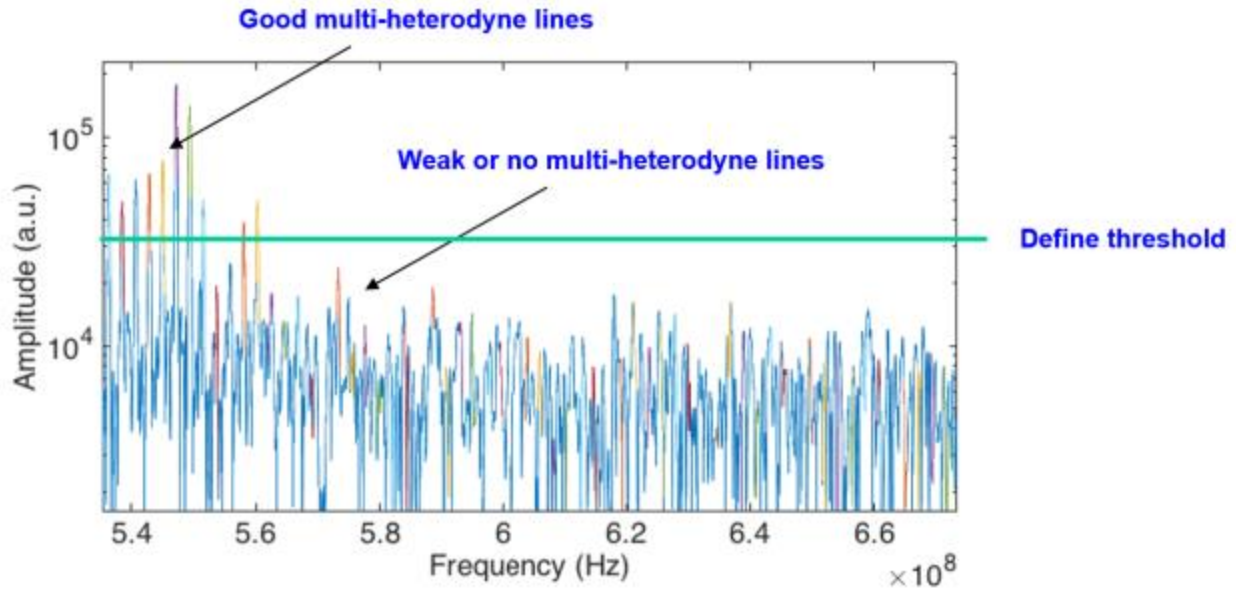


Figure 49. Amplitude threshold for peak processing.

f) Extract the amplitudes signal and reference amplitudes form grid

After computing the grid indexes on the reference channel, it becomes thus possible to compute the amplitude on the signal channel with the same grid. Since the signal and reference channel drift in a correlated fashion, the indexes from the reference channel are also valid on the signal channel, even if there is the signal amplitude is small.

Signal read-out algorithm

The fact that the acquisition is not synchronized with the laser signal, means that the acquisition phase is random. This is problematic for small signal amplitudes, since the $\text{abs}(\text{fft})$ is always positive. IRS has developed an algorithm to compute the correct signal amplitude even if the signal is below the noise. As the Figure 50 illustrates, the random noise fluctuations therefore result in an overestimated signal amplitudes. This leads to a distortion of the signal and is particularly problematic for small signal amplitudes (Figure 51).

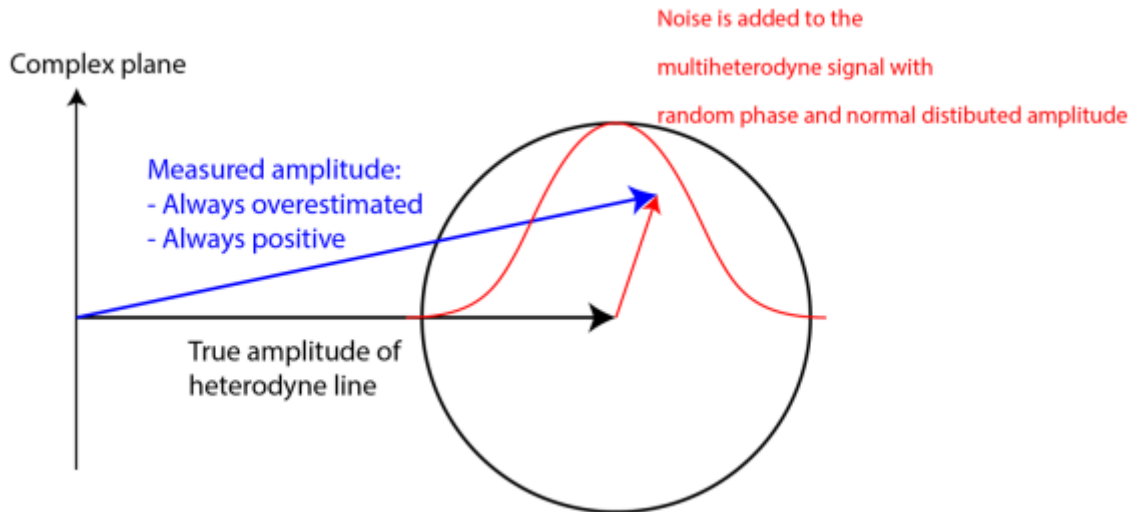


Figure 50. Representation of the true amplitude (black arrow) we wish to determine and the actual measured amplitude (blue arrow) resulting after random noise (black circle) is added.

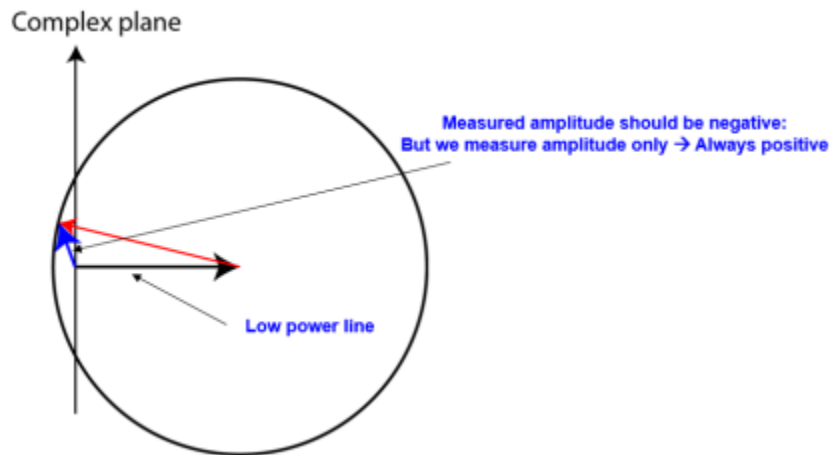


Figure 51. Representation of the true amplitude (black arrow) we wish to determine and the actual measured amplitude (blue arrow) resulting after random noise (black circle) is added for a small signal relative to noise amplitude.

If the noise distribution is larger than the signal size, the signal should be negative sometimes to average to the correct level. However, the absolute computation of the signal is always positive resulting in a systematic error on the signal amplitude computation. To overcome this problem we subtract in quadrature from the measured signal an exponentially average of the noise.

$$S_{calc} = \sqrt{S_{meas}^2 - \frac{N^2}{2} - \frac{N^2}{2} e^{1-1\left(\frac{S_{meas}}{N}\right)^2}} \quad (5)$$

where S_{meas} is the measured signal on either the signal or reference channel, N is the averaged noise floor measurement, and S_{calc} is the true signal amplitude.

Processor design

The overall processor design is illustrated in Figure 52. The processor was programmed in a modular fashion. All of the following parts of the program run independently and asynchronously, guaranteeing an efficient parallel execution and most efficient processing.

- A) IRspectrometerClient - GUI: The GUI gets processed data and logging information from the Processor over a TCPIP link and displays the results. This includes the multi-heterodyne signal as well as the transmission and absorption spectrum of the dual-comb system.
Furthermore, it is possible to send commands to the IRspectrometer Server via a simple command line.
- B) IRspectrometer Server: TCP Server: The TCP Server makes a connection between the GUI and opens two channels to send
 - a. Strings with: Log and Commands
 - b. Data Channel to send all processed measurements to the client
- C) IRspectrometer Server: Interpreter: The interpreter takes the commands from the GUI, interprets them and send the correct signals to the Processor, Driver, and IO InstrumentControl.
- D) IRspectrometer Server: IOInstrumentControl: This part is connected to a AI/AO channel for comb control. It sets and reads the current of the lasers. It sets and reads the temperature on the peltier and it has other digital I/O ports allowing to turn on/off the instrument by software.
The system data is sent in a periodic measurement to the client. The GUI subsequently updates the GUI to show the new measurements.
- E) IRspectrometer Server DiskWriter: A very powerful DiskWriter has been written. The disk writer gets raw binary int16 data from the processor and allows writing these binary files on the harddisk if requested. The data throughput is 20%.
- F) IRspectrometer Server Driver: The driver is responsible for the acquisition of the multi-heterodyne signal in the time domain. The Processor acquires two channels simultaneously at a sample rate of 1.6 GS/sec with 800 MHz bandwidth each channel. The acquired data is pushed on a FifoQueue which is filled successively with data.
- G) IRspectrometer Server Processor: The processor is connected to the same queue and pulls data from the FifoQueue. The processor then processes the data to:

- MultiHeterodyne Signal
- Transmission and absorption spectra according to the processor described beforehand.

Once the processor is finished, the requested data (e.g. multi-heterodyne signal/transmission) is sent to the client.

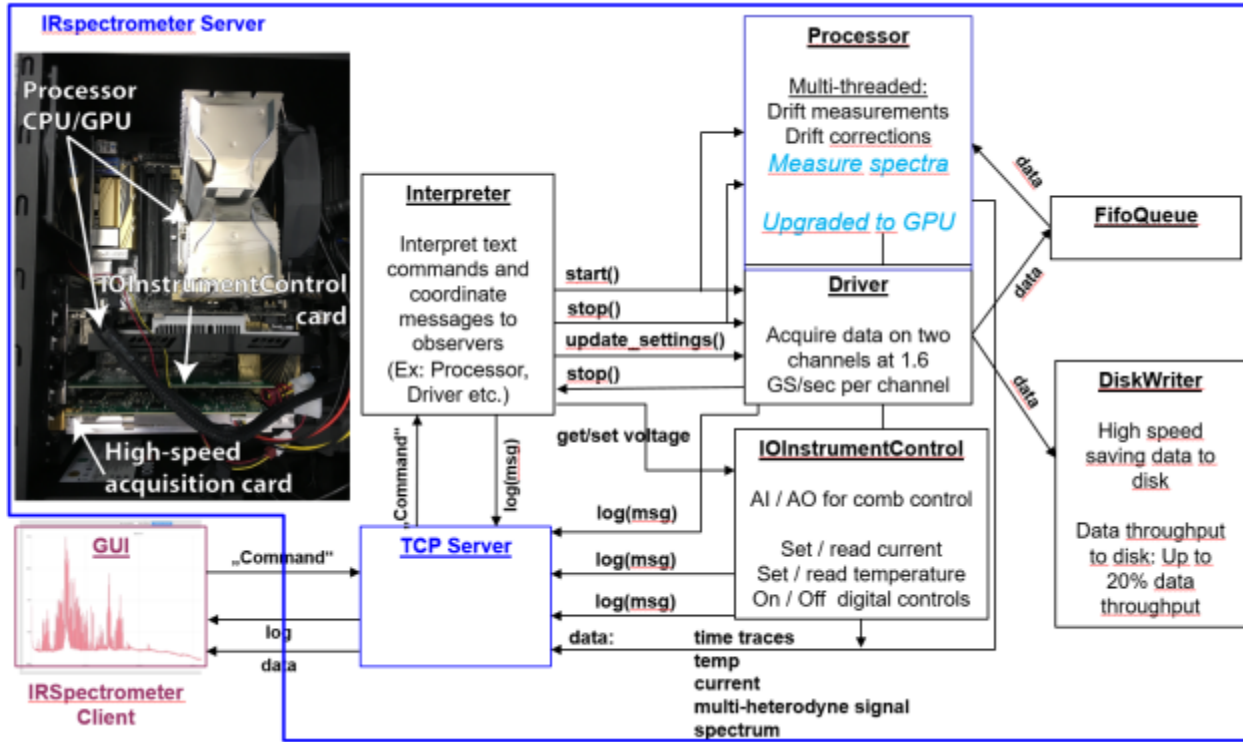


Figure 52. Processor design.

Performance testing of the precossor demonstrated:

- Data acquisition up to 1 GHz bandwidth / 12 bits.
- Increased robustness of algorithm
- Transfer of drift corrected measurments to the client
- Live display of the most important data

3.3 Sensor Design

3.3.1 System model

For the operational concept shown in Figure 53, we assume Lambertian scattering with $\sim 5\%$ diffuse reflectivity from the surface and consider a detector with collector diameter d imaging a region, A_{imag} , of a surface coated with target residue at a standoff distance D . The

power incident on the detector is $P_{\text{det}} \cong L_{\text{det}} A_{\text{imag}} \eta \left(\frac{d}{2D} \right)^2$ where η is the transmission efficiency of the collection optics and L_{det} is the incident radiance. To model the radiance incident on the detector we consider a contaminated surface schematically illustrated in Figure M1. For mass loading $\sim 1 \mu\text{g}/\text{cm}^2$, the target is optically thin and the resulting optical signature is dominated by target absorption, shown as L_{thin} . The L_{thick} term can be neglected. The total radiance from the surface due to radiation terms (blue arrows) is $L_{\text{surf}} \epsilon_{\text{surf}} T_{\text{film}} + L_{\text{film}} \epsilon_{\text{film}} (1 + R_{\text{surf}} T_{\text{film}})$ where $\epsilon = 1 - R$ is the emissivity of the surface and film and L is the temperature dependent Planck function. Since the film is thin, we can assume it is in thermal equilibrium with the surface, thus $L_{\text{film}} = L_{\text{surf}}$ and we can simplify to $L_{\text{surf}} (1 - R_{\text{surf}} T_{\text{film}}^2)$. The radiance from the optically thin reflected term (red arrow) is $(L_{\text{sky}} + L_{\text{las}}) R_{\text{surf}} T_{\text{film}}^2$, including contributions from both the ambient (L_{sky}) and the laser: $L_{\text{las}} = P_{\text{las}} A_{\text{las}}$. Note that if the laser spot is well matched to the imaging region at the surface, $A_{\text{las}} \sim A_{\text{imag}}$. The final resulting radiance at the detector is

$$(L_{\text{sky}} + L_{\text{las}} - L_{\text{surf}}) R_{\text{surf}} T_{\text{film}}^2 + L_{\text{surf}} \quad (1)$$

where the second term is the background and the first term is proportional to the film transmission, the surface reflectivity, and the radiance contrast between the laser and the surface. Of all these terms, only T_{film} has a strong wavelength dependence, so the target's spectral signature in the received power is $L_{\text{las}} R_{\text{surf}} (1 - T_{\text{film}}^2) \sim 2 L_{\text{las}} R_{\text{surf}} A_{\text{film}}$, where A_{film} is the single pass absorption through the film which depends on the absorption cross section σ and the mass loading ρ according to $A_{\text{film}} = 1 - \exp(-\sigma \rho t) \sim \sigma \rho t$, where t is the film thickness.

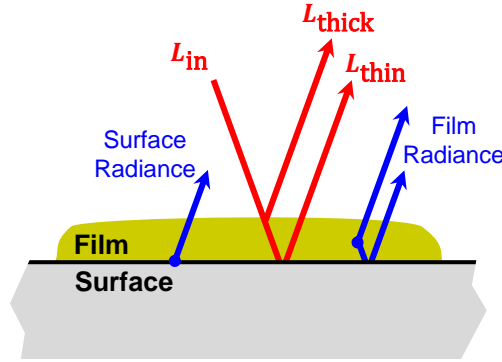


Figure 53. (blue) and reflective (red) pathways that provide the total radiance at the detector.

In terms of its specific detectivity, D^* , the noise equivalent power (NEP) of the detector of area A_{det} is $\text{NEP} = \sqrt{A_{\text{det}} / (2\pi\tau)} / D^*$, where τ is the total integration time for the measurement ~ 1 second. For a representative 0.2 mm diameter detector with a $D^* = 4 \times 10^8 \text{ cm}\sqrt{\text{Hz}}/\text{W}$, the NEP is $\sim 20 \text{ pW}$. As a function standoff distance, Figure 54 shows the signal to noise ratio (SNR) defined as the change in detector signal due to the target chemical divided by the detector NEP, assuming a 10 cm diameter receiver aperture. This figure also shows the effect of 0.05% laser intensity noise that remains after normalization with a reference channel.

To achieve reasonable SNR, this result shows that 50 mW OFC power is required to achieve the target system sensitivity at meter scale standoff distances.

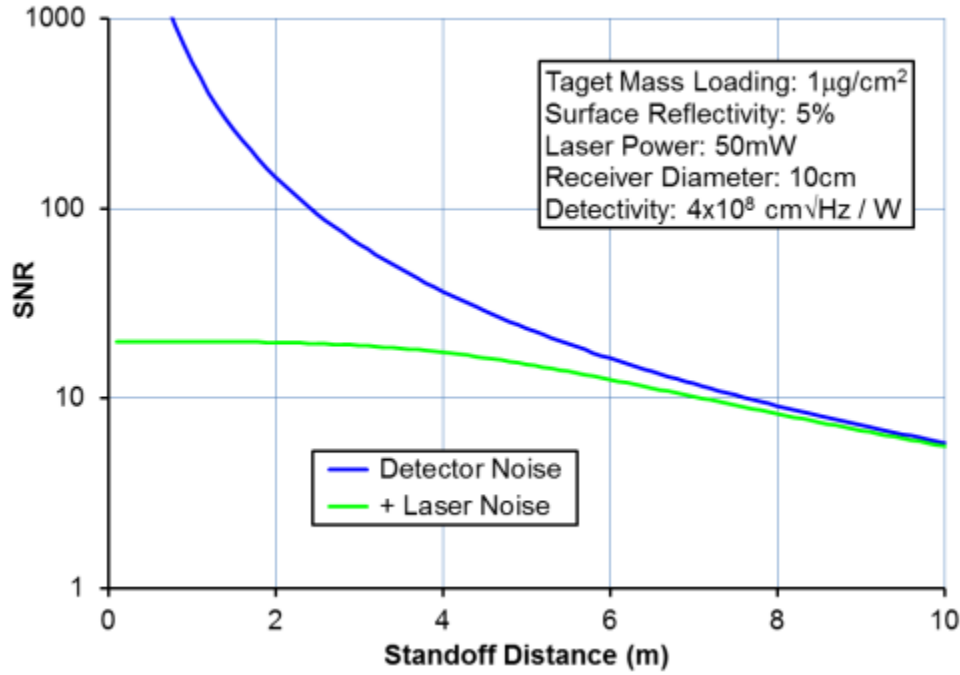


Figure 54. Signal to noise ratio (SNR) as a function of standoff distance to the target.

3.3.2 Speckle

Speckle occurs any time coherent light is scattered from a rough surface and observed by a finite aperture detector (Figure 55). Depending on the speckle contrast C , it can dominate the signal to noise ratio of a sensor system implementation. To quantify the contrast we consider, spatial / angular diversity, temporal diversity, and diversity from independent sources. For spatial / angular diversity we define

$$K = (FOV_{rx} / FOV_{tx})^2 \quad (6)$$

where FOV_{rx} and FOV_{tx} are the receiver and transmitter field of view or resolving power, and

$$M = A_{spot} / \sigma_x^2 \quad (7)$$

where A_{spot} is the illumination area on the target and σ_x^2 is the spatial coherence length of the roughness of that surface. Combine these terms we can write the contrast as

$$C = \sqrt{\frac{M+K-1}{MK}} \quad (8)$$

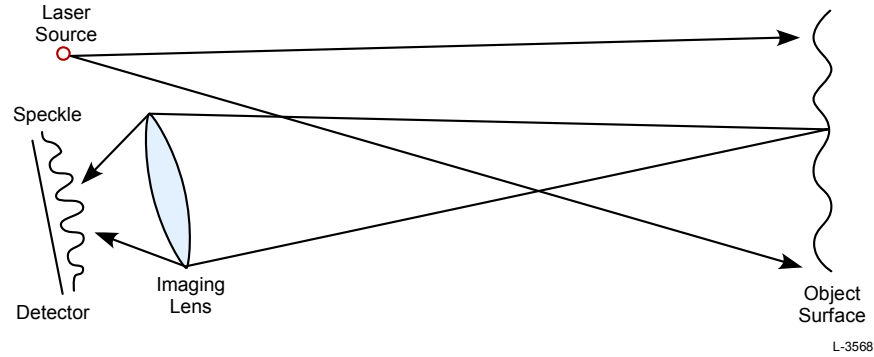


Figure 55. Key aspects of speckle.

Laser wavelength can also contribute to diversity that reduces speckle contrast but this requires that the laser linewidth $\Delta\lambda \gg \lambda^2/2\sigma_y$ where σ_y is the height variation of the surface and this condition is not met for LWIR lasers and typical surfaces.

If the laser source is made up of multiple independent sources with no mutual coherence, the contrast will be reduced according to $C \propto 1/\sqrt{N}$ where N is the number of independent sources. Since individual comb teeth are highly coherent, there is minimal contribution from this effect.

For our system parameters we estimate speckle at $C \sim 1\%$. Because the comb spacing $\Delta F_{\text{rep}} \ll F$, the speckle inducing optical phase difference from spatial point to point across the surface is unlikely to vary from comb tooth to comb tooth. Thus, all comb teeth will experience the same overall amplitude change due to speckle with minimal artifacts within the spectrum. However, the total optical power, the sum of all comb teeth will exhibit the same speckle effect as a single frequency laser would. This effect will inhibit our ability to use regions of the surface that do not contain the target compound (“background”) to help extract and isolate the target signature. However, at what level this $\sim 1\%$ contrast limits the overall system performance remains to be determined in the ongoing testing. Complicating this analysis is the effect of optical feedback where the varying optical intensity due to interfering speckle cells also creates varying feedback to the laser(s) which can cause more significant non-linear effects to the comb spectrum.

3.3.3 Detectors

In order to respond to the full bandwidth of the dual OFCs beating together generating a comb in the radiofrequency (RF), the detector must have bandwidth ~ 1 GHz. In terms of D^* , the best performing commercially available detectors are based on the mercury cadmium telluride (MCT) material system. The detectors available from *Vigo* (Figure 56), such as PVI-4TE-10.6, are electrically cooled with 4-stage thermo-electric cooling achieve a $D^* \sim 5 \times 10^9 \text{ cm}\sqrt{\text{Hz/W}}$. Because both the bandwidth and D^* decrease slightly as the active area increases, the smallest active area ($\sim 50\mu\text{m}$) is the best. Achieving this performance level, however, requires optimally filling the detector active area. For the reference detector where the input beam is spatially well controlled, the spot size can be reliably made this small. For the signal detector, on the other

hand, where the diffusely scattered light is collected by a large primary optic, the spot size on the detector is limited by spatial aberrations from the collection system. To compensate, we use the same detector size but with the hemi-spherical immersion lens integrated by the detector vendor directly on the active area.



Figure 56. Vigo MCT detector.

3.3.4 Optical Isolation

The application of stand-off detection from a diffuse surface almost guarantees that some fraction of the light from the source will be retroreflected to follow the beampath back to the source. The rough surface produces both a specular and diffuse reflection where there is always some fraction of the rough surface which is normal to the incident beam. With such perfect alignment, even small optical powers can influence sensitive optical elements. In the case of QCL OFCs, this presents a challenge since the behavior of the combs is sensitive to optical feedback. In the presence of feedback, the beatnote of the QCL combs is observed to jump frequencies and exhibit bistable behavior as well as broaden the comb lines.

If optical elements in the beampath are oriented normal to the beam, the residual 1% reflections from the antireflection coatings are enough to disrupt the spectral characteristics of the combs. As a matter of procedure, these optics are all angled slightly with respect to the normal such that the returning light does not overlap with the source. However, the diffuse scattering of the target surface requires additional optical isolation.

The highest extinction approach to optical feedback reduce back-reflections is with an optical isolator, a non-reciprocal device for light allowing light to travel one way, but not the other. In an optical isolator, two polarizers oriented a 45° are placed on either side of a transmissive crystal in which the plane of polarization rotates via Faraday rotation in the presence of a magnetic field B . The amount of Faraday rotation is quantified with a Verdet constant V where the rotation θ is determined by the product VBl where l is the pathlength through the material. Since V has a wavelength dependence, an isolator for a particular wavelength is created by selecting the appropriate B and l for the given V of the crystal such that light experiences a 45° rotation to transmit through the polarizers, but counter-propagating light is rejected by the polarizers.

Optical isolators based on materials such as Yttrium Iron Garnet (YIG), Bismuth Iron Garnet (BIG), and Terbium Gallium Garnet (TGG) combined with calcite polarizers can be used to provide optical isolation throughout the visible and near-infrared, but materials for Faraday rotation as well as high extinction polarizers in the Mid-IR and LW-IR are significantly harder to find. To our knowledge, two companies commercially produce optical isolators in this wavelength range. (1) *Laser 2000* (United Kingdom based) makes a line of mid-IR optical isolators from 4 μm – 14 μm which depend on highly specialized materials for both the rotator and the polarizers. (2) *Innovation Photonics* (USA based) advertises isolators operating at wavelengths of 4-5 μm as well as 8 μm with $\leq 90\%$ transmission with ≤ 30 dB of isolation.

Due to the inadequacies of currently commercially available LWIR isolators, we decided that optical isolation was not the correct approach. Instead, an approach using mid-IR quarter waveplates and wire grid polarizers was pursued. Figure 57 shows the wavelength dependence of the retardance of a quarter-waveplate designed for 7.5 μm made out of CdGa_2S_4 (Cadmium Thiogallate). This retardance shift is tolerable for the $\sim 100\text{cm}^{-1}$ wide QCL combs. These waveplates are manufactured with AR coatings by *Crystran* and distributed by vendors such as *LaserAnd Inc.* and *Edmund Optics*.

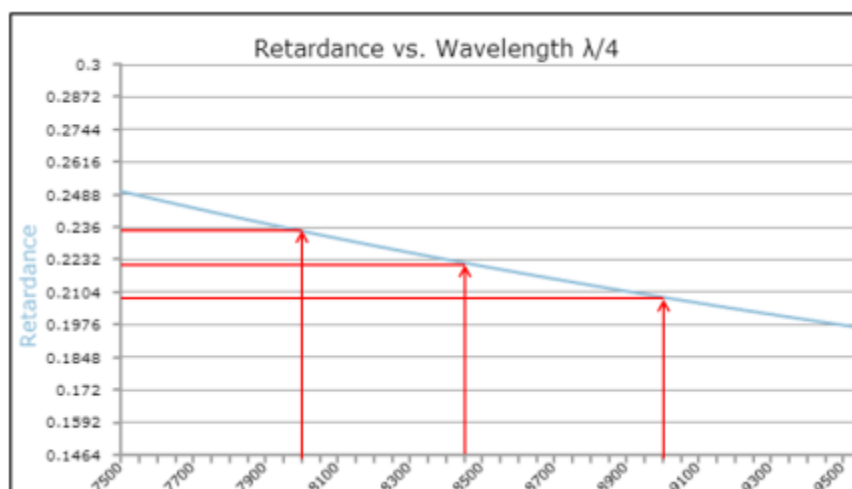


Figure 57. Dispersion of cadmium thiogallate $\lambda/4$ waveplate designed for $\lambda = 7.5 \mu\text{m}$ with arrows marking commercially available wavelengths.

4.0 RESULTS AND DISCUSSION

Measurements conditions are summarized in Table 1. We tried both fixed, switched, and spinning samples. As shown in Figure 58, switched samples were mounted to a Brandstrom Instruments A1263-2 shutter blade that actuates between two positions 90 degrees apart about the shutter motor's rotation axis, so that the shutter moves first one then the other sample centered onto the beam. We evaluated both manual switching, where the shutter blade was rotated manually approximately halfway through the data acquisition sequence, and electronic switching, where a function generator actuated the shutter and gated the dual comb acquisition system every 2 seconds. In both cases when the spectra from the blank coupon was used to normalize the spectrum from the sample coupon, the fixed oscillations in the processed comb spectra were reduced but the absolute reflectance level and the baseline shape were not properly normalized. These observations were highly repeatable from data file to data file but not when different blank coupons were used or even if the same blank coupon was moved slightly relative to the laser spot. Based on these observations, we conclude that the shutter motion is repeatable but the total amount of reflected light varies from coupon to coupon and as a function of position across a single coupon.

Table 1. Measurement Summary

Date	StandOff Distance	OD in Signal Path	Beam Diameter	Number of Data Files	Samples	Comment
7/24	0.285m	0.3	6mm	40	FSO in place	Manual switching
7/25	0.285m	0.3	6mm	40	SA11,SA12	Electronic switching
7/26	0.285m	0.3	3mm	50,10	SA11 - SA14	Fixed, spinning
7/26	0.894m	0.3	3mm	50,10	SA11 - SA17	Fixed, spinning
7/27	0.894m	1.0	3mm	40	SA11-17, B1-3, IG	Fixed, spinning
7/27	0.894m	0.3	3mm	40	SA11-17, B1-3, IG	Fixed, spinning
7/28	0.95m	0.0	3mm	40	SA11-17, B1-4, IG	(series C) Fixed
7/28	0.873m	0.0	3mm	40	FSO in place (SA21)	(series D) Fixed
7/28	0.95m	0.3	3mm	40	SA11-17,21 B1-4, IG	(series E) Fixed
7/28	0.95m	0.3	3mm	40	FSO in place (SA22)	(series E) Fixed
7/28	0.31m	1.0	3mm	40	SA11-17,21-2 B1-4, IG	(series F) Fixed
7/28	0.31m	1.0	3mm	40	FSO in place (SA23)	(series F) Fixed
7/28	0.31m	1.0	3mm	40	Krytox™ in place (SA23)	(series G) Fixed

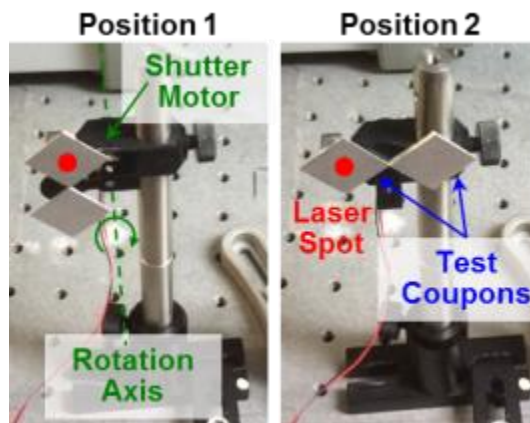


Figure 58. Electronic switching between two test coupons, one with target compound applied and one blank.

In an attempt to average out the effect of the irregular surface, we also mounted the sample to a chopper wheel motor as shown in Figure 59. Related to the observation discussed above, instead of averaging out the effect of different speckle cells, it introduced enough instability in the lasers to lower the comb signal to noise level below a usable level. Because this laser configuration had no optical isolation beyond simple OD filters, we suspect that some fraction of the the diffesulely scattered light incident on the target was feeding back to the laser. Figure 60 shows the overall setup with, in this case, a 0.3 meter standoff distance. With no focusing lens the laser spot was approximately 6mm in diameter at the target. With our collection optics, this spot size overfills the detector, so we also took data with a 100cm lens in the beam path reducing the laser spot size at the target to ~ 3mm diameter.

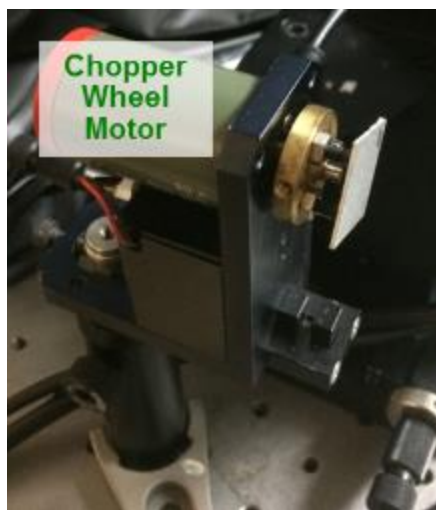


Figure 59. Sample mounted on chopper wheel motor for measurements with continuously moving sample.

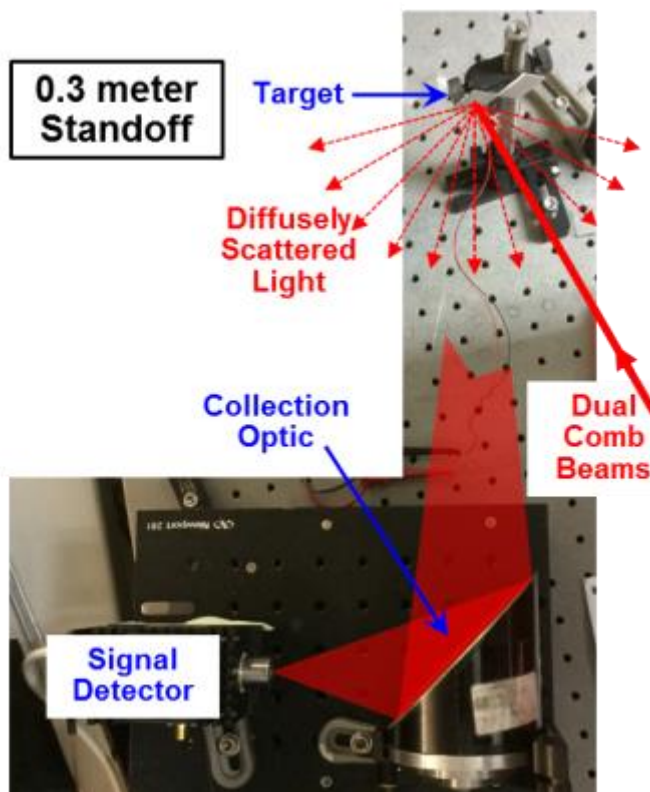


Figure 60. Optical layout for standoff measurements off of a diffusely scattering sample. This example shows a 0.3m standoff case.

Figures 61 through 64 show the data at various points in the processing, starting with a $100\mu\text{s}$ segment of the the 21ms long raw time domain signal from the two detectors (Figure 61). Figure 62 shows these data in the frequency domain after bin averaging over 1024 points. The inset shows a segment of the frequency domain data before bin averaging. As shown in Figure 63 the processing algorithm is applied to the frequency domain data to determine the amplitude of each comb tooth (shown in solid circles). This comb envelope is plotted again in Figure 64 for the entire spectrum along with a 12 point running average. The 1.973 cm^{-1} period oscillations that are clearly visible are present in every comb signal to reference ratio. They are highly repeatable in both spectral position and amplitude over repeated measurements of the same sample and after switching sample positions or samples, so they are attributed to a fixed etalon that differs between the signal and reference detector path. For absolute comb spacing of 0.328 cm^{-1} , this oscillation period is equivalent to 6.016 points. Therefore, as expected, bin averaging when the bin size is an integer multiple of 6 points reduces the oscillation amplitude by $\sim 99\%$ to a level below other sources of noise. This 12 point running averaging that achieves an equivalent resolution of 4 cm^{-1} is used in all of the subsequent spectral analyses.

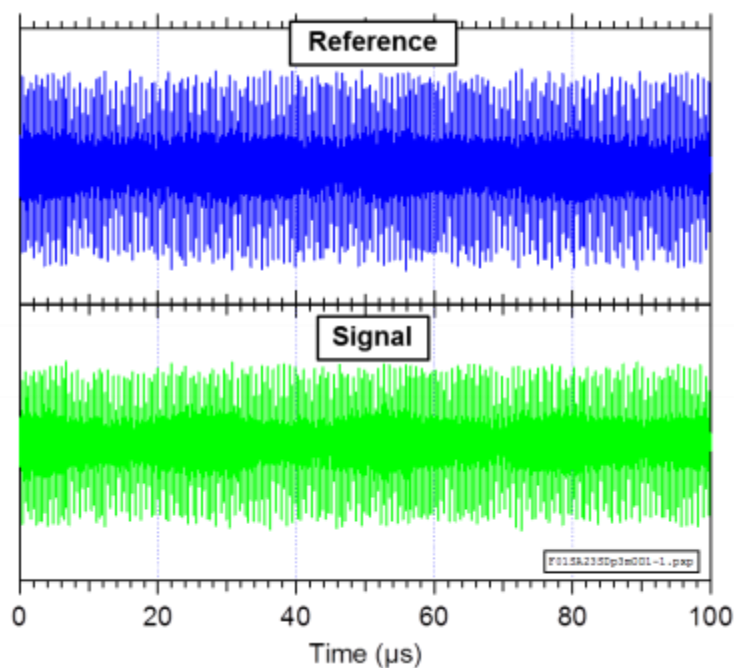


Figure 61. Segment of raw time domain comb data from the reference detector (top) and signal detector (bottom).

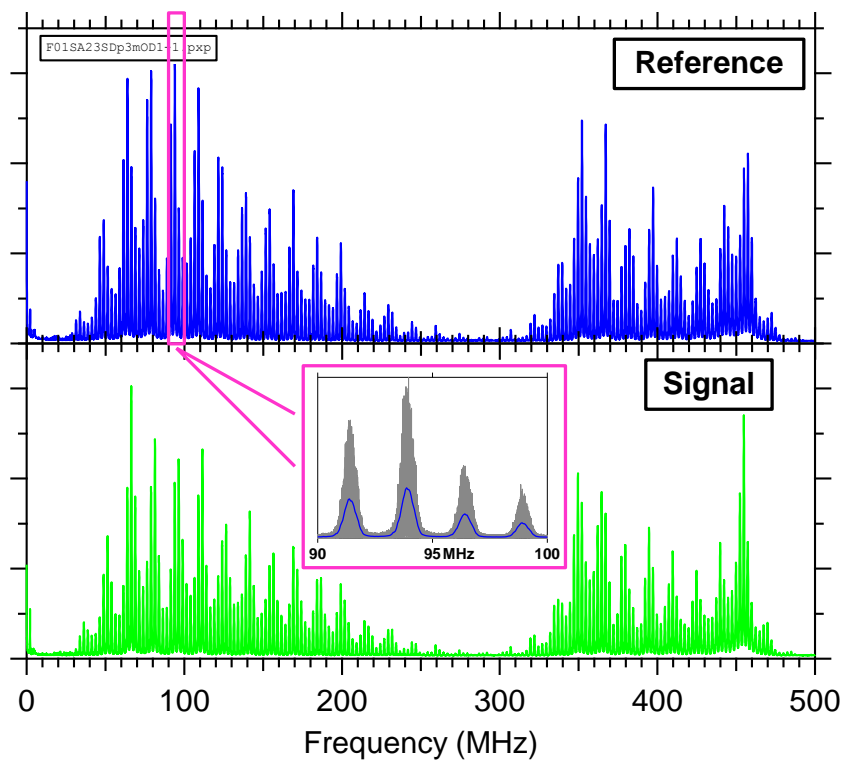


Figure 62. Raw frequency domain comb data from the reference detector (top) and signal detector (bottom) after bin averaging every 1024 points. Inset plot shows small region of frequency domain before bin averaging (gray).

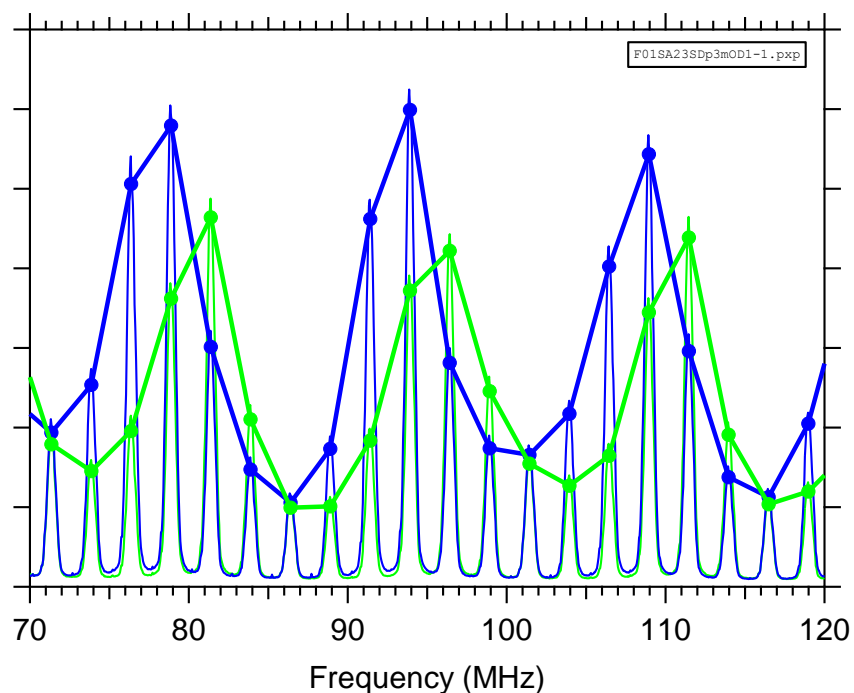


Figure 63. Segment of frequency domain comb data from the reference detector (blue) and signal detector (green) along with processed results (bold) determining amplitude for each comb tooth.

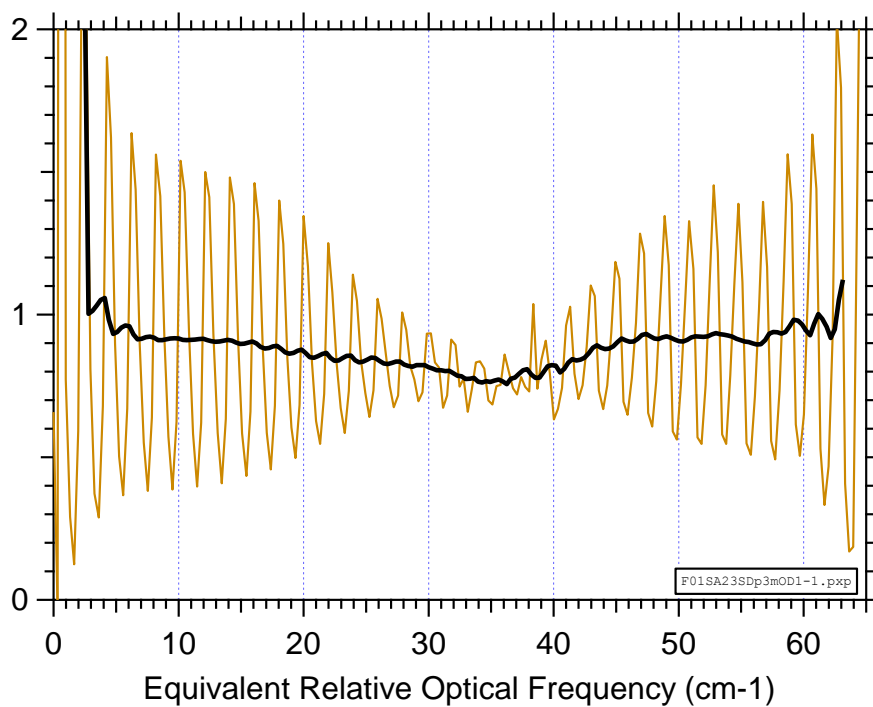


Figure 64. Ratio of signal to reference comb envelope from previous figure (brown) shown for the full spectrum converted to optical frequency, along with a 12 point running average (black) equivalent to a 4 cm^{-1} resolution.

In order to determine the absolute optical frequency of the multi-heterodyne comb spectral, the lasers “26HM” and “26BG” are individually characterized in a Fourier Transform InfraRed (FTIR) spectrometer. Figures 65 and 66 show FTIR spectra of individual lasers for a range of drive currents at the temperature closest to the following operating conditions used during the testing. For the drive current closest to the operation conditions a range of temperatures is also plotted.

	Laser 1 (26HM)	Laser 2 (26BG)
Current	0.9A	1.2A
Temperature	+26.2°C	+45.8°C

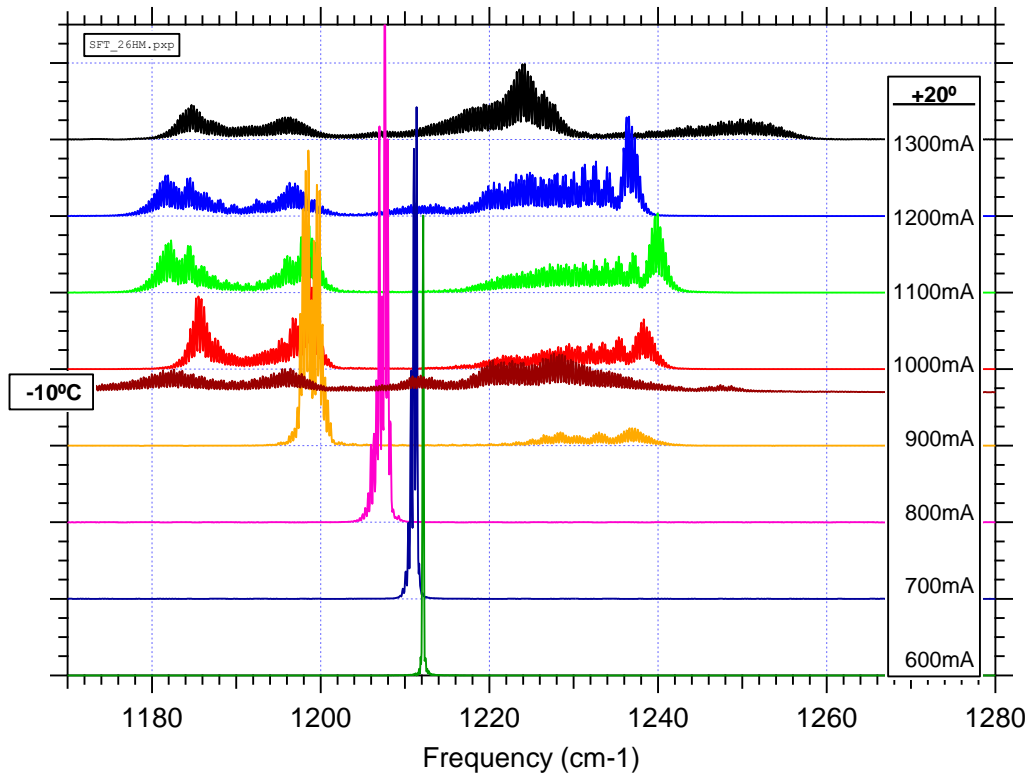


Figure 65. Optical Spectra from Laser 26HM.

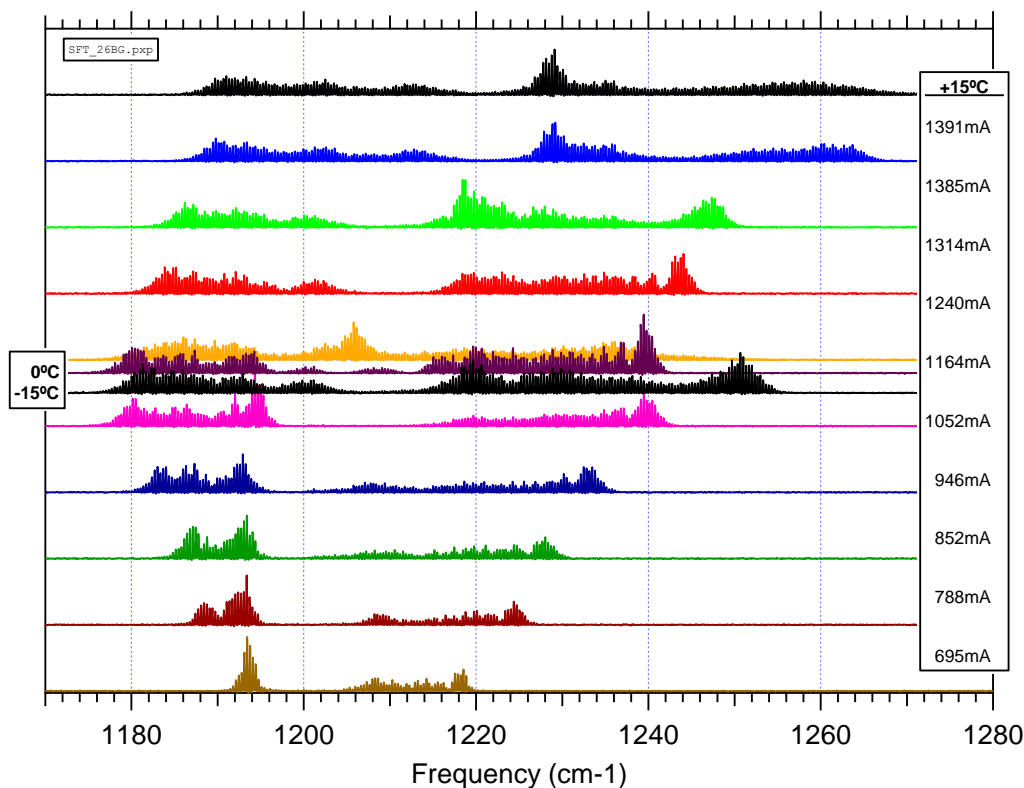


Figure 66. Optical Spectra from Laser 26BG.

The amplitude of each comb tooth from the spectra closest to the operation conditions (1.0A and +20°C for 26HM and 1.164A and +15°C for 26BG) was determined by fitting it to a Gaussian and plotted in Figure 67. The spectrum for 26BG has been scaled by a factor of 280 so that integrated area (total power) was the same for both devices. The geometric mean ($= \sqrt{L1 L2}$) is also shown and in the Figure 68 with logarithmic scale.

On the $\sim 10\text{cm}^{-1}$ scale temperature doesn't seem to have a significant effect on the laser's output spectrum, so these data imply that the hole (minimum amplitude) in the center of the RF comb spectrum should occur at $\sim 1211\text{ cm}^{-1}$. The measured comb space is 0.328 cm^{-1} .

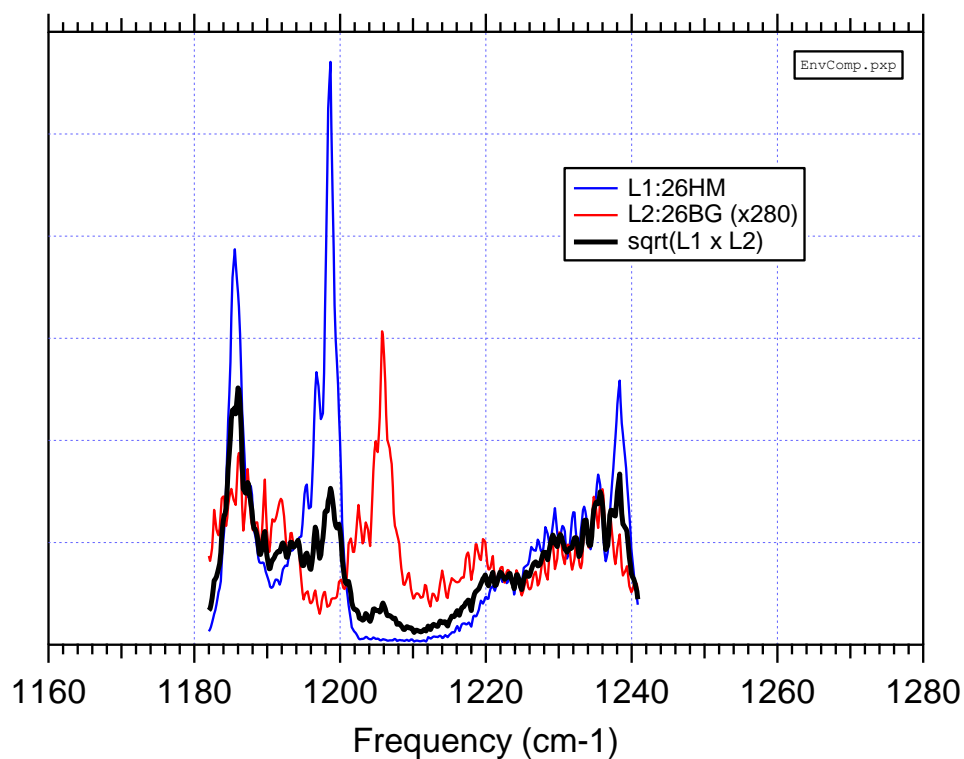


Figure 67. Envelope of optical spectra from laser 26HM (blue) and laser 26BG (red) along with their geometric mean (black).

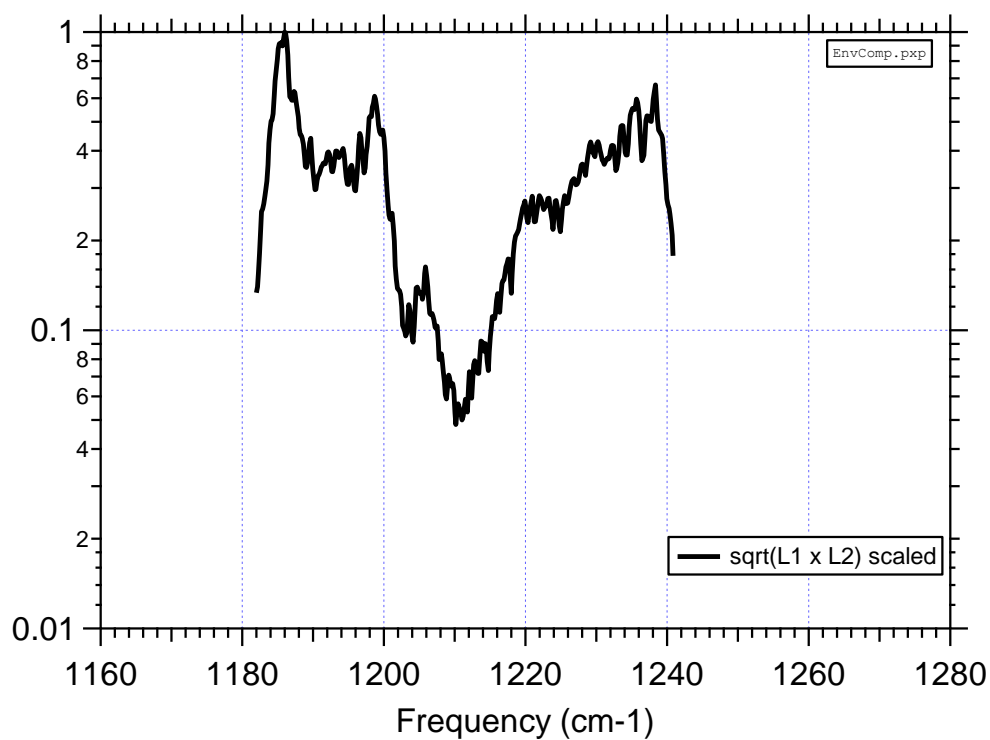


Figure 68. Logarithmic scale plot of combined (geometric mean) laser spectra.

Targets

In order to simulate the signatures of security related target compounds, we identified the following representative simulants:

1. fluorinated silicone oil (FSO), poly(methyl-3,3,3-trifluoropropylsiloxane) – *Alfa Aesar*
2. Krytox™ vacuum oil, grade 1514 – *Sigma Aldrich*
3. Dimethicone (SF-96), polydimethylsiloxane – *ClearCo*
4. UCON OSP-150 lubricant, 1H601606 – *Dow Chemical*

All of these compounds are clear (in the visible) oily liquids at room temperature with 40°C viscosity $\sim 150 \text{ mm}^2/\text{s}$. Because they are fluorinated, the traditional hydrocarbon absorption band around $3.4 \mu\text{m}$ is shifted to the LWIR, with strong absorption features around the target spectral regions. Figure 69 and 70 show their LWIR spectrum, where Figure 70 zooms in around the where the QCL combs emit.

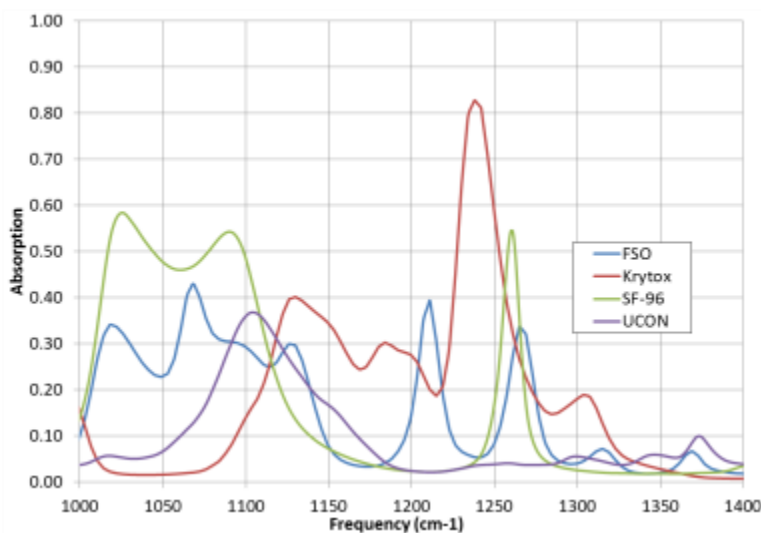


Figure 69. Previously measured LWIR absorption spectra for 4 representative simulants: fluorinated silicone oil (FSO), Krytox™ vacuum oil, Dimethicone (SF-96), UCON OSP-150 lubricant.

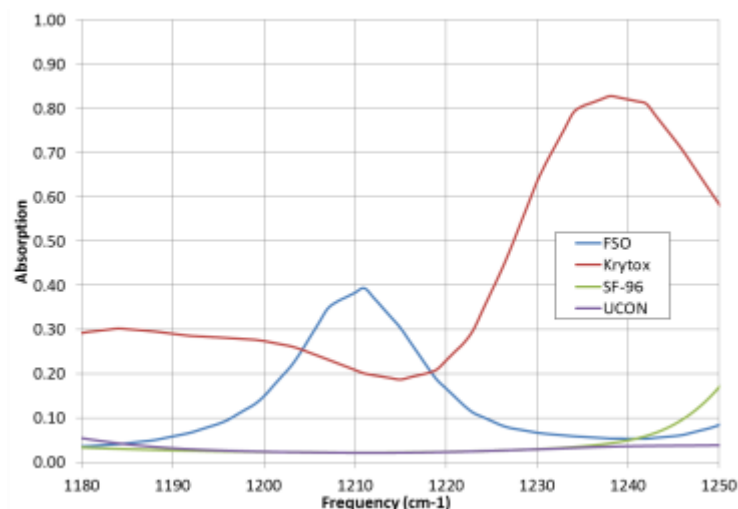


Figure 70. LWIR absorption spectra for 4 representative simulants in the region of the QCL comb emission.

Stand-off measurements were conducted with FSO and Krytox™, so quantitative measurements of these targets were taken using an Nicolet 4700 FTIR and a spectrophotometer cell. This FTIR spectrometer is capable of measuring transmission as a function of wavelength from 400 cm^{-1} to 4000 cm^{-1} through commercial liquid spectrophotometer cells from International Crystal Labs (Figure 71).



Figure 71. Liquid spectrophotometer cell.

This cell has NaCl windows and a calibrated $16.7\text{ }\mu\text{m}$ pathlength over a $\sim 1\text{ cm}$ diameter area. In order to improve measurement precision, a series of diluted solutions containing FSO are prepared such that measurements of several known concentrations in the optically thin regime can be compared. Hexane is an ideal choice for these measurements since it dissolves oils, has no strong optical absorption features in the $1100\text{ cm}^{-1} - 1300\text{ cm}^{-1}$ region of interest, and contains little water that can dissolve the NaCl windows. The following solutions shown in Table 2 were prepared:

Table 2. FSO Samples

Solution	Solute	Solvent	FSO Concentration (mg/cm ³)	Mass Loading (μg/cm ²)
A	100.0 μL FSO	10.0 mL Hexane	12.4	20.7
D	1.0 mL A	10.0 mL Hexane	6.20	10.4
B	2.0 mL A	4.0 mL Hexane	4.13	6.9
C	1.0 mL A	10.0 mL Hexane	1.13	1.9

Each of the liquid samples were vortexed for 20 seconds and pumped into the sample using a syringe. Prior to measurements, the sample holder is flushed with 8 mL of hexane to remove organic contamination. For each sample, 1 mL of solution is pumped through the holder to completely displace the previous sample. The samples are loaded in order of increasing FSO concentration to further avoid contamination with the previous sample which is a standard analytical technique.

Fractional transmission is determined by computing the ratio of the transmission of the solution containing FSO to a sample containing hexane. Due to variations across the FTIR full spectrum, the vertical offset of each transmission curves varies slightly. To remove this baseline, a point close to the region of interest at 1176 cm⁻¹ but sufficiently removed from absorption features is used. The fractional transmission of each of the samples is shown in Figure 72.

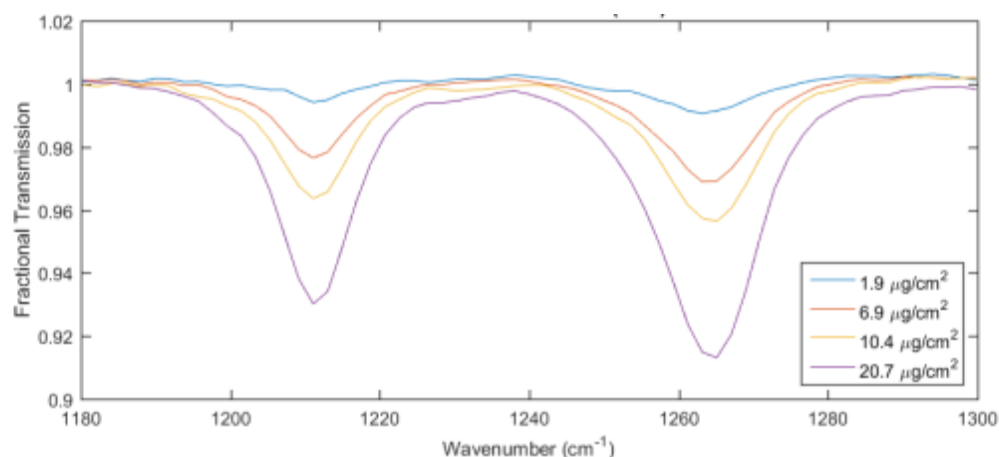


Figure 72. Fractional transmission from FTIR transmission spectra of FSO samples in Table 2 at a resolution of 4 cm⁻¹.

The fractional absorption light is described by Beer's Law

$$I = I_0 e^{-n\sigma l} \quad (9)$$

where I/I_0 is the fractional intensity, n is the density of FSO, σ is the cross section and l is the path of the interaction. The product nl is considered the mass loading in Table 2. The cross

section as a function of wavenumber is well-described by a Gaussian. Fits to the logarithm of the fractional intensity produce values for the peak absorbance and Gaussian width for both peaks at $1211 \pm 0.2 \text{ cm}^{-1}$ and $1264 \pm 0.2 \text{ cm}^{-1}$. The fitted peak values and computed mass loading of each solution determine the plot in Figure 73 where the slope determines σ for each of the peaks.

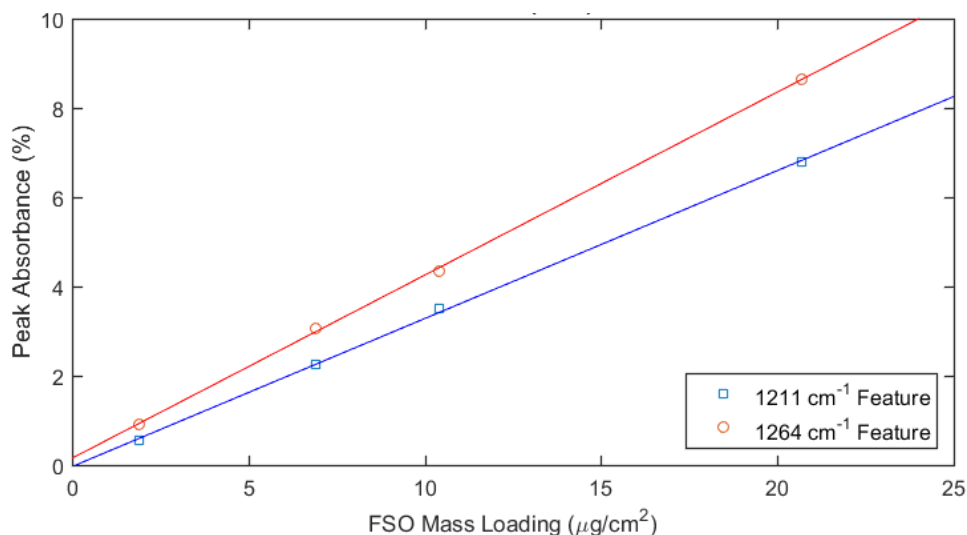


Figure 73. FSO Transmission as function of mass loading to determine absorption cross section.

The slopes and intercepts for the peaks are listed in Table 3. Deviation of the intercept with the expected zero value is an indication of possible systematic effects in the measurement. The intercept for the 1211 cm^{-1} peak is within one standard deviation while the intercept for the 1264 cm^{-1} peak is two standard deviations.

Table 3. Linear Fit Coefficients from Previous Figure

Peak	Slope (% Absorbance/ $\mu\text{g}/\text{cm}^2$)	Intercept (% Absorbance)
1211 cm^{-1}	0.332 ± 0.006	-0.03 ± 0.07
1264 cm^{-1}	0.410 ± 0.006	0.15 ± 0.07

In order to quantify the absorption of KrytoxTM, a similar series of measurements was performed. However, KrytoxTM is not soluble in common organic solvents, acids, or bases. KrytoxTM oils are completely miscible in highly fluorinated solvents such as trichlorotrifluoroethane (Freon 113), hexafluorobenzene, perfluorooctane, perfluorohexane, or perfluorodimethylcyclobutane isomers. However, many of these solvents have the same C-F bonds as KrytoxTM that absorb strongly around 1250 cm^{-1} . Hexafluorobenzene was chosen because its ring structure shifts the strong absorption to 1000 cm^{-1} and 1500 cm^{-1} (Figure 74) which makes it an ideal solvent to determine KrytoxTM absorption at $\sim 1250 \text{ cm}^{-1}$.

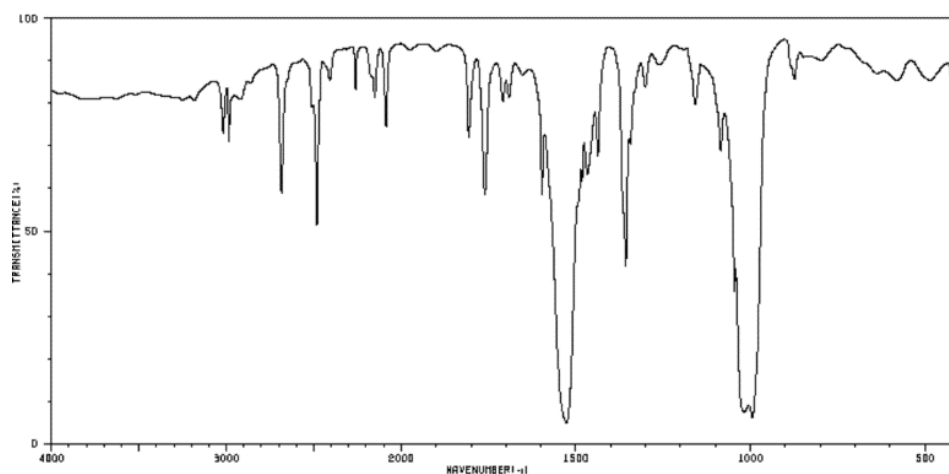


Figure 74. IR transmission spectra for hexafluorobenzene from SDBS database.

Four solutions hexafluorobenzene solutions containing ~0.1%-1% Krytox™ 1514 were produced (Table 4). They were vortexed for 15 s and pumped into the sample holder using a syringe. Transmission spectra of each solution was measured in order of increasing concentration and 1.5-2 mL of each solution was used to displace the previous sample.

Table 4. Krytox™ Samples

Solution	Solute	Solvent	FSO Concentration (mg/cm ³)	Mass Loading (μg/cm ²)
A	100.0 μL Krytox™	10.0 mL C ₆ F ₆	18.7	31.2
B	2.0 mL A	2.0 mL C ₆ F ₆	9.35	15.6
C	2.0 mL A	4.0 mL C ₆ F ₆	6.23	10.4
D	1.0 mL A	10.0 mL C ₆ F ₆	1.70	2.8

Fractional transmission of the diluted Krytox™ to hexafluorobenzene is shown in Figure 75A and exhibits a broad absorption band from 1050 cm⁻¹ to 1350 cm⁻¹ with a distinct peak at 1250 cm⁻¹. The absorbance of the peak at 1250 cm⁻¹ is shown in Figure 75B. A fit to the line provides linear slope of (1.45±0.02) %/(μg/cm²) with an offset of (0.4±0.3)%. Any deviation of the offset from zero is an indication of systematic effects in the measurement, but the reported value within 1.5 standard deviations is an indication that these effects are small compared the the absorbance of Krytox™.

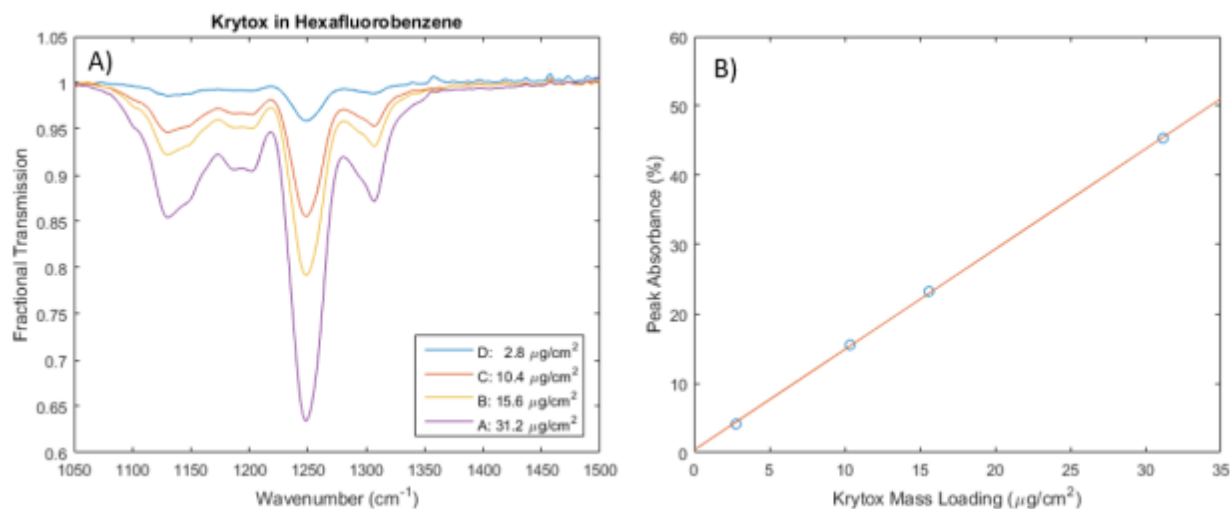


Figure 75. A) Fractional transmission of Krytox™ in hexafluorobenzene at various concentrations. B) Peak absorbance at 1250 cm⁻¹ versus mass loading.

Samples

To simulate a diffusely reflective surface, substrates were prepared using 0.031 inch (= 0.79mm) thick 6061 aluminum sheet stock. The sheet stock was sanded using random orbit sander with #60 (= 250μm) grit sand paper and cut into 20x20mm coupons. Target compound was transferred by pressing a clean lab tissue saturated with a sample of the oil firmly into the center of the coupon to form an approximately 14mm diameter spot of compound on the surface. To make samples with reduced mass loading, these initial samples were wiped using the same technique but with a fresh lab tissue. Since an unknown amount of target is transferred and subsequently partially removed, each sample is independently measured in a FTIR spectrometer configured for reflectance measurements. Figure 76 shows the FTIR signal from a blank sample, an FSO sample (SA11), and no sample. The salient features are dominated by absorption from the room air and by the falling response of the FTIR detector (< 1300 cm⁻¹). However, by normalizing the signal from each sample with the signal from the blank coupon, these effects are removed. Finally, by focusing just on the relevant spectra region (1170 to 1250 cm⁻¹) and removing any linear dependence of the baseline away from FSO spectral features, we can quantitatively determine the absolute reflection, and therefore the absorption, due to just the FSO. Figure 77 shows the results for the FSO samples and Figure 78 shows the results for the Krytox™ samples. The absorption and concluded mass loadings for each sample are summarized in Table 5. Based on the variation of the signal from blank to blank, we estimate that this technique can detect absorption no smaller than ~0.2%, which is equivalent to a mass loading of 0.3 and 0.1 μg/cm² for FSO and Krytox™, respectively.

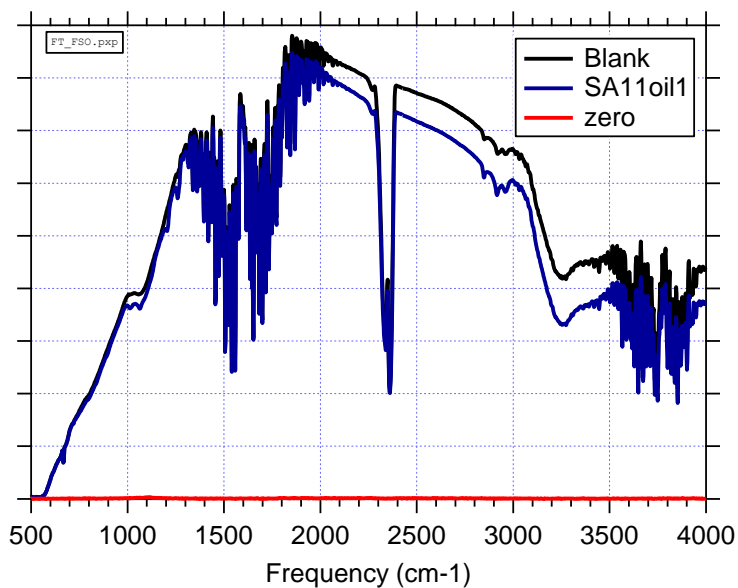


Figure 76. FTIR reflection signal from a Blank sample (black), an FSO sample (blue), and no sample (red).

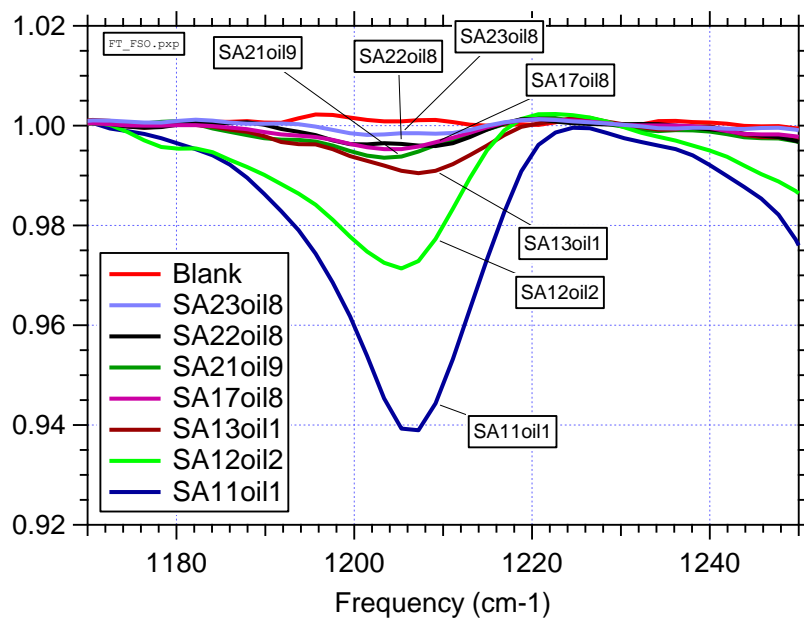


Figure 77. FTIR measured reflectance from all FSO samples and one blank (red).

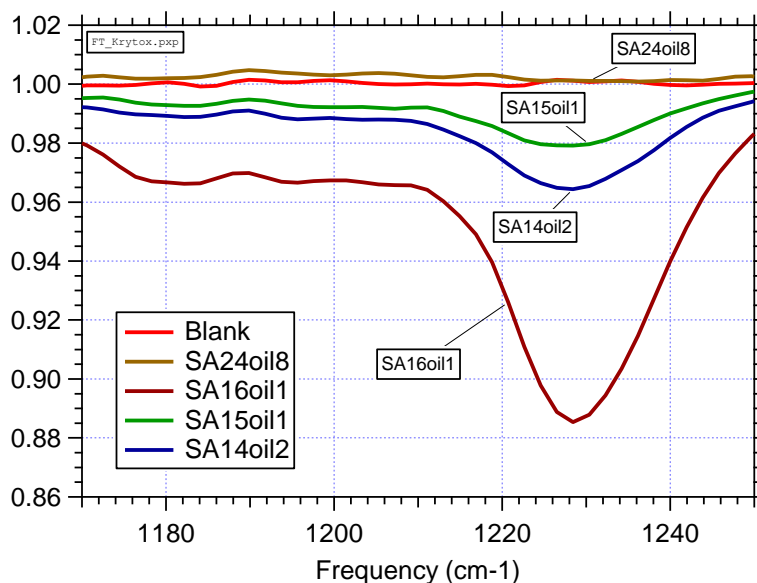


Figure 78. FTIR measured reflectance from all Kryptox™ samples and one blank (red).

Table 5. Summary of Target Coupons and Their Mass Loading

Sample	Target Applied	FTIR Measured Absorption	Concluded Mass Loading ($\mu\text{g}/\text{cm}^2$)
B1	none	<0.2%	0.0
B2	none	<0.2%	0.0
B3	none	<0.2%	0.0
B4	none	<0.2%	0.0
IG	none	<0.2%	0.0
SA11	FSO	6.4%	9.6
SA12	FSO	3.0%	4.5
SA13	FSO	0.89%	1.3
SA17	FSO	0.38%	0.5
SA21	FSO	0.64%	1.0
SA22	FSO	0.40%	0.6
SA23	FSO	0.17%	0.3
SA14	Kryptox™	3.6%	1.2
SA15	Kryptox™	2.1%	0.7
SA16	Kryptox™	11.5%	4.0
SA24	Kryptox™	-0.10%	0.0

QCL comb measurements at 0.3 meter standoff

For this series of measurement (series F and G), the standoff distance to the sample was 0.31m. For this geometry with a 3mm diameter laser spot, we estimate that the geometrical

collection efficiency is $\sim 0.16\%$. However, there is sufficient laser power, that an OD 1.0 attenuator in the signal path is required to set the signal detector to an appropriate level. Figure 79 shows spectral measurements from a series of blanks named B1, B2, B3, B4, and IG. IG is a 1 inch diameter InfraGold surface from LabSphere. The F2B1 measurement is a repeat measurement of the B1 target but with the target removed and re-installed to show the effect of different measurement locations within a single target. The data outside of the ~ 2 to 60 cm^{-1} are not significant because there is negligible comb power in these regions. Note that due to the effect of speckle the baseline level varies from target to target and even from position to position on the same target. Figure 80 shows these same data normalized by the mean of the spectra from the Bx blanks in Figure 79. Note that the 1.973 cm^{-1} oscillations that remain after the bin averaging are completely eliminated, indicating that these oscillations are stable in amplitude and spectral position. However, the absolute reflectance level and low order (up to third order polynomial) shape of the baseline do not repeat. Because of this, in order to make quantitative measurements of target compounds, the third order polynomial dependence of the baseline away from the target spectral features is removed. Figures 81 and 82 show the measurements from the FSO samples before and after normalizing, and Figure 83 shows the measurements with the baseline dependence removed. Because the region in the middle of the spectrum where the comb power is significantly reduced overlaps partially with the FSO feature, this measurement detects FSO down to $\sim 3\mu\text{g}/\text{cm}^2$. Figures 84 and 85 show similar measurements for the KrytoxTM samples before and after normalizing, and Figure 86 shows the KrytoxTM measurements with the baseline dependence removed. Using just the region from 3 to 30 cm^{-1} , these measurements demonstrate FSO detection down to $\sim 1\mu\text{g}/\text{cm}^2$.

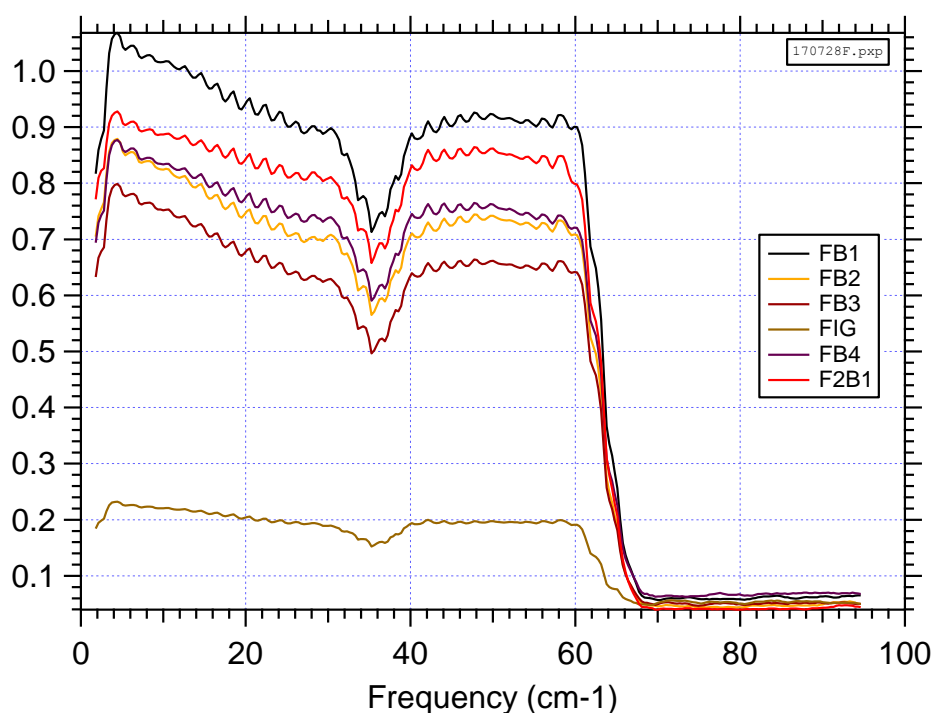


Figure 79. Raw comb envelope from blank samples.

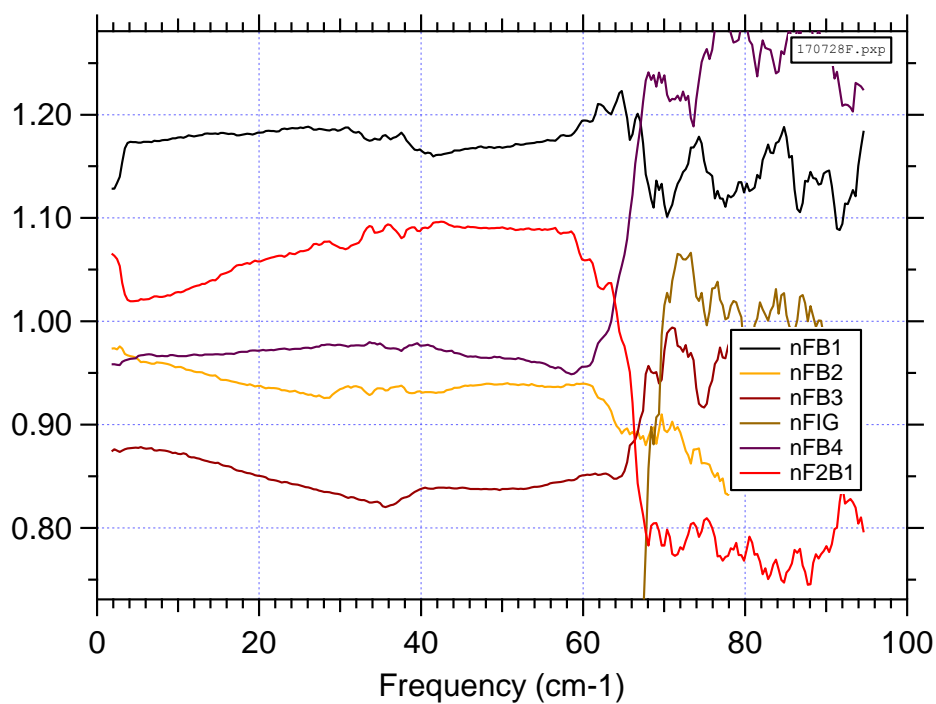


Figure 80. Comb envelope of blank samples normalized by mean of all F series blanks.

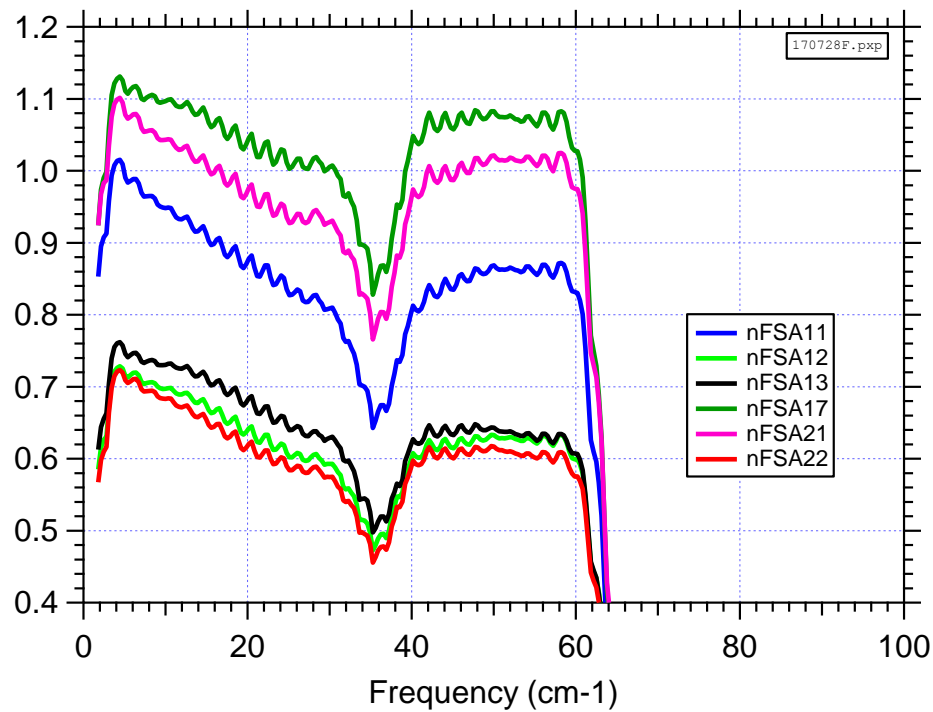


Figure 81. Raw comb envelope of FSO samples.

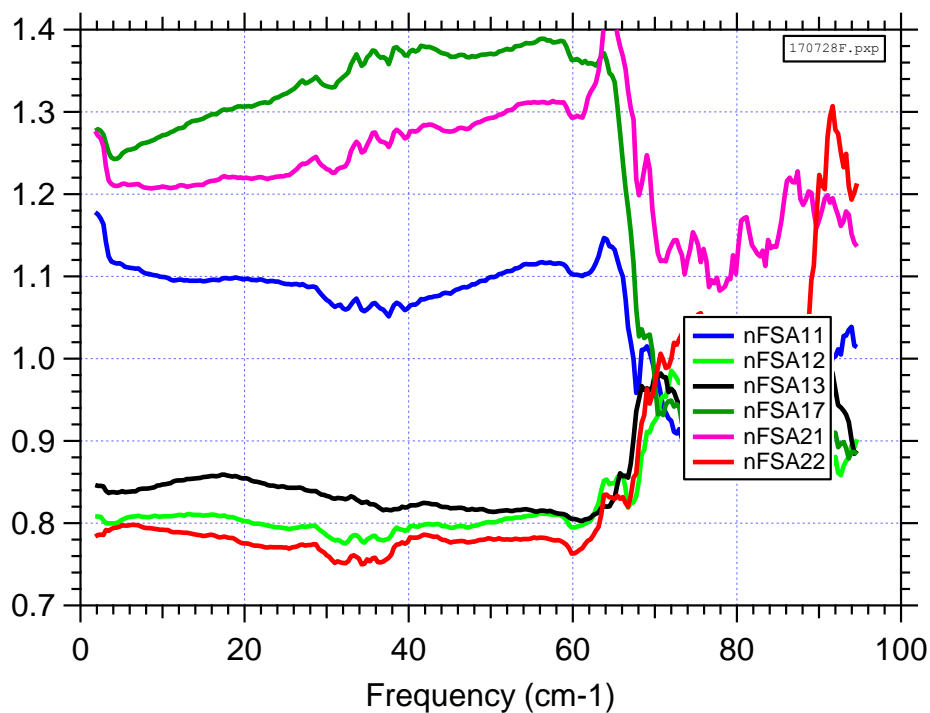


Figure 82. Comb envelope from FSO samples normalized by mean of all F series blanks.

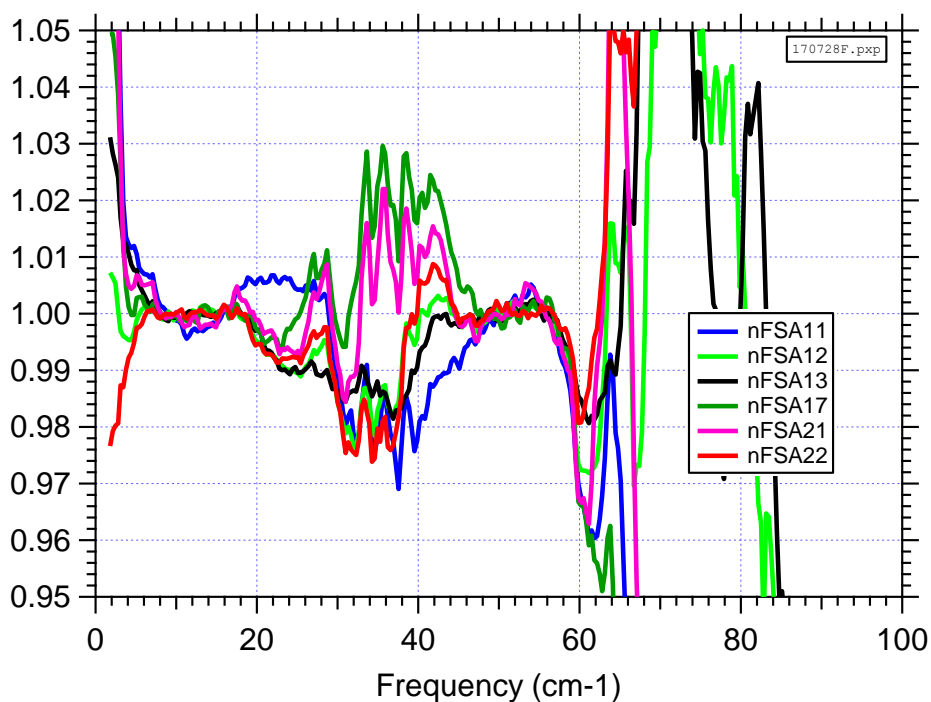


Figure 83. Comb envelope from FSO samples normalized by mean of all F series blanks and 3rd order polynomial baseline removed.

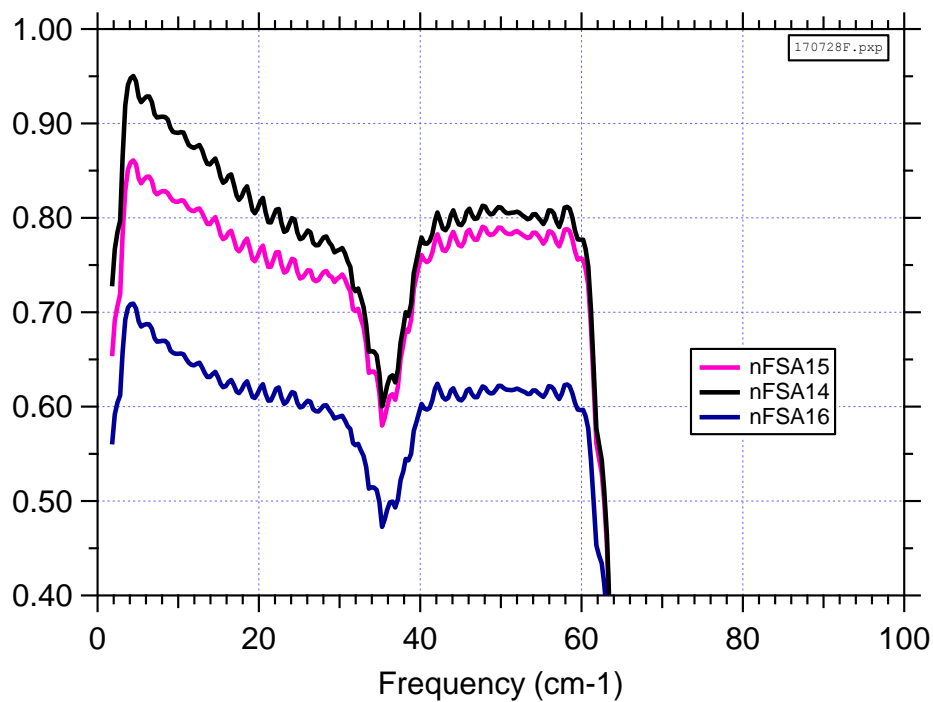


Figure 84. Raw comb envelope of Krytox™ samples.

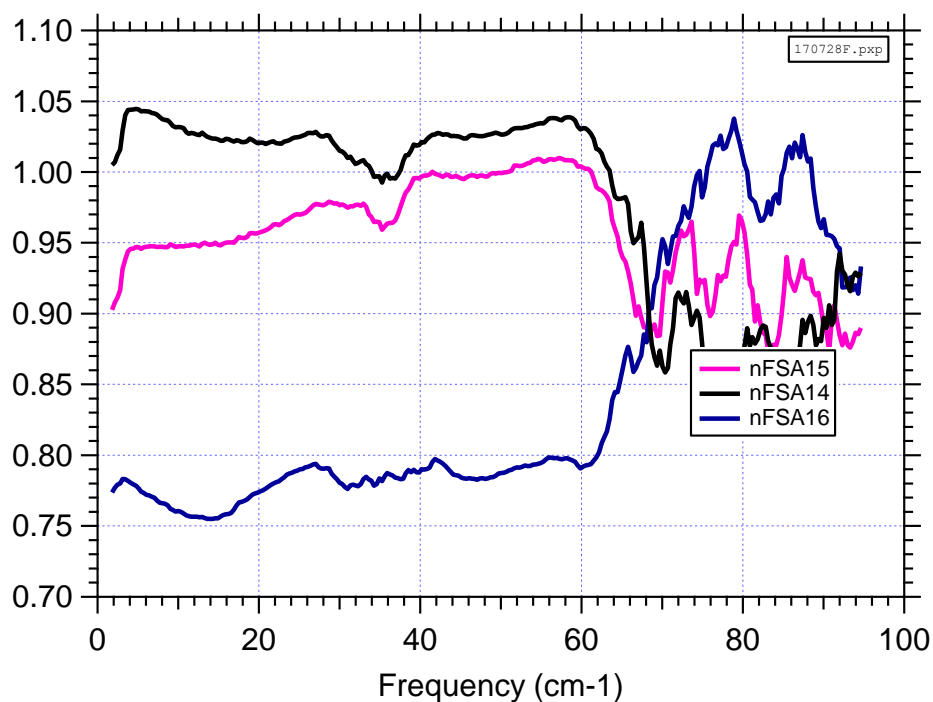


Figure 85. Comb envelope of Krytox™ samples normalized by mean of all F series blanks.

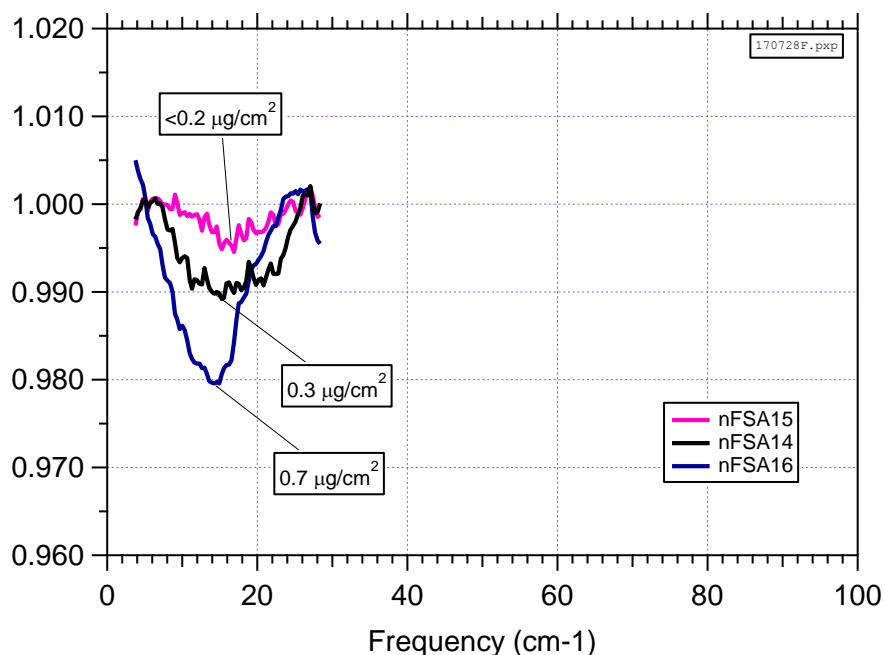


Figure 86. Comb envelope of Krytox™ samples normalized by mean of all F series blanks and 3rd order polynomial baseline removed.

To highlight the issue using an independent sample or sample position to correct for baseline variation, we also took measurements by applying the oil in place without moving the substrate relative to incident laser beam. In this series of experiments a blank sample called “SA23” is mounted to the sample holder and a comb measurement is acquired. FSO is applied in place with a single dab from a saturated lab tissue and another comb measurement called “SA23oil1” is taken. With a fresh tissue, a single swipe removes some amount of FSO from the sample and another comb measurement called “SA23oil2” is taken. This oil removal process is repeated 7 times for measurements “SA23oil3”, “SA23oil4”, ..., “SA23oil8” until the sample is finally removed and characterized in the FTIR (see Figure 77, indicating no measurable FSO remaining). Figure 87 shows the raw measurements. Figure 88 shows the data after normalizing each subsequent measurement with the first measurement “SA23” before oil was applied. Not only is the absolute reflectance level now reasonable but the baseline requires very little flattening. Since the sample cannot be removed during this series of measurements, there are independent FTIR measurements of the sample only at the beginning when it is blank and at the very end. Therefore, for Figure 89 with the baseline corrected data, the labelled mass loading is deduced only from the comb measured absorption level due to the FSO feature. This result reinforces the conclusion that the detection limit is $\sim 1\text{--}3\text{ }\mu\text{g}/\text{cm}^2$.

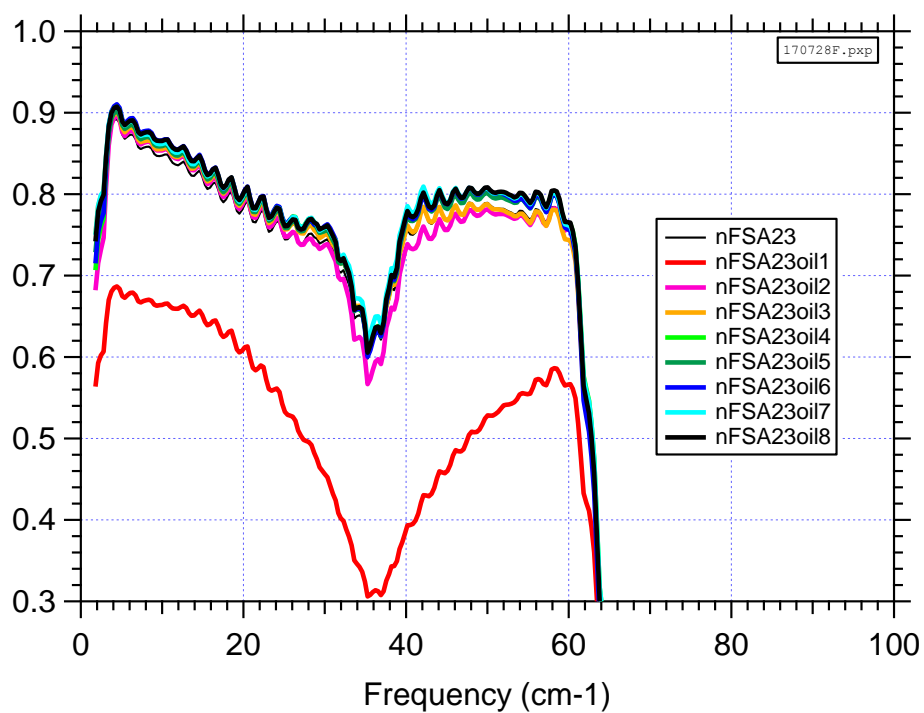


Figure 87. Series of raw comb envelope measurements from FSO applied in place sample.

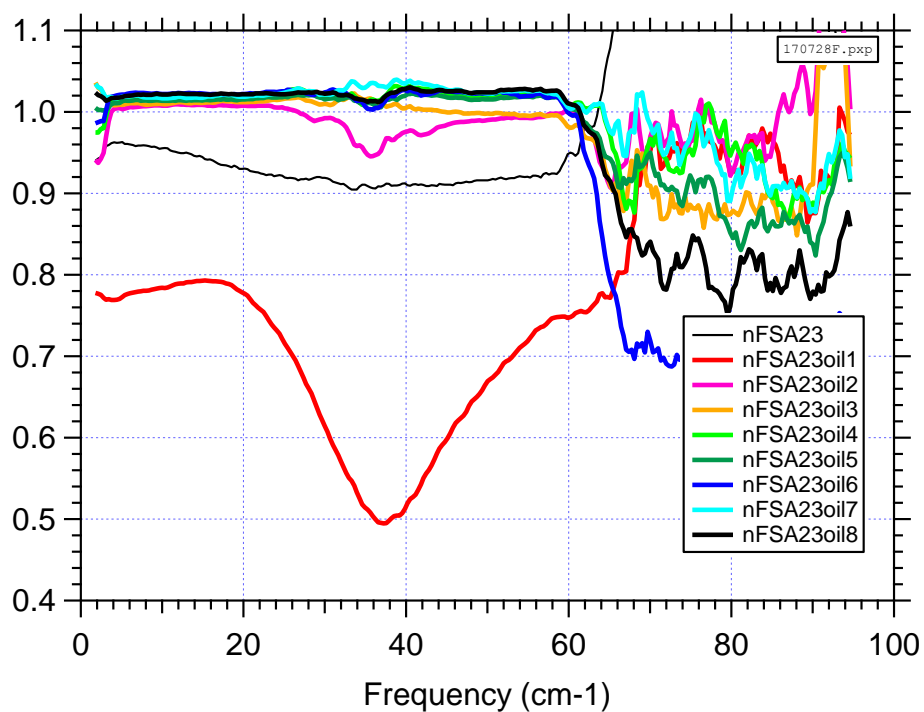


Figure 88. Series of comb envelope measurements from FSO applied in place sample, normalized to first measurement (FSA23).

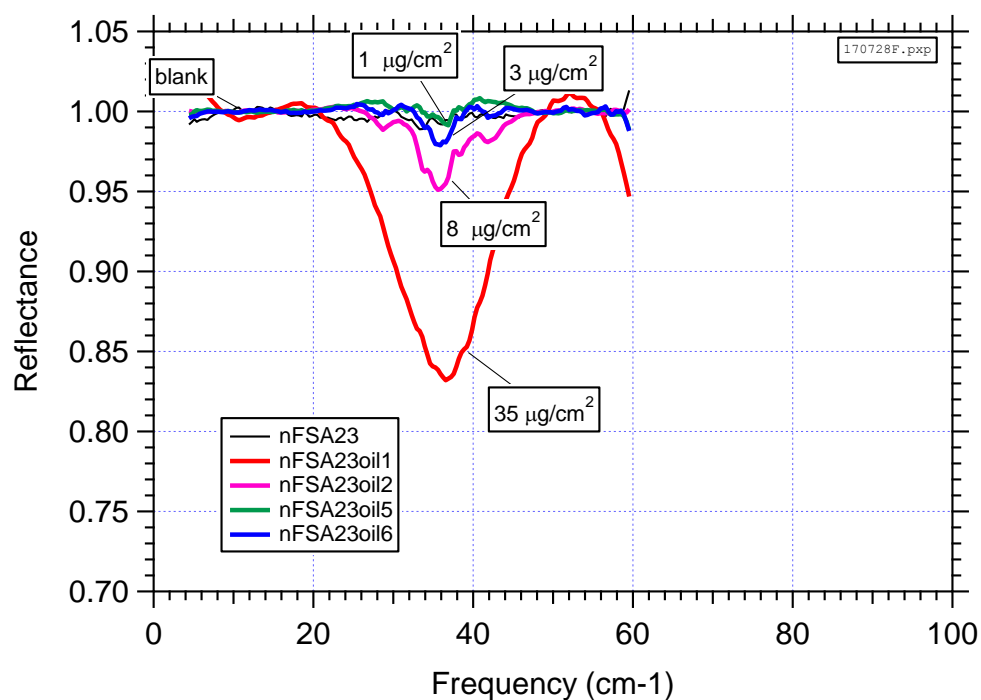


Figure 89. Series of comb envelope measurements from FSO applied in place, normalized to first measurement (FSA23) and 3rd order polynomial baseline removed.

A similar measure series was also taken with Krytox™ applied in place to sample “SA24”. Figure 90 shows the raw measurements. Figure 91 shows the data after normalizing each subsequent measurement with the first measurement “SA24” before Krytox™ was applied. Figure 92 shows these data with just a linear baseline removed, indicating a detection limit $\sim 3\mu\text{g}/\text{cm}^2$.

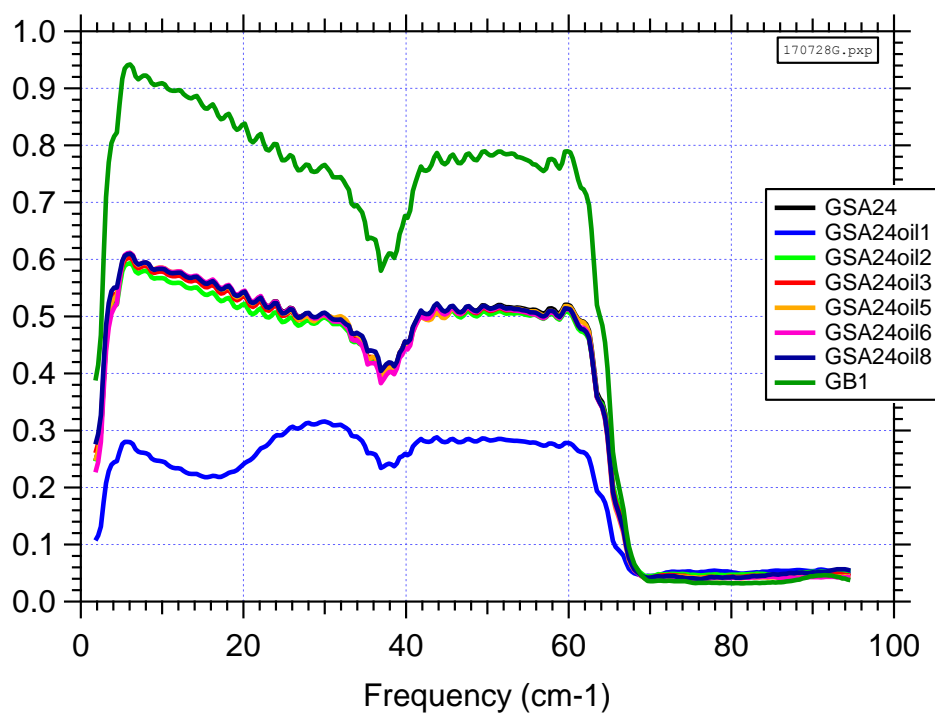


Figure 90. Series of raw comb envelope measurements from Krytox™ applied in place sample.

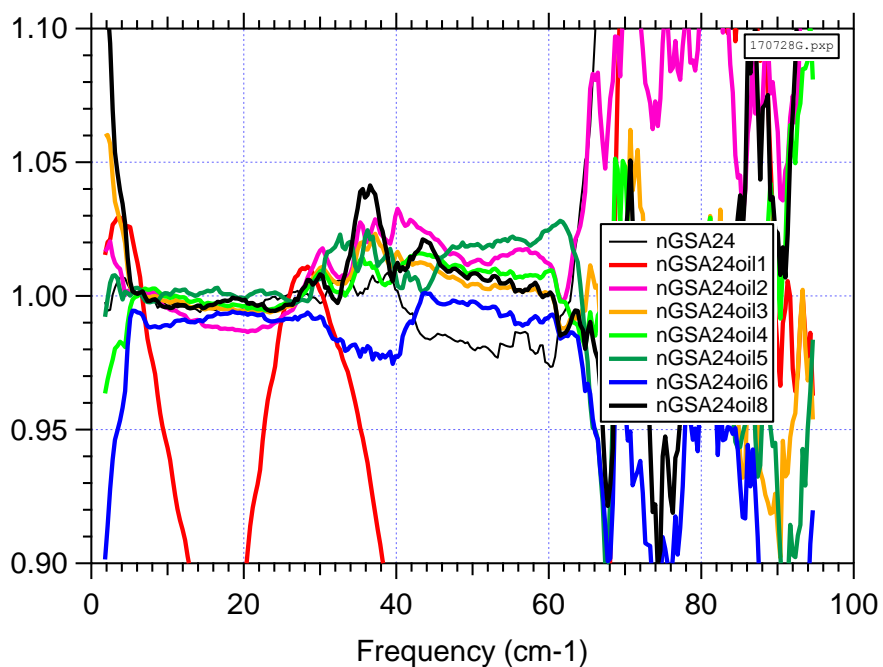


Figure 91. Series of comb envelope measurements from Krytox™ applied in place sample, normalized to first measurement (GSA24).

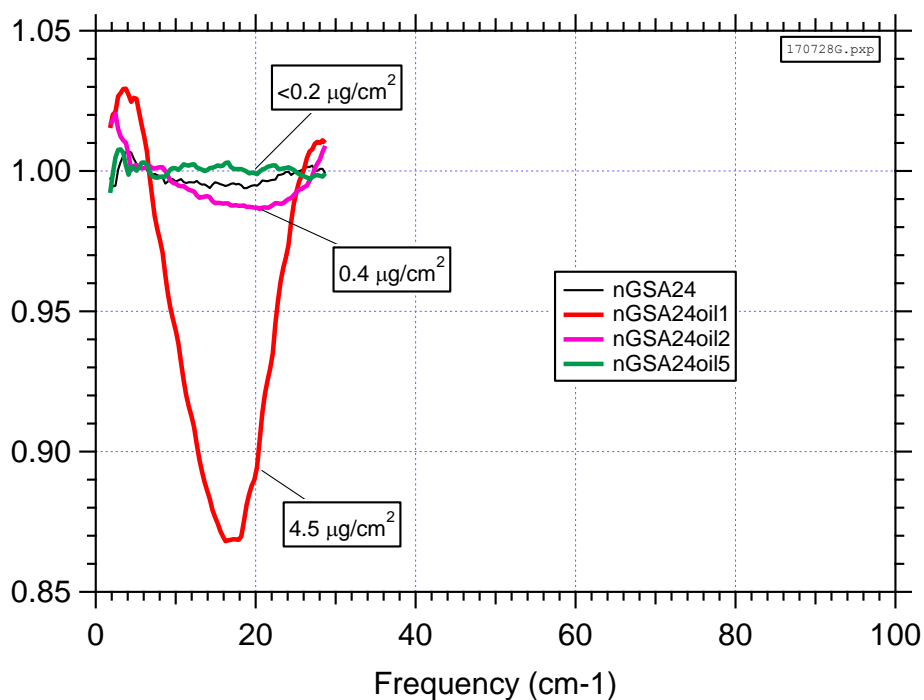


Figure 92. Series of comb envelope measurements from Krytox™ applied in place sample, normalized to first measurement (GSA24) and linear baseline removed.

QCL comb measurements at 1 meter standoff

For this series of measurement (series E), the standoff distance to the sample was 0.87m. For this geometry with a 3mm diameter laser spot, we estimate that the geometrical collection efficiency is $\sim 0.09\%$, dominated by the dropping solid angle fraction that the collection optic subtends. We reduced the OD attenuation in the signal path from 1.0 to 0.3. We also tried removing the attenuation altogether ($OD = 0.0$, series C and D). While this resulted in adequate laser power on the detector, the comb spectra were less stable, so the following results were taken with $OD = 0.3$. Figures 93 and 94 show the FSO samples before and after normalization, respectively, while Figure 95 shows these data with a third order polynomial baseline removed. In Figure 95 the points for which the comb amplitude was too small have also been removed. Even though some of these points lie in the center of the FSO spectral feature, the $\sim 6\%$ absorption signature from SA11, equivalent to $\sim 9\mu\text{g}/\text{cm}^2$ mass loading, is apparent, and lowest detectable mass loading seems to be a few $\mu\text{g}/\text{cm}^2$. Figures 96, 97, and 98 show a similar series for the Krytox™ samples, reinforcing the detection limit of a few $\mu\text{g}/\text{cm}^2$.

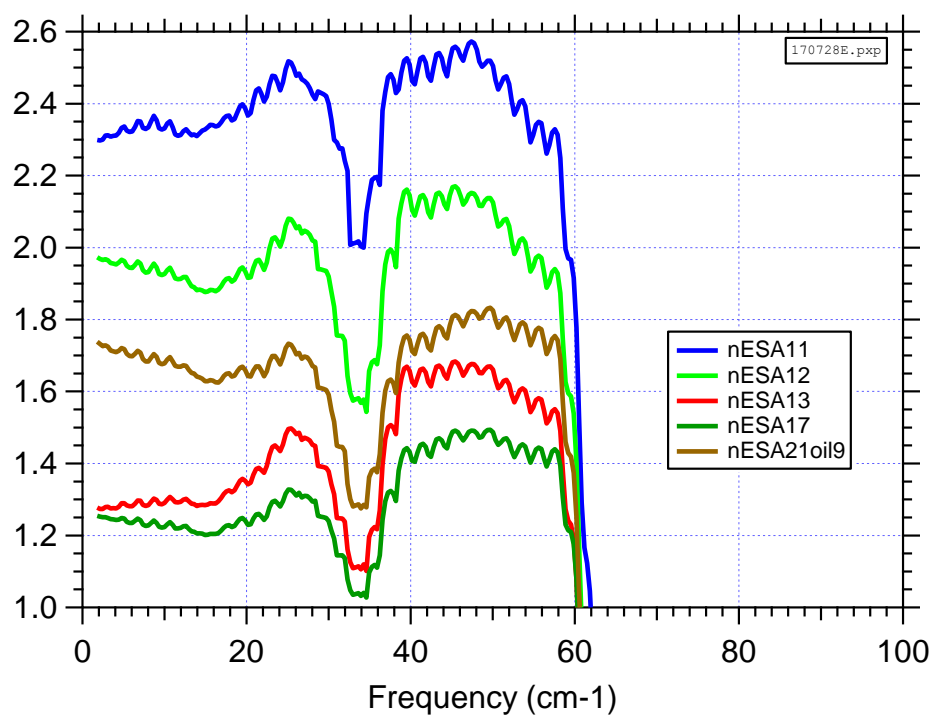


Figure 93. Raw comb envelope of FSO samples at 0.98m standoff.

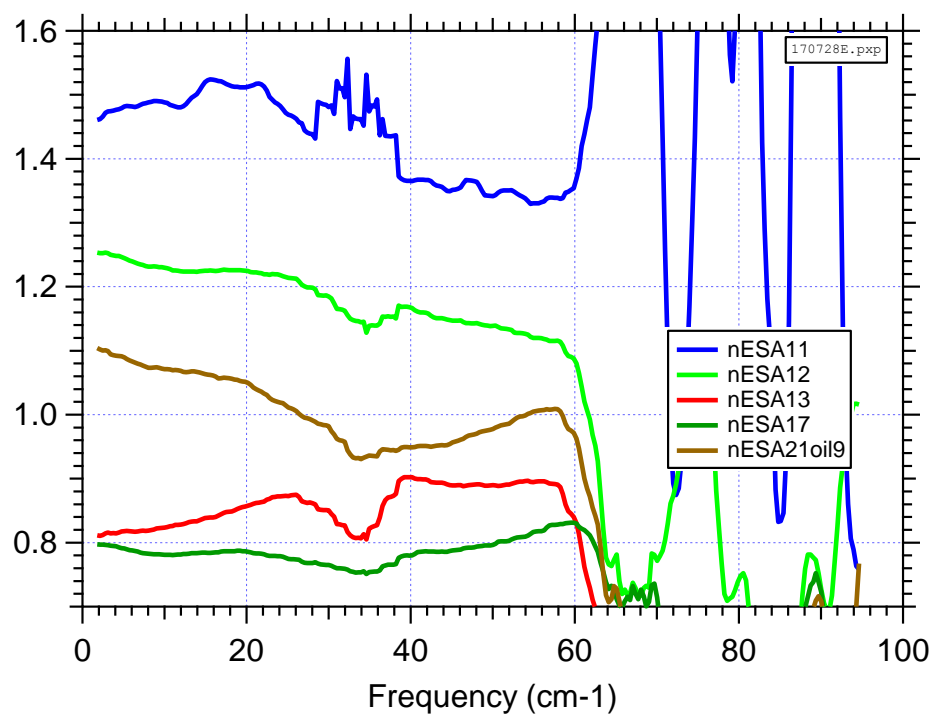


Figure 94. Comb envelope of FSO samples normalized by mean of measurements EB1,EB2,EB3,EB4 at 0.98m standoff.

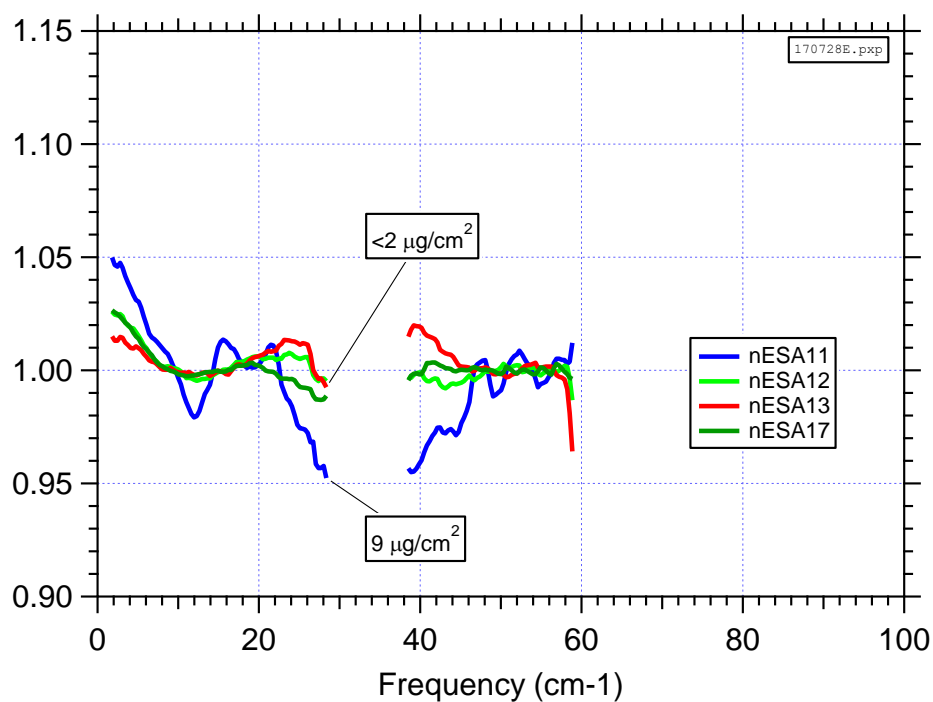


Figure 95. Comb envelope of FSO samples normalized by mean of measurements EB1,EB2,EB3,EB4 and 3rd order polynomial baseline removed at 0.98m standoff.

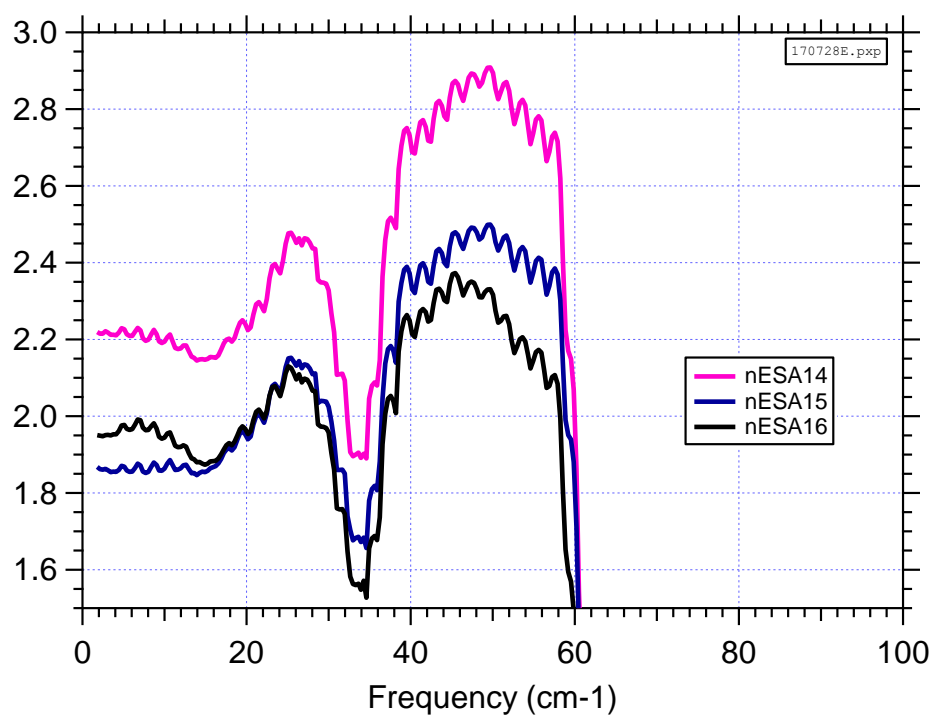


Figure 96. Raw comb envelope of Krytox™ samples at 0.98m standoff.

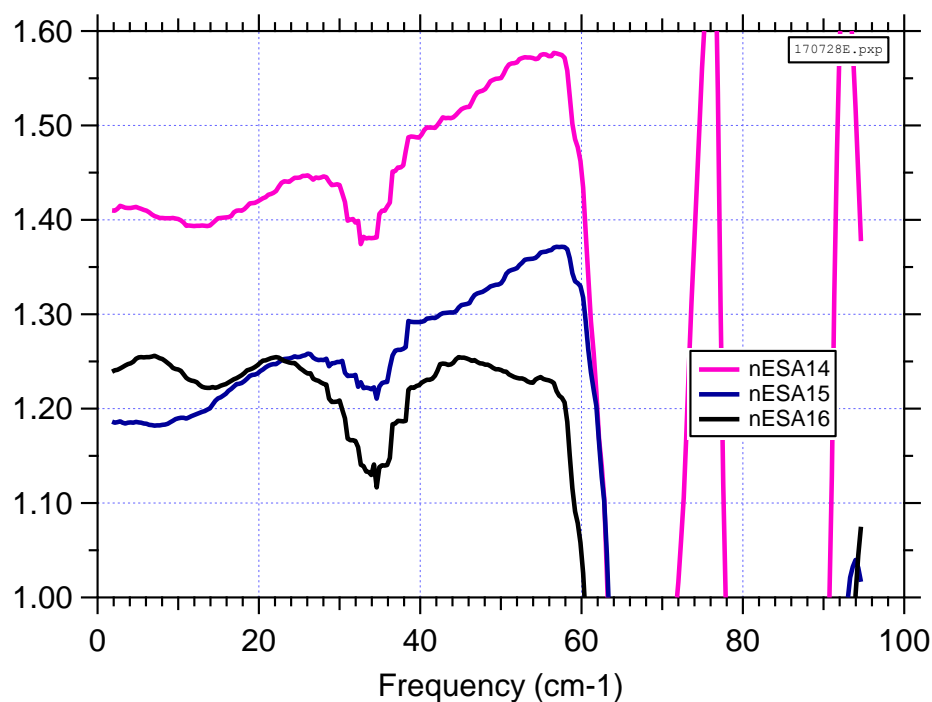


Figure 97. Comb envelope of Krytox™ samples normalized by mean of measurements EB1,EB2,EB3,EB4 at 0.98m standoff.

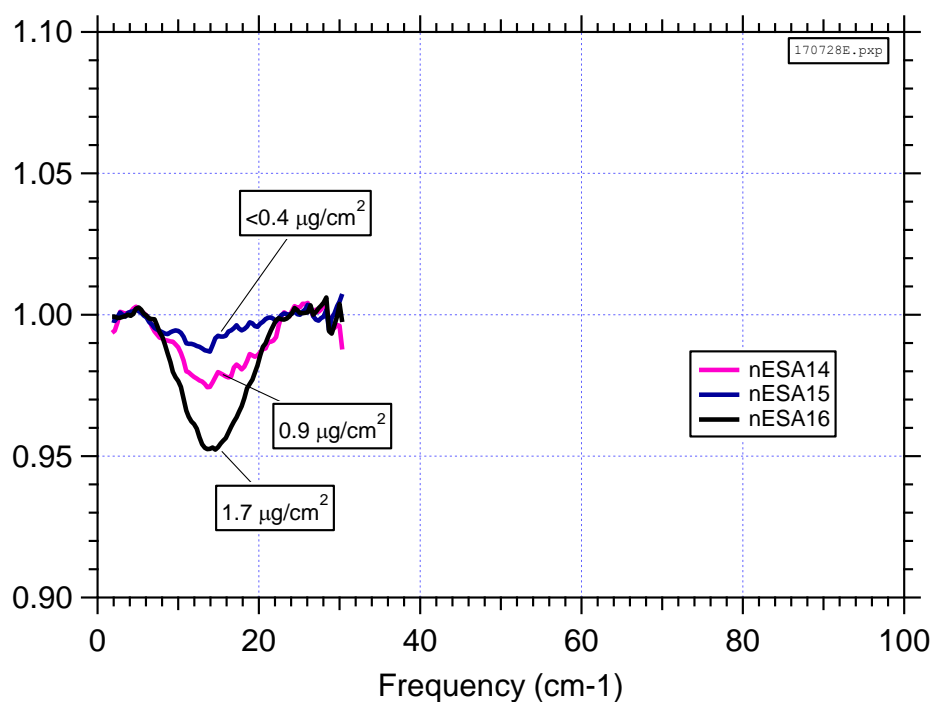


Figure 98. Comb envelope of Krytox™ samples normalized by mean of blank measurements EB1,EB2,EB3,EB4 and 3rd order polynomial baseline removed at 0.98m standoff.

During this measurement series sample SA22 was treated with FSO in place using the procedure described above where target compound is first applied and then partially removed with single wipes, repeating the comb measurement at each point. Figure 99 and 100 show the raw and normalized results, respectively, and Figure 101 shows the result after the baseline is removed. Figure 102 shows a subset with the small amplitude comb points removed and the effective surface mass loading identified.

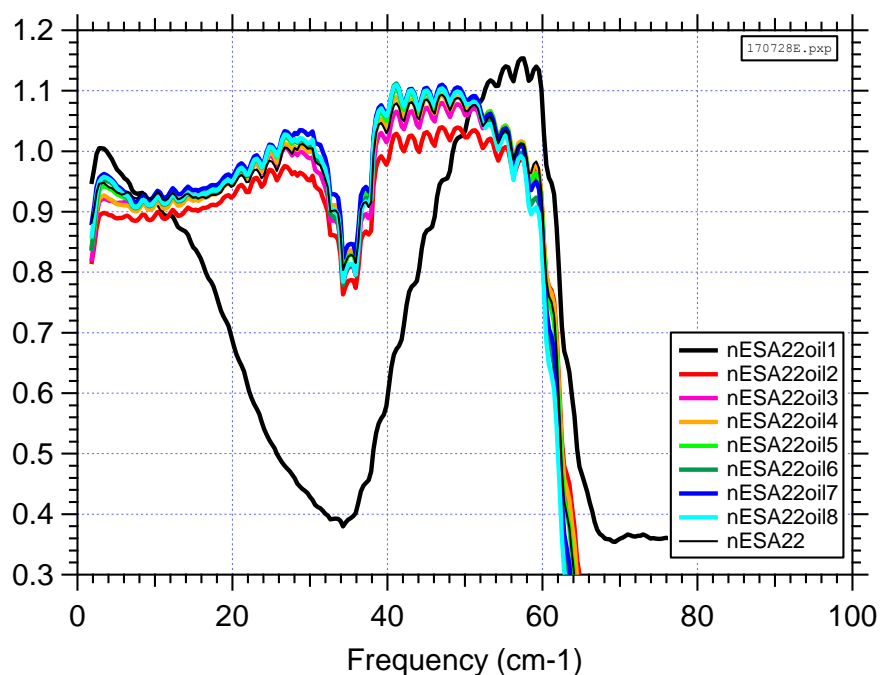


Figure 99. Series of raw comb envelope measurements from FSO applied in place sample at 0.98m standoff.

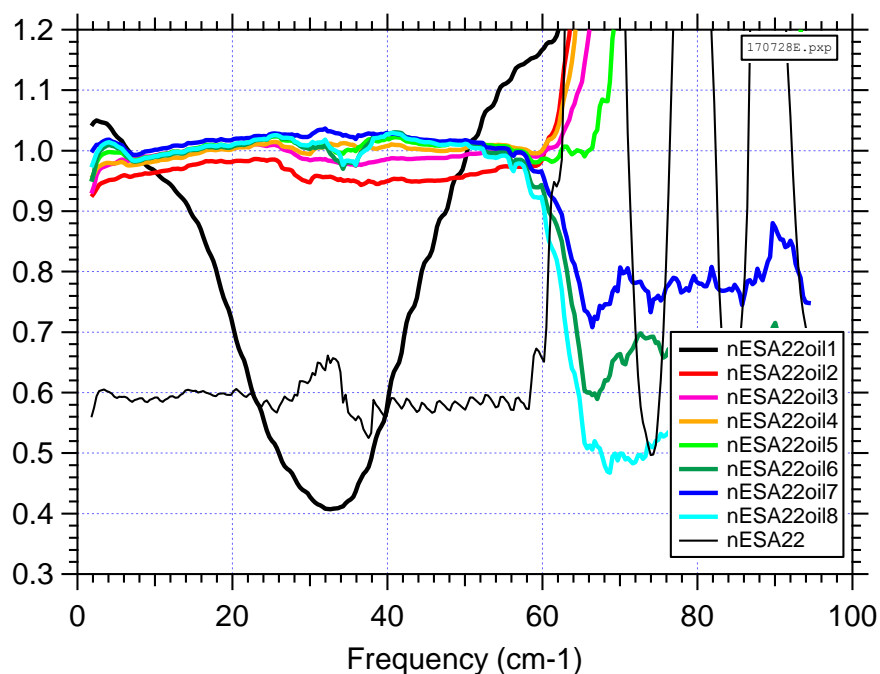


Figure 100. Series of comb envelope measurements from FSO applied in place sample, normalized to first measurement (ESA22) at 0.98m standoff.

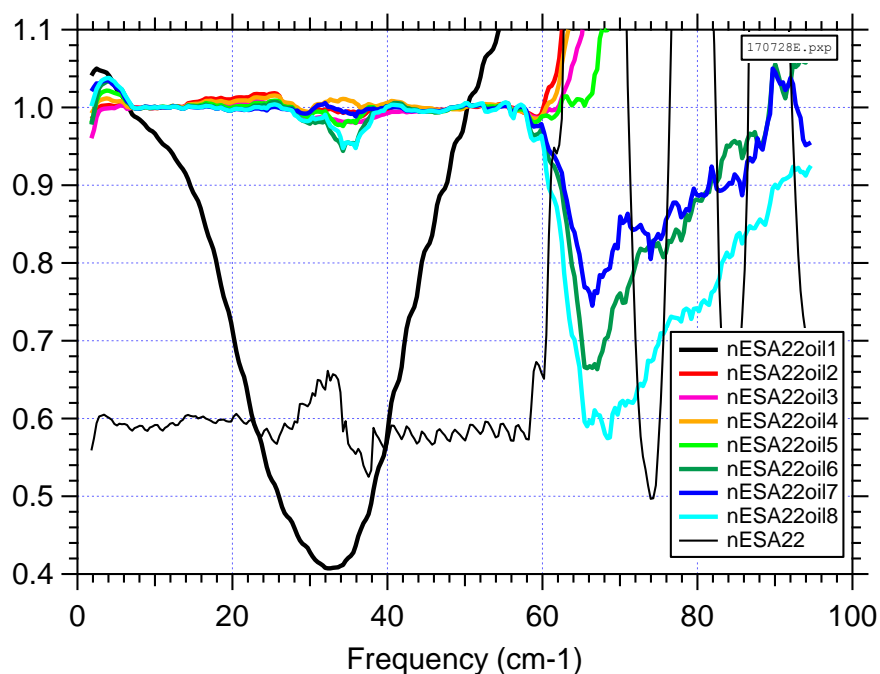


Figure 101. Series of comb envelope measurements from FSO applied in place sample, normalized to first measurement (ESA22) and 3rd order polynomial baseline removed at 0.98m standoff.

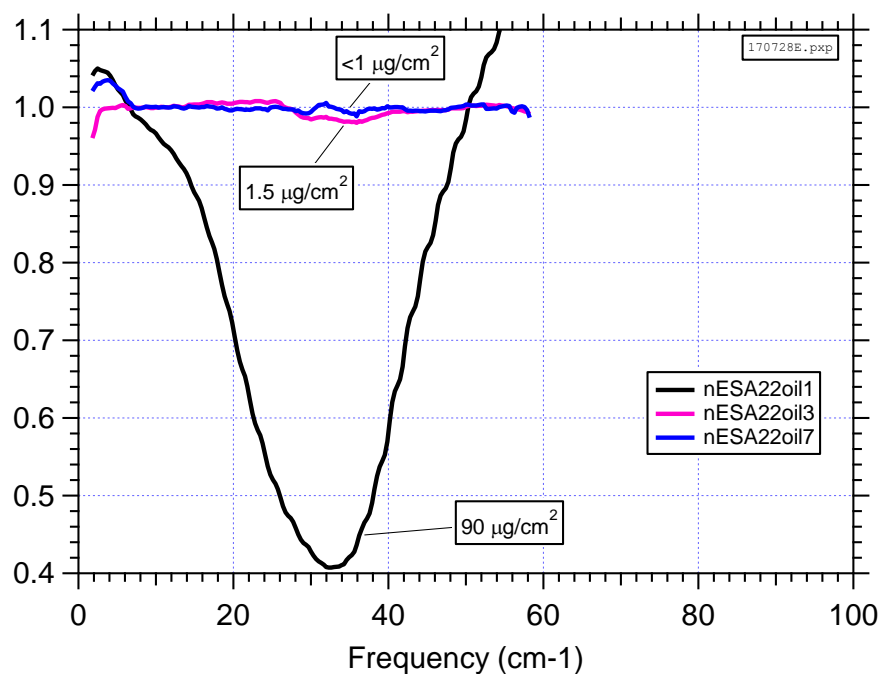


Figure 102. Selected comb envelope measurements from FSO applied in place sample, normalized to first measurement (ESA22) and 3rd order polynomial baseline removed at 0.98m standoff.

5.0 CONCLUSIONS

In this program we demonstrated a compact dual-optical frequency comb (OFC) sensor for standoff detection of national security relevant compounds. These compounds are primarily solids at room temperature and consequently have low vapor pressure. In realistic application scenarios these materials are found on common surfaces that are not necessarily optically flat and highly reflective, so we have emphasized diffusely reflective surfaces that are representative of the real-world surfaces. Because the target materials have their strongest spectral signatures in the LWIR (8 to 12 μm) regime, our OFC sources are based on dispersion compensated QCLs. Targeting two spectrally rich regions of the LWIR, we designed lasers at 8.3 μm (1180 to 1240 cm^{-1}) and 10.0 μm with a novel dispersion compensating approach in the laser processing. The 8 μm lasers emit ~1W optical power under cw operation near room temperature and produce combs with optical bandwidths exceeding 100 cm^{-1} . We developed processing algorithms for reducing the high bandwidth multi-heterodyne data stream into the desired spectral information with up to 0.3 cm^{-1} resolution and optimizing the signal to noise ratio. Finally, we tested a prototype dual-comb system against diffusely scattering surfaces at standoff distances up to 1 meter and demonstrated spectral discrimination at the few $\mu\text{g}/\text{cm}^2$ mass loading level, a relevant level for national security needs.

Based on these results, we conclude that standoff detection from diffusely scattering surfaces using coherent comb sources is possible. However, the scattering surface introduces a random measurement to measurement fluctuation in the amplitude of the overall comb envelope. Since this variation affects only the overall envelope and not the tooth to tooth amplitude, we demonstrated relative measurements of specific spectral features. Scattered light also provides a pathway for optical feedback into the laser, to which QCL combs are particularly sensitive. The measurement SNR is currently limited by these effects and not by the inherent comb amplitude or frequency noise. The amount of feedback falls with increasing standoff distance, so that at meter scale distances with proper optical isolation, the sensitivity limit can be improved to the inherent laser noise level limit.

Due to the spectral complexity of typical targets and cluttered environments, it is critical to increase the comb bandwidth. With improved dispersion control bandwidths exceeding 150 cm^{-1} should be achievable. Increasing this bandwidth by another factor of two will require not only wider QCL gain bandwidth but also either faster detectors or better matching between the spacings of the individual combs (ΔF_{rep}).

6.0 RECOMMENDATIONS

Based on the successful Phase 1 development, we recommend the following next steps:

- Integrate the 10 μ m band into the sensor
- Embedded the signal processing algorithms in the system hardware to allow real-time processing
- Demonstrate the sensor performance against other surfaces and increasingly spectrally cluttered environments
- Address size, weight, and power constraints in a second generation prototype.

7.0 REFERENCES

Bidaux, Y., I. Sergachev, W. Wuester, R. Maulini, T. Gresch, A. Bismuto, S. Blaser, A. Muller, and J. Faist, *Opt. Lett.* **42** (8), 1604 (2017)

Coddington, I., W. Swann, and N. Newbury, "Coherent dual-comb spectroscopy at high signal-to-noise ratio," *Phys. Rev. A* **82**, 043817 (2010)

Faist, J., F. Capasso, D. L. Sivco, C. Sirtori, A.L. Hutchinson, A. Y. Cho, *Science* **264**, 553 (1994)

Hofstetter, D. and J. Faist, *IEEE Photonic Tech L* **11**, 1372 (1999)

Hugi, Andreas, Villares Gustavo Filipe Ferreira, and Jérôme Faist. Method for Optical and Electrical Signal Processing of a Multi-Heterodyne Signal Generated by a Multi-Mode Semi-Conductor Laser and Detection Device Utilizing that Method. US2017201328 (A1), issued July 13, 2017.

https://worldwide.espacenet.com/publicationDetails/biblio?FT=D&date=20170713&DB=EPODOC&locale=en_EP&CC=US&NR=2017201328A1&KC=A1&ND=4

Ideguchi, Takuro, Antonin Poisson, Guy Guelachvili, Nathalie Picqué, and Theodor W. Hänsch. "Adaptive Real-Time Dual-Comb Spectroscopy." *Nature Communications* **5** (February 27, 2014): 3375. doi:10.1038/ncomms4375

Jouy, P., J. M. Wolf, Y. Bidaux, P. Allmendinger, M. Mangold, M. Beck and J. Faist, "Dual comb operation of $\lambda \sim 8.2 \mu\text{m}$ Quantum Cascade Laser frequency comb with 1 W optical power", *Appl. Phys. Lett.* **111**, 141102 (2017).

Keilmann, F., et al. Time-domain mid-infrared frequency-comb spectrometer. *Opt. Lett.* **29**, 1542–1544 (2004)

Schiller, S., "Spectrometry with frequency combs," *Opt Lett*, vol. 27, no. 9, pp. 766–768, 2002.

Villares, G. et al, *Appl. Phys. Lett.* **107**, 251104 (2015)

Villares, G., A. Hugi, S. Blaser, and J. Faist, *Nature Communications* **5**, 5192 (2014)

Villares, G., S. Riedi, J. Wolf, D. Kazakov, M. J Süess, P. Jouy, M. Beck, and J. Faist, *Optica* **3** (3), 252 (2016)

Yang, Y., D. Burghoff, J. Reno, and Q. Hu. "Computationally-Assisted THz Dual-Comb Spectroscopy Using Quantum Cascade Laser Frequency Combs." In *2016 Conference on Lasers and Electro-Optics (CLEO)*, 1–2, 2016

LIST(S) OF SYMBOLS, ABBREVIATIONS, AND ACRONYMS

BIG	Bismuth Iron Garnet
ETH	Swiss Federal Institute of Technology
FSO	Fluorinated Silicone Oil
FTIR	Fourier Transform InfraRed
FWM	Four Wave Mixing
GDD	Group Delay Dispersion
GTI	Gires-Tournois
HR	High Reflectivity
JPEO-CBD	Joint Program Executive Office for Chemical and Biological Defense
LIV	Optical power – Current – Voltage
LWIR	Longwave Infrared
MCT	Mercury Cadmium Telluride
NDF	Neutral Density Filter
NEP	Noise Equivalent Power
NGCD	Next Generation Chemical Detector
OFC	Optical Frequency Comb
PSI	Physical Sciences Inc.
QCLs	Quantum Cascade Lasers
RF	Radiofrequency
SNR	Signal to Noise Ratio
TGG	Terbium Gallium Garnet
YIG	Yttrium Iron Garnet